Synthesis of Iron Doped Titania and its Application in Degradation of Organic Pollution in Water

by

Vahid Moradi

B.Sc., Razi University, 2008

M.Sc., Buali Sina University, 2010

A Dissertation Submitted in Partial Fulfillment of the Requirements for the Degree of

DOCTOR OF PHILOSOPHY

in the Department of Mechanical Engineering

University of Victoria

Supervisory Committee

Synthesis of Iron Doped Titania and its Application in Degradation of Organic Pollution in Water

by

Vahid Moradi

B.Sc., Razi University, 2008

M.Sc., Buali Sina University, 2010

Supervisory Committee

Dr. Rodney Herring, Co-Supervisor

(Department of Mechanical Engineering)

Dr. Martin B.G. Jun, Co-Supervisor

(Department of Mechanical Engineering, Purdue University)

Dr. R.B. Bhiladvala, Departmental Member

(Department of Mechanical Engineering)

Dr. Harry H. L. Kwok, Outside Member

(Department of Electrical and Computer Engineering)

Abstract

Supervisory Committee

Dr. Rodney Herring, Co-Supervisor
(Department of Mechanical Engineering)

Dr. Martin B.G. Jun, Co-Supervisor
(Department of Mechanical Engineering)

Dr. R.B. Bhiladvala, Departmental Member
(Department of Mechanical Engineering)

Dr. Harry H. L. Kwok, Outside Member
(Department of Electrical and Computer Engineering)

Anatase TiO_2 has attracted a lot of attention due to its applications as a photocatalyst in water and air treatment technologies. However, its large band gap energy (~3.2 eV) limits its application only to UV light. Also, anatase TiO_2 suffers from high electron/hole recombination, which diminishes its photocatalytic activity. Therefore, different methods have been employed to decrease its band gap energy and reduce the recombination of the charge carriers. One of the methods is to incorporate impurities as dopants in its crystal lattice. Different metal and non-metal dopants have been studied for this aim. Among the different choices, Fe^{3+} has showed a great potential to improve the photocatalytic activity of TiO_2 under visible light irradiation. Firstly, the d orbitals of Fe^{3+} interact with the 3d orbitals of Ti^{4+} generating intermediate band gap energy levels to facilitate excitation of electrons under visible light by a red shift in the absorption of light. Secondly, Fe^{3+} can interact with both electrons and holes to produce Fe^{2+} and Fe^{4+} trapping the charge carriers and reducing their recombination rate. Fe^{2+} and Fe^{4+} can release the electron and hole and revert back to the Fe^{3+}. The released charge carriers migrate to the surface of the nanoparticles to initiate the photocatalytic reactions. However, it was found that the photocatalytic activity of Fe-TiO_2 is not as high as expected. Therefore, in this research study I investigated the cause for its low photocatalytic activity and found methods to improve it. The Fe-TiO_2 was synthesized using a facile sol-gel method and its structure and properties were characterized by different instrumental techniques. Using TEM and HRTEM an amorphous layer was seen on the surface of the nanoparticles. This layer characterized using XPS and EDX was composed of iron oxide layers. This layer was contaminating the surface of the nanoparticles where the photocatalytic reactions take place. Moreover, the contamination layer was acting as a recombination center for the electrons and holes. To the best of our knowledge, no previous study was conducted to investigate the effect of an iron oxide contamination layer on the photocatalytic activity of Fe-TiO_2 nanoparticles. This layer was removed using a concentrated HCl solution confirmed using HRTEM and XPS. Also, using DRS it was shown that its removal does not effect the optical properties of the Fe-TiO_2 confirming that the acid treatment process did not influence the doped Fe^{3+} in the TiO_2 crystal lattice. The degradation of methelyne orange (MO), a representative pollutant, was increased from 25% to 98% under visible light irradiation. Also, in order to achieve the highest performance of the photocatalyst, it was necessary to study the parameters of the photocatalytic activity and the degradation efficiency. Therefore, experiments using a phenol solution, another representative pollutant, were conducted to investigate and optimize the effects of the catalyst load, reaction time, initial concentrating of the pollutant and pH. The degradation efficiency of the phenol solution was found to increase from 31% to 57% by the removal of the contamination layer and by controlling the pH of the solution.

Table of Contents

List of Figures

List of Tables

Glossary

AOP	Advanced Oxidation Process
CB	Conduction band
DE	Degradation Efficiency
DRS	Diffuse Reflectance Spectroscopy
EDX	Electron Dispersive X-ray
HRTEM	High Resolution Transmission Electron Microscopy
MO	Methyl Orange
PZC	Point of Zero Charge
SAED	Selected Area Electron Diffraction
TEM	Transmission Electron Microscopy
UV	Ultraviolet
VB	Valence band
XPS	X-ray Photoelectron Spectroscopy
XRD	X-ray Diffraction

Acknowledgments

I would like to express my deepest appreciations to my supervisors Dr. Rodney Herring and Dr. Martin Jun for their help, support and insightful comments throughout my PhD. I also wish to extend my thanks to the members of my supervisory committee Dr. Rustom Bhiladvala, Dr. Harry Kwok and Dr. Troy Vassos. I would also thank Dr. Elaine Humphery for her helpful guidance on the SEM and Dr. Arthur Blackburn for his support and advice on the TEM. I am also very thankful to Dr. Alexander Brolo for letting me use some space in his laboratory and Dr. Milton Wang for his help and support.

I would also like to thank my dear friends and colleagues Shannon Johnson, Ahmad Esmailirad, Mohammad Pelaschi, Vahid Ahsani, Mana Norouzpour, Farzam Allafchi and many others. Their company, advice and friendship helped me to confront the challenges and difficulties faced during my PhD.

I want to especially express my deepest sense of gratitude to my mother for her lifetime support, encouragement and love, to my father who was always there for me and inspired me with his strength and energy and to my brother Navid for all the great moments we have had through these times. Words cannot express how much I love them and how grateful I am for their support.

Chapter 1 Introduction

1.1 Research Motivation

Limited access to fresh water is a challenge for many people around the world due to the rapid growth in the population. Also, pollution from sewage, agricultural activities and industrial waste have increased the need for seeking effective methods to treat their wastewater. Numerous technologies including physical, biological and chemical methods have been employed to remove contamination from wastewater. Physical methods such as sedimentation, filtration and adsorption employ physical methods to remove the pollution from the waste water [1-3]. Chemical treatments such as the chlorination, coagulation and ion exchange methods accomplish pollution removal using a chemical process [4-6]. The biochemical methods use microorganisms to decompose organic materials into more stable end products [7, 8]. Biological methods require large operational area. The chemical methods introduce toxic chemicals into the water. None of these methods of cleaning wastewater are able to remove the contamination completely [9]. Hence, the conventional methods are usually a combination of the biological and chemical cleaning methods [10]. On the other hand, Advanced Oxidation Processes (AOPs) have proven their potential to completely degrade chemically stable pollutant compounds [11]. There are several AOP methods such as the fenton reactions [12, 13], ozonation [14], plasma oxidation [15, 16], UV/H_2O_2 [17, 18] and photocatalytic reactions [19-21]. These methods rely on the generation of hydroxyl radicals (•OH) that are strong oxidizing agents having a redox potential of 2.8 V [22], the strongest of the oxidizing radicals, having the potential to completely degrade the organic matter in the wastewater to produce water and carbon dioxide (CO_2) as the end products [23].

Among different AOP methods, photocatalytic reactions have been studied vastly since they have shown a very good capability to degrade organic pollution. The photocatalytic reactions utilize the metal oxide semiconductors such as ZnO [24], CdS [25], WO_3 [26] and TiO_2 [27]. TiO_2 has been studied widely owing to its high photocatalytic activity, chemical inertness, non-toxicity and low cost. The crystal form of anatase TiO_2 possesses a large band gap of 3.2 eV, which provides sufficient energy for generating electron/hole pairs that participate in redox reactions by producing hydroxyl radicals [28]. Irradiation by a photon of higher energy than the band gap can excite the electrons from the valence band to the conduction band to generate conduction band electrons and valence band holes [29]. The problem with titania's large band gap is that the electron excitation from the valence band to conduction band can occur only under UV irradiation, which has a higher energy than the 3.2 eV band gap. This limits the application of TiO_2 to the UV light region. Since only 4-5% of the sunlight reaching the earth contains UV light, it is inefficient in utilizing TiO_2 under sunlight irradiation [23]. Another challenge in using TiO_2 as a photocatalyst is the high number of electron/hole recombination, which has an adverse effect on its photocatalytic activity [30]. These problems can be solved by adding transition metal impurities as dopants into the crystal structure of TiO_2 [21] to introduce intermediate energy levels to the band gap of TiO_2 causing a red shift in the light absorption towards longer wavelengths [31, 32]. In addition, the metal dopants can trap electrons and/or holes increasing the life time of the charge carriers that decreases their recombination. Among the different metal dopant options Fe^{3+} is an excellent choice because the interaction of the d orbitals of Fe^{3+} with the d orbitals of Ti^{4+} causes the intermediate energy levels to decrease the band gap. Fe^{3+} also reacts with both the electrons and holes forming Fe^{2+} and

Fe^{4+} ionic states trapping the charge carriers, which leads to an increase in their life time. Hence, doping Fe^{3+} into the crystal lattice of TiO_2 makes it possible to activate the catalyst under visible light irradiation and also increases the photocatalytic activity by charge carrier trapping. The photocatalytic activity of Fe doped TiO_2 (Fe-TiO_2) can be measured by its degradation of a representative pollutant in the water. However, Fe-TiO_2 has not shown the expected efficiency even though it was considered to be one of the most suitable dopants according to the literature review. Previous works showed that its degradation efficiency (DE) was not as high as expected.

In this research thesis study, the optimum synthesis conditions of the Fe-TiO_2 nanoparticles including the amount of the dopant content and the pH of the solution were investigated. Different instrumental analysis methods were employed to characterize the catalyst nanoparticles. Also, the low photocatalytic activity of the catalyst was investigated in order to increase its photocatalytic activity. Moreover, the photocatalytic activity was measured using two different pollutants, methyl orange (MO) and phenol. The degradation efficiency (DE) of the catalyst particles was measured and different influential parameters on their efficiency were studied to find the optimum operational conditions.

1.2 Dissertation outline

The first chapter of the dissertation describes the motivation of the research as a very brief introduction providing the background of the research.

The second chapter is a brief introduction and reviews the TiO_2 crystal structures, properties and synthesis, electron/hole generation and the challenges in using TiO_2, transition metals as dopants. Finally, the photocatalytic activity and kinetics studies of the pollutant degradation is presented.

Chapter 3 is a peer-reviewed published journal paper [33], which introduces a sol-gel method to synthesize the Fe-TiO_2 photocatalyst for wastewater treatment under visible light irradiation, its characterization using different instrumental techniques and the challenges and problems influencing its photocatalytic activity. Then, an acid treatment method is introduced to enhance the photocatalytic activity of the synthesized photocatalysts under visible light and its DE was measured using MO as the pollutant.

Chapter 4 is a submitted journal manuscript for peer review that presents the practical uses of the synthesized photocatalysts. It investigates the influential parameters that affect the photocatalytic activity in detail. Also, using the kinetics of the reaction, the optimum conditions for degradation of phenol as the pollutant are introduced.

Chapter 5 summarizes the main results and contributions and suggests the possible future work.

1.3 Research Contributions

The main objectives of this research work were first to produce and develop an efficient, low cost, affordable photocatalyst using iron doped titania, and to improve and increase its photocatalytic activity under visible light irradiation and second to find the optimum reaction conditions for its practical applications. The main contributions of the current dissertation are summarized as follows:

1. Producing iron doped TiO_2 photocatalyst using a very facile and simple sol-gel method. Sol-gel is one of the most inexpensive and easiest to scale up processes to synthesize nano TiO_2 crystals. The nanoparticles were prepared using this method without adding any surfactants.

2. Investigate the reason behind the low photocatalytic activity of iron doped TiO_2 naoparticles under visible light irradiation using different characterization techniques such as HRTEM and XPS. It was found that an iron oxide layer was contaminating the surface of the nanoparticles reducing their photocatalytic activity.
3. Adding an acid treatment step to the conventional synthesis process of the iron doped TiO_2 nanoparticles to remove the contamination layer from the surface of the nanoparticles using a concentrated HCl solution. The removal was confirmed using HRTEM and XPS.
4. Conducting photocatalytic experiments and kinetic study to obtain the optimum reaction condition for the practical use of the prepared photocatalyst. Different experiments were conducted to obtain the influence of different parameters such as catalyst load, reaction time, initial concentration of pollutant and pH.

Chapter 2 Literature review

This chapter introduces and explains TiO_2, its photocatalytic reactions and their mechanisms and the Fe doping concept of TiO_2.

2.1 Titanium Dioxide (TiO_2): Structures and properties

TiO_2 is a semiconductor, which is used by industry as a paint additive, pigment and cosmetic products such as sunscreens. TiO_2 is inexpensive, chemically stable and environmental friendly. Moreover, it has an excellent charge transport ability making it a very good candidate as a photocatalyst [34, 35]. TiO_2 has three distinct crystal polymorphs of anatase, rutile and brookite; Table 2.1 summarizes the characteristics of these three phases. The crystal structure of both anatase and rutile is tetragonal where each Ti atom is coordinated with six O atoms and each O atom is coordinated with three Ti atoms. Four of the Ti–O bonds have the same length and the two other bonds are greater than the other four. Brookite has an orthorhombic structure where there are six different Ti–O bonds of different lengths [36].

Table 2.1. Crystal structure and properties of TiO_2

Properties	rutile	anatase	brookite
Crystal structure	tetragonal	tetragonal	orthorhombic
Lattice constants (A°)	a = b = 4.593, c = 2.9587	a = b = 3.784, c = 9.515	a = 9.184, b=5.447 c = 5.145
Density ($g.cm^{-3}$)	4.13	3.79	3.99
Ti-O bond length (A°)	1.949 (4) 1.980 (2)	1.937 (4) 1.965 (2)	1.87~2.04

Different methods have been reported for TiO_2 synthesis such as chemical vapor deposition [37], direct oxidation method [38], ultrasonic irradiation [39], solvothermal [40], hydrothermal and sol-gel. The sol-gel method has attracted a lot of interest due to its simplicity and low cost even though the catalyst synthesized can be highly pure [41]. Many other catalysts have also been synthesized using the sol-gel method such as ZrO_2 [42], $SrTiO_3$ [43], ZnO [44], WO_3 [45] and TiO_2. This method is based on the polymerization of inorganic chemicals in the solution, which includes four steps: 1) hydrolysis 2) polycondensation 3) drying and 4) thermal decomposition [46]. During the hydrolysis and polycondensation, M–OH–M and M–O–M bonds are formed, which eventually produce oxides or hydroxides. The hydrolysis reactions are as follows:

$$Ti(OR)_n + H_2O \rightarrow TiOH(OR)_{n-1} + ROH \qquad \text{Equation 2.1}$$

$$TiOH(OR)_{n-1} + H_2O \rightarrow Ti(OH)_2(OR)_{n-2} + ROH \qquad \text{Equation 2.2}$$

These reactions continue to produce $Ti(OH)_n$. The polycondensation reactions are as follows [41]:

$$-Ti-OH+HO-Ti\rightarrow -Ti-O-Ti-+H_2O$$ Equation 2.3

$$-Ti-OR+HO-Ti\rightarrow -Ti-O-Ti-+ROH$$ Equation 2.4

To slow down the hydrolysis step, resulting into finer crystal size, ethanol and acid are added as well. Different parameters such as the ratio of the reactants, pH, reaction time and temperature affect the morphology of the nanoparticles [47]. The initial sol-gel method was a single step process in which water was added to the titanium alkoxide solution [48]. This led to a non-uniform and big particle with low surface area. A two step process is now used where the titanium alkoxide precursor is dissolved in an alcohol solution and the water is added to this solution drop wise [49]. The catalyst synthesized using the two step process has a uniform morphology with a controlled particle size distribution. It is conventional to use different additives in the sol-gel method to control the shape of the particles. Eiden-Assmann controlled the size distribution by adding salt and polymer solutions to the process. They used alkali halides such as LiCl, NaCl, KCl, CsCl, KBr, KI, diblock-copolymers Lutensol ($RO(CH_2CH_2O)_xH$) and triblock-copolymers Pluronic (PEO_n–PPO_m–PEO_n)) copolymers [50]. The water molecules can be trapped by hydrogen bonds among the organic chains, which leads to micropores in the TiO_2 gel structure. Calcination causes the water molecules to escape from the structure however this step would lead to agglomeration of particles and consequently a reduction in the surface area [41]. By controlling the temperature of the sol-gel method, one can control the structure, crystallite size, and specific surface area. The phase transformation of anatase to rutile is reported to occur at about 600 °C however the transition temperature is reported between 400-1200 °C due to the different influential variables such as impurities, morphology, sample preparation method, etc. [51, 52]. The changes in crystallite size and specific surface area based upon the change in the calcination temperature are presented in Table 2.2 [53]. It should be noted that the grain size of the rutile is significantly larger than that of the anatase due to the fact that the transition from anatase to rutile occurs with grain growth resulting in larger crystals. Hence, anatase has a larger specific surface area compared to the rutile because of its smaller crystallite size.

Table 2.2. Crystallite size (nm) and specific surface area for TiO_2 particles calcined at various temperatures.

Calcined temperature (°C)	Crystallite size (nm)		Specific surface area (m^2/g)
	anatase	rutile	
250	6.8	-	145.8
300	7.3	-	120.1
400	8.9	-	106.9
500	11.3	-	100.7
600	15.1	20.5	64.88
700	17.4	20.5	26.85
900	-	22.7	-

2.2 Photocatalyst, band gap and electron/hole generation

Semiconductors (in our case TiO_2) have a valence band as the highest unoccupied energy band and a conduction band as the lowest occupied energy band. The energy difference between the valence band and the conduction band is called the band gap energy. Photons of light with higher energy than the band gap energy can be absorbed by the photocatalyst. This leads to the excitation of the electrons from the valence band of the semiconductor to the conduction band. As a result, the energy-rich electrons (e^-) and holes (h^+) are generated in the conduction and valence bands, respectively [54]. The energy of these photo-generated charge carriers can be used electrically such as for solar cells or chemically such as for photochemical catalysis. In the case of photocatalytic applications, the charge carriers migrate to the surface and initiate the photocatalytic reactions. The electrons in the conduction band react with the oxygen molecules and produce superoxides ($O_2^{\bullet -}$) and on the other side the holes in the valence band react with the water molecules and produce hydroxyl radicals ($HO^{\bullet}$). Figure 2.1 illustrates the excitation of the electrons upon absorption of ultraviolet (UV) photons. As mentioned, the energy of the absorbed photon must be greater than the band gap energy of the material (in this case 3.2 eV).

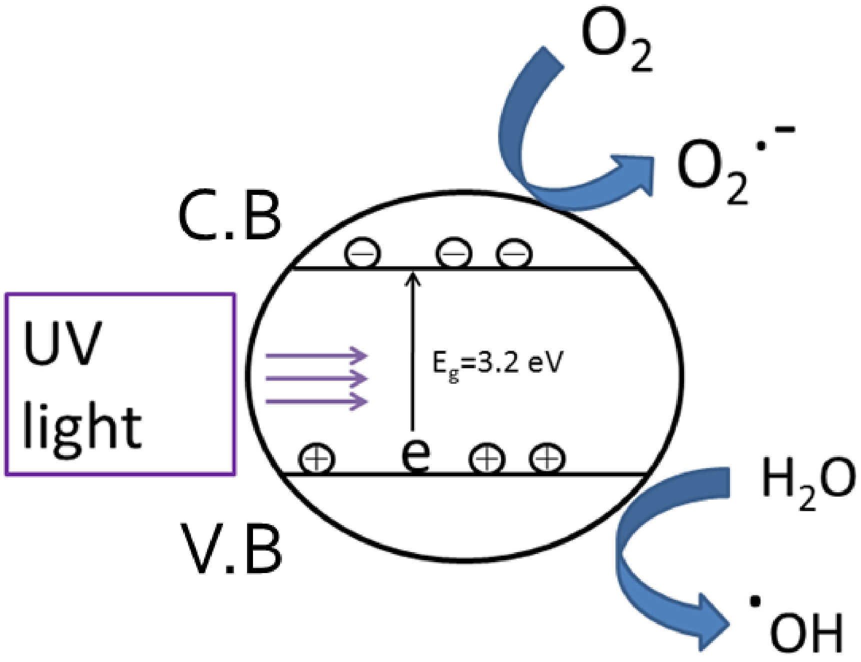

Figure 2.1. The schematic of the conduction band (C.B) and valence band (V.B) in anatase TiO_2, generation of electrons and holes and their reaction with adsorbed oxygen and water molecules to generate superoxide and hydroxyl radicals.

The generated radicals are the species with a free unpaired electron and are the product of the reaction of the adsorbed molecules such as O_2 or H_2O with the charge carriers. The electrons and holes can either recombine or migrate to the surface and initiate the radical generation. The following equations summarize different reactions occurring from the moment that the photon is absorbed by the titania until the carriers reach to the catalyst surface and start the photocatalytic reactions [21, 23]:

$$TiO_2 + h\vartheta \rightarrow e^- + h^+ \qquad \text{Equation 2.5}$$

$$h^+ + H_2O \rightarrow HO^\bullet + H^+ \qquad \text{Equation 2.6}$$

$$O_2 + e^- \rightarrow O_2^{\bullet -} \qquad \text{Equation 2.7}$$

$$O_2^{\bullet -} + H^+ \rightarrow HO_2^\bullet \qquad \text{Equation 2.8}$$

$$HO_2^\bullet + H^+ + e^- \rightarrow H_2O_2 \qquad \text{Equation 2.9}$$

$$H_2O_2 + e^- \rightarrow HO^\bullet + HO^- \qquad \text{Equation 2.10}$$

$$HO^- + h^+ \rightarrow HO^\bullet \qquad \text{Equation 2.11}$$

$$HO^\bullet + organic\ pollution \rightarrow intermidistes \rightarrow CO_2 + H_2O \qquad \text{Equation 2.12}$$

It should be mentioned that water molecules are crucial for the generation of hydroxyl radicals.

2.3 Transition metals as dopants

As described, TiO_2 is a great candidate for photocatalytic reactions. However, there are some problems using it in photocatalytic reactions. They include a) the electron/hole recombination rate is high, which results into lower photocatalytic activity since the electrons and holes do not have enough time to migrate to the surface and initiate the photocatalytic reactions, b) the large band gap energy of anatase TiO_2 limits its photocatalytic applications only to UV light irradiation [21, 55-57]. The UV light is expensive and requires high safety precautions, whereas, activation under visible light will provide the opportunity to use solar light as the free source of energy.

It has been reported that introducing metals as the dopants into the crystal lattice of titania can trap both electrons and holes temporarily and hence reduce the electron/hole recombination and cause an increase in the photocatalytic activity [58, 59]. Meanwhile, the interaction of the *d* orbital of the metal dopant and 3*d* orbital of Ti introduces intra-band gap states, which leads to a red shift towards longer wavelengths in the light absorption [21, 60]. Different transition metals have been used as dopants to modify the band gap energy and electron/hole recombination rate of titania [61]. Cr^{3+} acts as a trap for holes to increase the lifetime of the charge carriers. The trapped holes in Cr^{4+} migrate to the surface and generate hydroxyl radical through the reaction with hydroxyl groups as follows [62]:

$$Cr^{3+} + h^{+} \rightarrow Cr^{4+} \qquad \text{Equation 2.13}$$

$$Cr^{4+} + HO^{-} \rightarrow Cr^{3+} + HO^{\bullet} \qquad \text{Equation 2.14}$$

It has been reported that Tungsten (W) introduces two unoccupied states and Vanadium (V) introduces a single occupied state below the conduction band. Hence, W can decrease the recombination rate more than V since the electrons require more processes to recombine with the holes. Mn^{3+} and Mn^{4+} possess both occupied and unoccupied states and trap both electrons and holes in their intermediate band gap region. However, since the electrons and holes are trapped on the same sites, the Mn ion increases the electron/hole recombination rate. The occupied states of the Cu^{+} and Cu^{2+} are positioned close to the valence band enabling the Cu ions to trap holes [63]. Fe^{3+} has a very similar ionic radius to Ti^{4+} and can substitute for Ti^{4+} in the crystal lattice of TiO_2 [64]. Fe^{3+} reduces the electron/hole recombination rate significantly since it can trap both electrons and holes.

More importantly, the occupied states of Ti^{4+}/Fe^{3+} are positioned 0.5-0.8 eV above the valence bond and the unoccupied states are positioned 0.7 eV below the conduction band. This suggests that the electron/hole separation using Fe^{3+} can occur effectively resulting to a higher lifetime of the charge carriers [65]. On the other hand, Fe^{2+} and Fe^{4+} are less stable than Fe^{3+} and based upon the crystal field theory by gaining or losing an electron would eventually return to the Fe^{3+} state. Therefore, the electron and hole will be released enabling it to migrate to the surface of the catalyst [59, 66]. The mechanism of electron/hole trapping and their passing to the surface to generate radicals are described as follows [21]:

$$TiO_2 + h\vartheta \rightarrow e^- + h^+ \qquad \text{Equation 2.15}$$

$$Fe^{3+} + h^+ \rightarrow Fe^{4+} \qquad \text{Equation 2.16}$$

$$Fe^{3+} + e^- \rightarrow Fe^{2+} \qquad \text{Equation 2.17}$$

$$Fe^{2+} + O_2 \rightarrow Fe^{3+} + O_2^{\bullet -} \qquad \text{Equation 2.18}$$

$$Fe^{2+} + Ti^{4+} \rightarrow Fe^{3+} + Ti^{3+} \qquad \text{Equation 2.19}$$

$$Ti^{3+} + O_2 \rightarrow Ti^{4+} + O_2^{\bullet -} \qquad \text{Equation 2.20}$$

$$Fe^{4+} + e^- \rightarrow Fe^{3+} \qquad \text{Equation 2.21}$$

$$Fe^{4+} + HO^- \rightarrow Fe^{3+} + HO^{\bullet} \qquad \text{Equation 2.22}$$

Figure 2.2 illustrates the intermediate band gaps, which are formed by the interaction of the d orbitals of Fe and 3d orbitals of Ti making it possible to absorb photons with less energy than 3.2 eV. These trapped electrons and holes migrate to the surface of the catalyst to react with the adsorbed oxygen and water molecules to generate the superoxide and hydroxyl radicals.

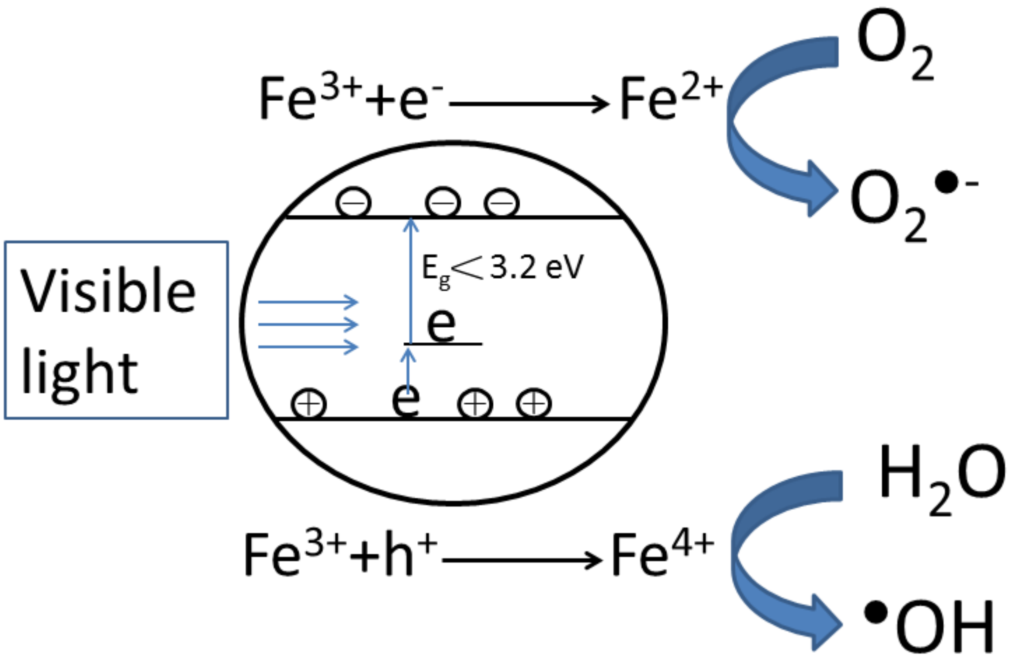

Figure 2.2. Schematic of Fe-TiO_2 and electron/hole traps for charge separation. The trapped electrons and holes are released to generate superoxide and hydroxyl radicals.

2.4 Photocatalysis, photocatalytic activity and kinetics study

The photosensitization of TiO_2 was first discovered by K. Honda and A. Fujishima in 1972. They found when using TiO_2 as a photoanode the electrolysis of water into hydrogen and oxygen under UV light irradiation occurred at a lower bias voltage [67]. Later in 1977, G. N. Schrauzer and T. D. Guth reported the photocatalytic decomposition of water using a powder of TiO_2 assisted with small amounts of Pt or Rh [68]. Then, the idea was developed that the generated electrons migrate to the Pt metal where they initiate the reduction reactions and the holes stay in TiO_2 and migrate to the surface and induce the oxidation reactions [69]. The photo-generated charge carriers (electrons and holes) play a critical role in photo degradation of organic pollutants. The degradation of organics takes place by hydroxyl radicals ($HO^{\bullet}$), holes (h^{+}), superoxide ions ($O2^{\bullet-}$) and hydroperoxyl radical ($HOO^{\bullet}$), which oxidize a large variety of organic compounds [70]. Hence, one of the methods to measure the photocatalytic activity is to measure the degradation of organic pollutants in water. In this case, a known amount of pollutant is added to water and the concentration of the pollution before and after the treatment process is measured. The percent DE ($X\%$) is usually obtained as follows:

$$X\% = \frac{C_0 - C_C}{C_0} \times 100 \qquad \text{Equation 2.23}$$

where C_0 and C_c are the initial and final concentrations of the pollutant, respectively.

The kinetics of the heterogeneous photocatalytic degradation usually follows the Langmuir-Henshelwood model as follows:

$$r = -\frac{dC}{dt} = \frac{kKC}{1+KC} \qquad \text{Equation 2.24}$$

where r represents the rate of the degradation reaction, C is the concentration of the pollutant, t is the reaction time, k is the rate constant of the reaction and K is the adsorption coefficient of the pollutant. If the concentration of the pollutant is extremely low, the above equation can be simplified to:

$$\frac{lnC_0}{C} = kKt = K_{app}t \qquad \text{Equation 2.25}$$

where K_{app} is the apparent first order rate constant, which can be obtained by plotting lnC_0/C vs t [70].

2.5 Contamination sources: methyl orange and phenol

A large volume of dyes is consumed in the textile industry for wet processing of textiles. The existence of a very low amounts of dye in effluent is highly visible. More than 7×10^5 tons of 100,000 different types of dyes are being produced annually. Most of the dyes are very difficult to decompose due to their complex structure. Different types of dyes include acidic, basic, azo, diazo, metal complex dyes, etc. Aerobic methods do not treat and decompose the textile dye effluents in the municipal sewerage systems [71]. Azo dyes are the most common type of dyes in the textile, food, paper, printing and cosmetic industries [72]. Therefore, one of the pollutant representatives chosen for this research was methyl orange, which is an azo type of dye. The chemical structure of methyl orange is shown in Figure 2.3 [73]:

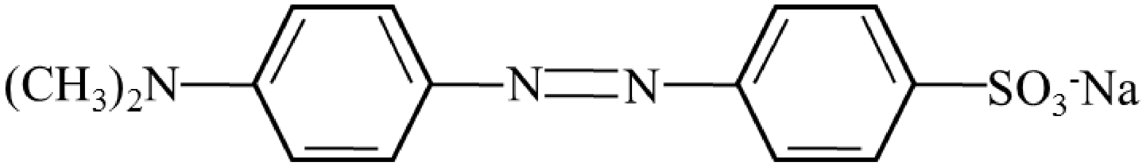

Figure 2.3. Structural formula of methyl orange.

The other pollutant used in the degradation experiments was phenol. Phenol (hydroxybenzene) is a crystalline, colorless material with a special odor. It is soluble both in water and organic solvents. Phenol is a toxic chemical as stated in the List of Priority Pollutants by the US Environmental Protection Agency (US EPA). Phenol is used in numerous industries such as oil, coal, metallurgic, petrochemical, chemical, pharmaceutical, pulp and paper [74, 75]. Due to the low biodegradability of these compounds, the conventional biological degradation processes are not efficient in removing them from the effluent. Therefore, AOP methods as a very efficient alternative are promising for the reduction or complete mineralization of these toxic organic compounds [76]. The chemical structure of phenol is shown in Figure 2.4 [74]:

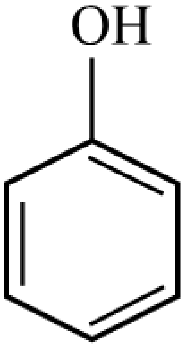

Figure 2.4. Structural formula of phenol compound

Chapter 3 Significant improvement in visible light photocatalytic activity of Fe doped TiO_2 using an acid treatment process

This paper was published at Journal of applied surface science [33].

Vahid Moradi, Martin B.G. Jun , Arthur Blackburn and Rodney A. Herring

ABSTRACT

Transition metal dopants have been used to decrease the band gap energy of TiO_2 for visible light photocatalytic purposes. Fe^{3+} is a good dopant candidate owing to its capability to decrease the band gap energy and enhance the electron/hole trapping. However, in previous studies the photocatalytic activity of Fe-TiO_2 was around 40-50% for a reaction time of ~300 min. Herein, using HRTEM it was found out that the photocatalytic activity of Fe-TiO_2 is limited by an amorphous contamination layer on the surface of the Fe-TiO_2 nanoparticles. The contamination layer was determined to be composed of iron oxide by XPS surface analysis. The contamination layer was successfully removed using an acid treatment process comprising of HCl solution. Using the cleaned Fe-TiO_2 nanoparticles, the photocatalytic activity measured utilizing a solution of 20 mg.L^{-1} methyl orange (MO) was significantly increased from 24% to 98% within 60 min of reaction time under visible light illumination.

KEYWORDS: Fe doping, transition metal, TiO_2 photocatalyst, visible light, acid treatment

3.1 Introduction

Anatase titanium oxide (TiO_2) has been widely studied for the past few decades for its photocatalytic applications such as water purification, water splitting and solar cells due to its low cost, high chemical stability and excellent charge transport ability [34, 59, 77-80]. However, because of its large band gap energy (~3.2 eV), it performs poorly as a photocatalyst under visible light, which limits its applications [81-83]. Doping TiO_2 with transition metal ions can improve its photocatalytic activity under visible light illumination [31, 84-87]. Firstly, it is believed that the interaction of the 3d orbital of Ti and the d orbital of a transition metal introduces an intra-band gap state that causes a decrease in the band gap energy, which leads to a red shift (longer wavelengths) in absorption of a photon [31, 32, 88-91]. Secondly, metal dopants incorporated into the crystal lattice of TiO_2 inhibit electron/hole recombination, which, due to the effective separation of the charge carriers, enhances the photocatalytic activity [30, 31, 92, 93]. Metal dopants trap both electrons and holes, leading to the increased life time of the charge carriers, which enhances their chance to reach the catalyst's surface to initiate the photocatalytic reactions [94, 95]. Fe^{3+} has been reported as a suitable dopant for TiO_2 because the radius of Fe^{3+} (0.645 $\overset{\circ}{A}$) is very close to that of Ti^{4+} (0.604 $\overset{\circ}{A}$) [64]. Moreover, it has been reported that among the transition metals, Fe^{3+} can inhibit electron/hole recombination the best by trapping both the photo-generated electrons and holes creating Fe^{2+} and Fe^{4+}, respectively, to enhance the photocatalytic efficiency [92, 96]. Many studies have been conducted to investigate the role of Fe^{3+} as the dopant of TiO_2 (Fe-TiO_2) on its photocatalytic activity under visible light illumination using organic dyes. Table 3.1 shows the studies conducted on the degradation efficiency of Fe-TiO_2 nanoparticles using MO solution as a pollutant model without utilizing any oxidant such as H_2O_2.

Table 3.1. Photocatalytic activity of Fe-TiO_2 on the degradation of MO under visible light illumination.

Catalyst (mg.L^{-1})	MO (mg.L^{-1})	Reaction time (min)	Light source	Optical filter	Degradation efficiency%	Reference
1000	50	240	150 W metal halide	410 nm	20	[97]
1000	5	300	105 W fluorescent	-	5	[58]
1000	10	175	400 W metal halogen	420	55	[98]
2000	3.2	300	500 W tungsten iodide	420	52	[99]
2000	3.2	420	300 W halogen	420	39	[100]
714	10	540	300 W xenon	400	54	[101]
10000	20	150	1000 W tungsten halogen	420	40	[102]
1000	8	60	300 W xenon	420	22	[103]
1000	20	300	1000 W tungsten halogen	420	30	[104]
1000	20	360	300 W halogen tungsten	400	50	[105]
500	20	60	300 W xenon	400	98	This work

According to the high potential of Fe^{3+} in decreasing the band gap energy and its ability to trap the charge carriers (both electron and hole), we believed that the degradation efficiency could be improved further with adjustments in the catalyst preparation. Using XPS and atomic absorption spectroscopy indicated that the surface concentration of Fe^{3+} (deposited on the surface of TiO_2 particles as iron oxide) is significantly higher than the bulk Fe^{3+} concentration (doped Fe^{3+} in the crystal lattice) [106]. These surface Fe^{3+} ions in the iron oxide were believed to act as recombination centers for the photocatalytic generated electrons and holes in the Fe-TiO_2 [107-109]. Moreover, we suspected that the deposited iron oxide layer on the surface of the Fe-TiO_2 particles contaminates its surface reducing the accessible active sites for the photocatalytic reactions. To the best of our knowledge, no study has been conducted to remove this surface contamination layer to investigate its effect on the photocatalytic activity. Therefore, in the present work hydrochloric acid (HCl), which is an effective solvent for hematite and magnetite species [110, 111], was employed to remove the surface iron oxide contamination layer. As a result of this HCl acid treatment process, the degradation of MO under visible light irradiation showed a significant increase in the photocatalytic efficiency, reported herein.

3.2 Experimental

3.2.1 Synthesis

All the reagents were of analytical grade used without any further purification. Deionized water was used throughout the synthesis steps. The catalysts were prepared by a simple sol-gel method using titanium isopropoxide (TTIP) as the precursor and ferric nitrate ($Fe(NO_3)_3.9H_2O$) as the Fe^{3+} source purchased from Sigma-Aldrich. The desired amount of ferric nitrate (0.25, 0.5, 1, 5 and 10 Fe:Ti molar% ratio) was dissolved in deionized water at a ratio of Ti:H_2O (1:4). The solution was added to 30 mL of anhydrous ethyl alcohol and stirred for 10 minutes. If an acidic synthesis pH was required, the pH was adjusted by adding nitric acid (HNO_3) in this step. Then, TTIP was added dropwise to the solution under vigorous stirring and the mixture was stirred using a magnetic stir bar for 2 hours at room temperature and then dried at 80 °c for 2 hours. The dried powder was then centrifuged and washed 3 times with deionized water to remove a carbon residual that contaminates the surface and then calcined at 400 °c (temperature ramp of 10 $°C.min^{-1}$) for 3 hours. After calcination, the catalyst particles were stirred in concentrated HCl solution (pH~2) for 3 hours, centrifuged and washed with deionized water 3 times to remove the possible chlorine residuals. The residue solution turned brownish ascribed to the dissolution of the iron oxide from the surface of the Fe-TiO_2 particles.

3.2.2 Material characterization

The TEM images were obtained using a JEOL JEM-1400 electron microscope and HRTEM and selected area electron diffraction (SAED) patterns were obtained by a Hitachi HF-3300V to having spherical aberration, Cs plus coma correction for its Transmission Electron Microscopy mode. A Cary 100 UV-vis spectrometer was used to obtain the UV-vis absorption spectra of MO. An Omicron & Leybold MAX200 X-ray Photoelectron Spectrometer (XPS) and PANalytical Empyrean X-ray diffractometer (XRD) with copper X-ray lamp, Kα ($A°$) = 1.54 were used to obtain the XPS spectra and XRD patterns, respectively. A Lambda 1050 UV-vis/NIR spectrometer was used to obtain the diffuse reflectance spectra (DRS) and light absorption of the catalyst particles.

A Cermax PE300BUV Xenon arc lamp (300 W) with a cut off filter (λ> 400 nm) was used as the light source to measure the photocatalytic activity.

2.3. Photocatalytic Experiments

The photocatalytic activity experiments were carried out using a 20 mg.L^{-1} MO solution as the pollutant. A 300 W xenon lamp with a UV cut off filter (λ> 400 nm) was used as the visible light source. The experiments were carried out in a 200 mL beaker containing 100 mL of solution. The catalyst was added to the MO solution and stirred for 30 min in dark to reach the adsorption equilibrium. While the lamp was turned on samples were taken in the desired time intervals within 60 min of reaction time. The change in the concentration of MO was measured using UV-vis absorption spectroscopy at the maximum absorption wavelength of 466 nm.

The degradation efficiency was measured using the following equation:

$$X\% = \frac{C_0 - C_C}{C_0} \times 100 \qquad \text{Equation 3.1}$$

where, $X\%$ is the degradation efficiency, C_0 and C_c are the initial and final concentrations of MO, respectively.

3.3 Results and Discussion

3.3.1 Characterization

XRD was used to determine the phase structure and crystallite size of the particles. Figure 3.1 shows the XRD patterns of bare TiO_2 and Fe-TiO_2 with different iron contents. The peak at 25.3 2θ degrees corresponds to the main anatase peak (101) and the other peaks correspond to (004), (200), (105), (211), (204), (116), (220) and (215) planes [111-

113]. It is noteworthy to mention that the rutile phase with the main peak at 27.45° corresponding to (110) was not found in any of the samples. The crystallinity decreased gradually for an increase in the Fe doping content. The average crystallite size of the particles was determined from the broadening of the XRD peaks applying the Scherrer equation [114, 115]. It was observed that adding Fe^{3+} to the crystal lattice decreased the crystallite size and 13, 10.0, 9.7, 9.3, 6.4 and 5.9 nm of crystallite size were obtained for bare TiO_2, $Fe_{0.25}$-TiO_2, $Fe_{0.5}$-TiO_2, Fe_1-TiO_2, Fe_5 -TiO_2 and Fe_{10}-TiO_2, respectively. Also, $Fe_{0.5}$-TiO_2 was synthesized in acidic pH (~3) as well as the natural pH. It was observed that the crystallite size decreased from 9.3 nm to 8.0 nm showing that the size decreases by synthesizing the nanoparticles in acidic pH. The latter is due to the fact that the acidic pH slows down the hydrolysis step resulting in finer catalyst particles [116, 117]. It should be mentioned that the acid treatment process did not affect the crystallite size. It is noteworthy to mention that a peak for α-Fe_2O_3 was not observed in any of the spectra suggesting that either iron oxide is formed as an amorphous phase or exists as a very thin layer on the surface of the catalyst particles insufficient to be characterized by XRD.

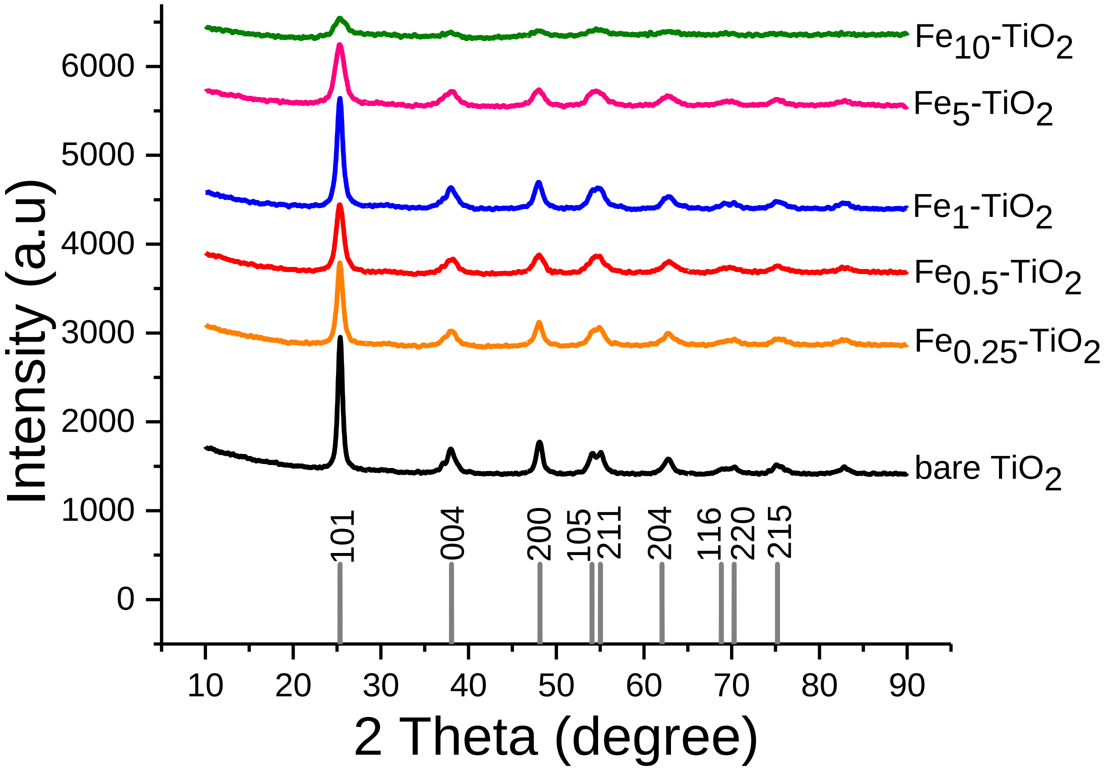

Figure 3.1. XRD pattern of bare TiO_2 and Fe-TiO_2 with different iron content (0.25, 0.5, 1, 5 and 10 Fe:Ti molar% ratio) calcined at 400 °c for 3 hours.

SAED was used to study the d-spacing of the nanoparticles (shown in Figure 3.6 in supporting information). As it is illustrated in Table 3.2, the lattice parameter was increased by doping Fe^{3+}. Since the ionic radius of Fe^{3+} is larger than that of Ti^{4+}, the lattice parameter enlarges upon corporation of Fe^{3+} [64]. Also, it was observed that the lattice parameter did not change before and after the acid treatment.

Table 3.2. Lattice parameters measured using SAED.

Sample		a = b (Aº) (± 0.003)	c (Aº) (± 0.005)
bare TiO_2	untreated	0.376	0.935
bare TiO_2	acid treated	0.377	0.948
$Fe_{0.5}$-TiO_2		0.399	1.004
Fe_1-TiO_2		0.391	0.980
Fe_5-TiO_2		0.397	1.004

TEM images of the untreated and acid treated $Fe_{0.5}$-TiO_2 particles synthesized at a pH of 3 showed that the particles have a uniform size distribution of about 10 nm (Figure 3.2a and 2b) consistent with the XRD determination. An amorphous layer can be observed around the untreated $Fe_{0.5}$-TiO_2 particles (Figure 3.2a). After the acid treatment (Figure 3.2b), the amorphous layer is mostly removed from the surface of the $Fe_{0.5}$-TiO_2 particles. This amorphous layer is more obvious in the HRTEM images of untreated Fe_{10}-TiO_2 particles defined by the red dashed outlines (Figure 3.2c). After treating the particles with the HCl solution, the amorphous layer was mostly removed and the crystal planes can be seen to extend to the surface of the particles (Figure 3.2d). It should be mentioned that the amorphous layer was also observed for some of the acid treated particles but it was negligible compared to the untreated ones.

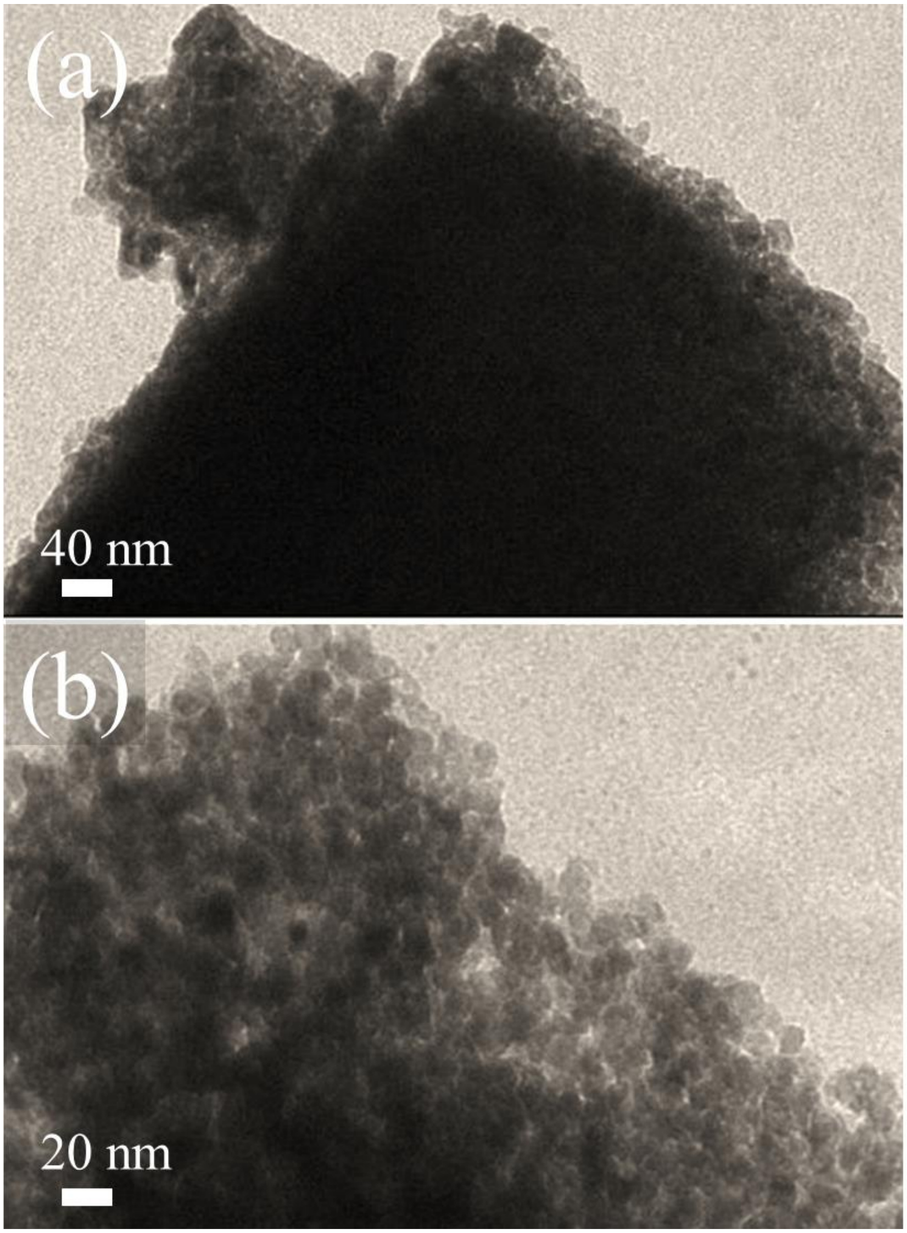
(a)
40 nm
(b)
20 nm

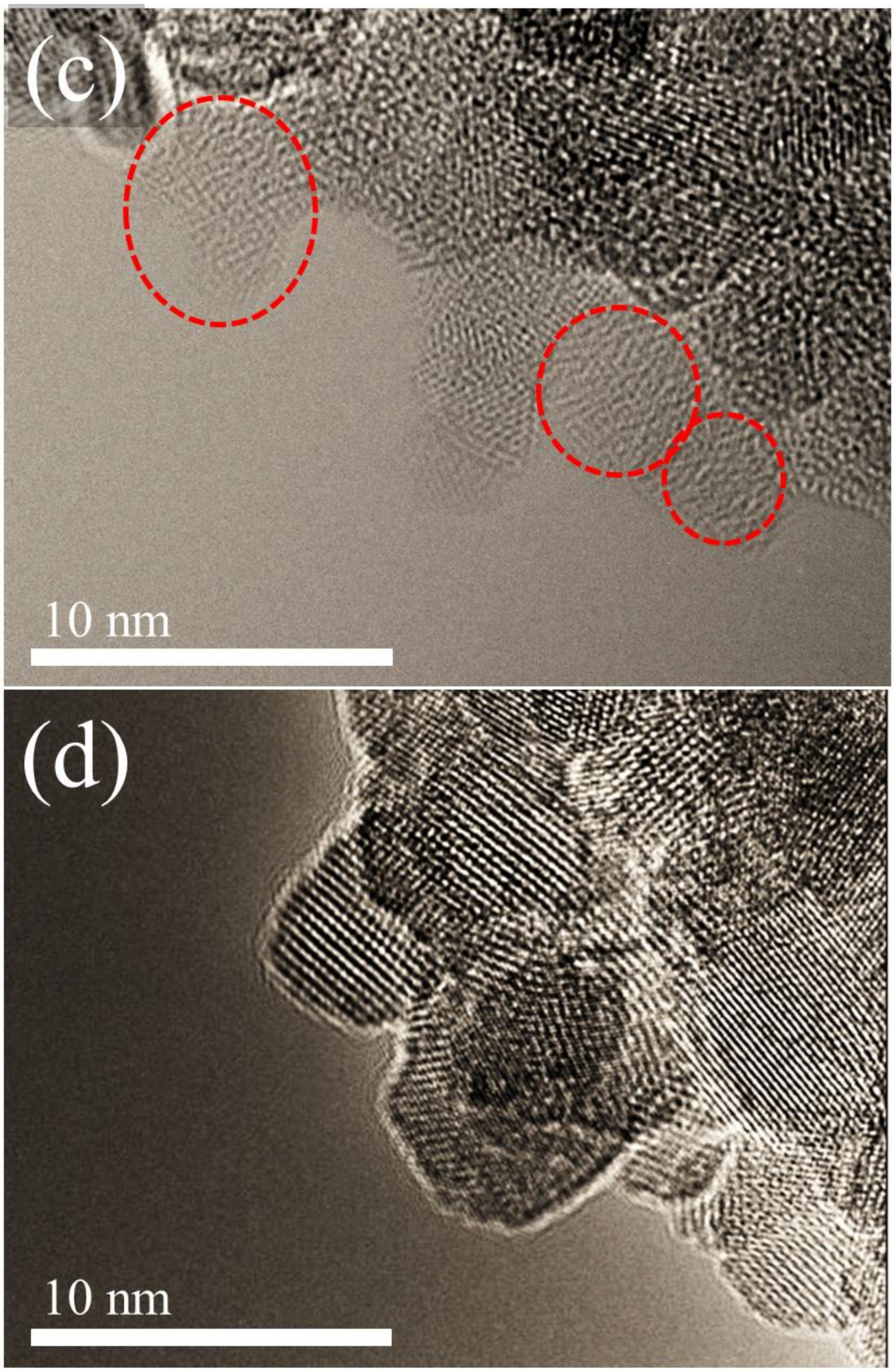

Figure 3.2. TEM images of a) untreated and b) acid treated $Fe_{0.5}$-TiO_2 particles and HRTEM images of c) untreated and d) acid treated Fe_{10}-TiO_2. The red dashed outlines in c) show amorphous areas surrounding the Fe_{10}-TiO_2 particles that were mostly removed by the HCl treatment seen in d) having the crystal planes extending to the surface.

X-ray photoelectron spectroscopy (XPS), a sensitive surface characterization technique, was employed to analyze the surface chemical composition. The survey scans of Fe_{10}-TiO_2 (Figure 3.3 a, b), and $Fe_{0.5}$-TiO_2, Fe_1-TiO_2 and Fe_5-TiO_2 (Figure 3.7 in supporting information)**,** show no trace of nitrogen, derived from the nitrate in $Fe(NO_3)_3.9H_2O$, as well as, no chlorine from treating the catalyst with HCl solution on any of the particles. It was shown that the surface is mostly composed of Fe, O and Ti. Hence, it can be concluded that the amorphous layer seen by the HRTEM was either TiO_2 or iron oxide.

Table 3.3 illustrates the change in atomic% (at.%) of Ti, O and Fe elements of Fe-TiO_2 with different doping content before and after acid treatment. Fe:Ti at.% ratio of Fe_1-TiO_2 (0.27:18.72), Fe_5-TiO_2 (0.88:17.39) and Fe_{10}-TiO_2 (1.33:15.55) show that the ratios are very close to the initial precursor amounts used to synthesize the catalysts. The iron amount in $Fe_{0.5}$-TiO_2 particles was not enough to be identified (Figure 3.7 in supporting information). The survey scans clearly show that the at.% of surface iron significantly decreased after treating the catalyst particles with HCl solution, whereas, that of Ti did not change significantly. Therefore, one can conclude that the amorphous layer removed by the acid treatment was mostly related to the iron oxide layers on the surface. The bulk iron, doped in crystal lattice of TiO_2, is not affected by the acid treatment. Hence, the decrease in the iron content is related to the removal of the iron oxide layers on the surface of the particles consistent with the observations by HRTEM and with the brownish color observed in the residue solution after the acid treatment. Figure 3.3 (c, d) depicts the spectra for Fe 2p of Fe_5-TiO_2 for untreated and acid treated samples. The Fe $2p_{3/2}$ of the untreated sample peaks are located at 709.3, 710.6, 711.9, 713.7 eV and the signal for Fe $2p_{1/2}$ appears around 725 eV. Considering the common variations of the binding energies**,** these peaks are in very good agreement with the ones observed for Fe_3O_4 [106, 107] and Fe_2O_3 [118-120]. The O 1s signal of untreated and acid treated Fe_5-TiO_2 are similar (Figure 3.3 e, f) and indicated a peak at 530.2 eV attributed to Fe_2O_3 (530.0 [121, 122] and 529.9 eV [123]), TiO_2 (530.0 [124]) and Fe_3O_4 (530.3 [123] eV). Another peak observed at 532.1 eV is assigned to the oxygen of the surface H_2O [125]. Figure 3.3 (g, h) illustrates the high resolution scan of Ti 2p for untreated and acid treated Fe_5-TiO_2. The Ti 2p deconvolution led to four peaks; the peaks around 463 and 464 eV are attributed to Ti^{3+} $2p_{1/2}$ and Ti^{4+} $2p_{1/2}$, and the ones around 457 and 458 eV are ascribed to Ti^{3+} $2p_{3/2}$ and Ti^{4+} $2p_{3/2}$ valence state of Ti [120, 125-130]. The existence of Ti^{3+} is due to the oxygen vacancy, where the electrons from the oxygen convert Ti^{4+} into Ti^{3+} to preserve charge neutrality [131, 132]. The high resolution scans of Fe, O and Ti in Fe_{10}-TiO_2 (Figure 3.8 in supporting information) show the same results as well. After deconvolution of the bare TiO_2 (Figure 3.3 i), two peaks were observed at 458.7 and 464.3 eV representing Ti^{4+} $2p_{3/2}$ and $2p_{1/2}$, respectively [133]. Ti^{3+} peaks did not appear in the bare TiO_2 sample showing that either it is not formed or its amount is very low making it difficult to identify.

Table 3.3**.** The at.% of C, O, Ti and Fe in Fe-TiO_2 with different Fe^{3+} content before and after acid treatment. (Un.T term is used for untreated and Ac.T term is used for acid treated samples)

Catalyst	C		O		Ti		Fe	
	Un.T	Ac.T	Un.T	Ac.T	Un.T	Ac.T	Un.T	Ac.T
Fe_1-TiO_2	35.60	40.13	45.41	42.13	18.72	17.61	0.27	0.13
Fe_5-TiO_2	37.36	49.45	44.37	36.18	17.39	13.97	0.88	0.40
Fe_{10}-TiO_2	40.66	46.13	42.46	38.82	15.55	14.27	1.33	0.77

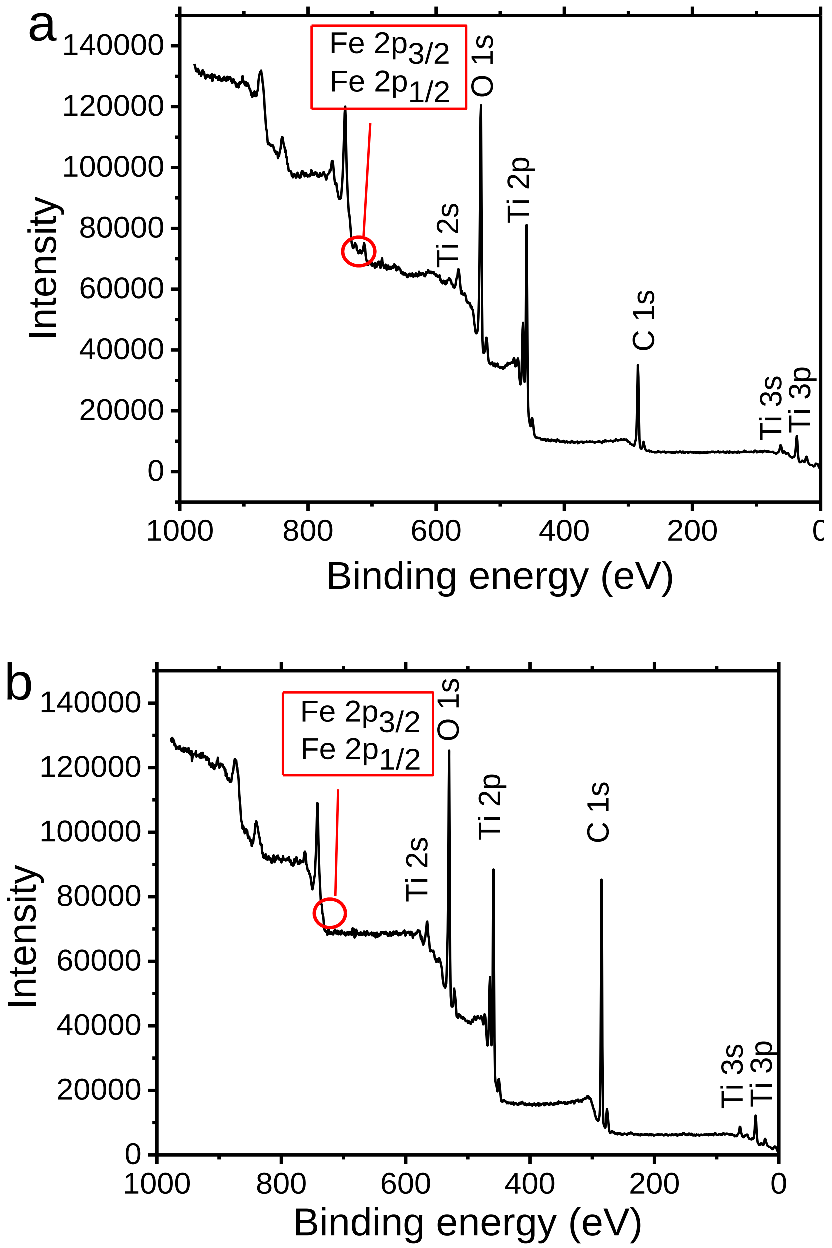
a
Fe 2p3/2
Fe 2p1/2
O 1s
Ti 2p
Ti 2s
C 1s
Ti 3s
Ti 3p
140000
120000
100000
80000
60000
40000
20000
0
Intensity
1000
800
600
400
200
Binding energy (eV)
b
Fe 2p3/2
Fe 2p1/2
O 1s
Ti 2p
Ti 2s
C 1s
Ti 3s
Ti 3p
140000
120000
100000
80000
60000
40000
20000
0
Intensity
1000
800
600
400
200
0
Binding energy (eV)

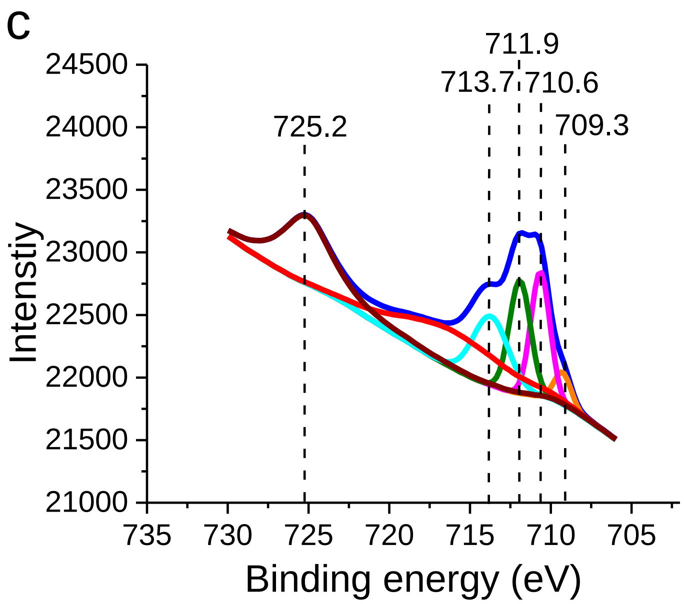
c
711.9
713.7
710.6
725.2
709.3
Intenstiy
24500
24000
23500
23000
22500
22000
21500
21000
735
730
725
720
715
710
705
Binding energy (eV)

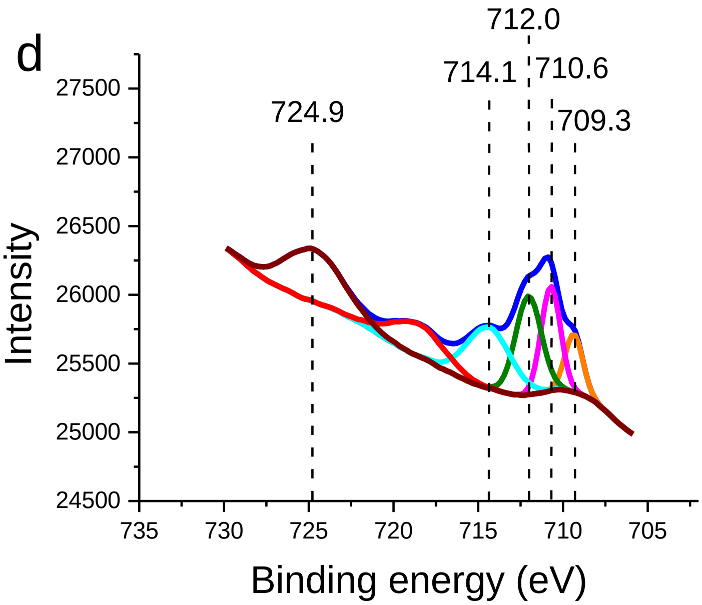
d
712.0
714.1
710.6
724.9
709.3
Intensity
27500
27000
26500
26000
25500
25000
24500
735
730
725
720
715
710
705
Binding energy (eV)

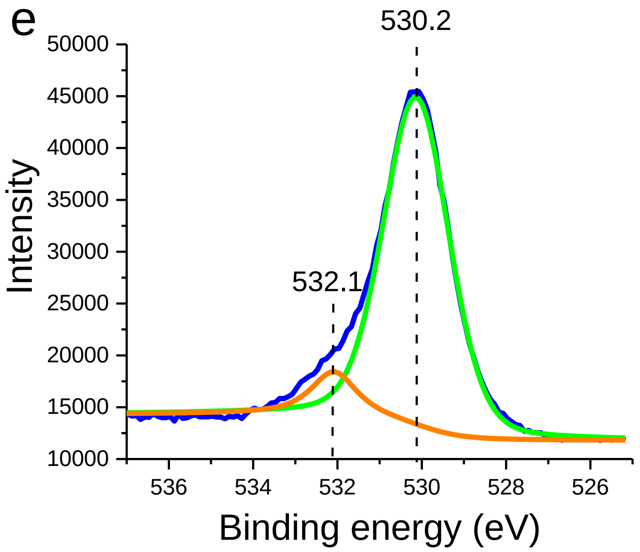
e
530.2
532.1
Intensity
50000
45000
40000
35000
30000
25000
20000
15000
10000
536
534
532
530
528
526
Binding energy (eV)

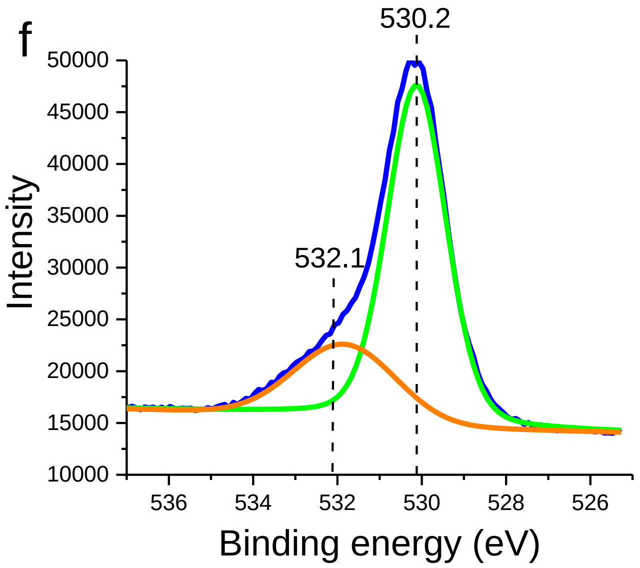
f
530.2
532.1
Intensity
50000
45000
40000
35000
30000
25000
20000
15000
10000
536
534
532
530
528
526
Binding energy (eV)

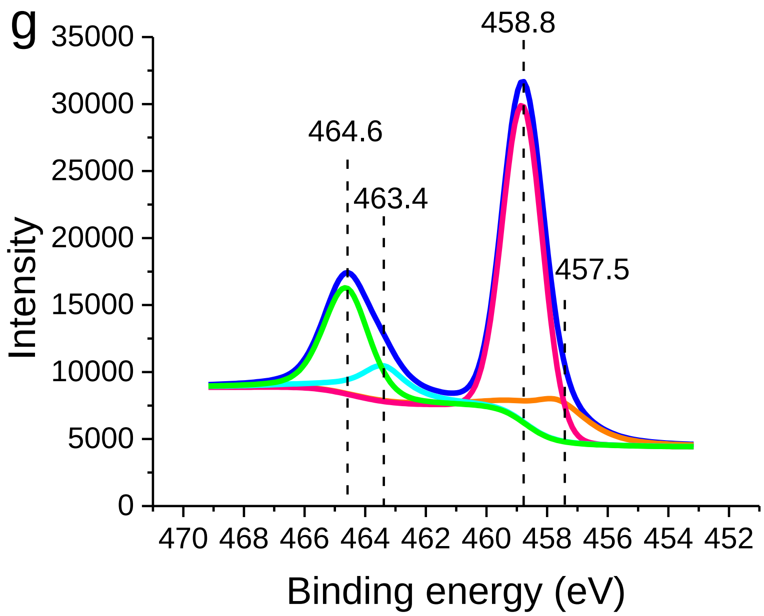
g
458.8
464.6
463.4
457.5
Intensity
35000
30000
25000
20000
15000
10000
5000
0
470 468 466 464 462 460 458 456 454 452
Binding energy (eV)

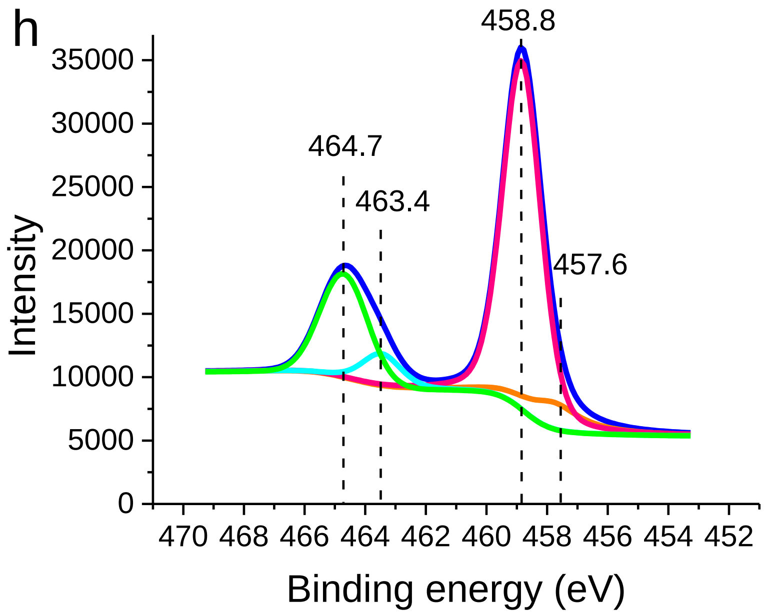
h
458.8
464.7
463.4
457.6
Intensity
35000
30000
25000
20000
15000
10000
5000
0
470 468 466 464 462 460 458 456 454 452
Binding energy (eV)

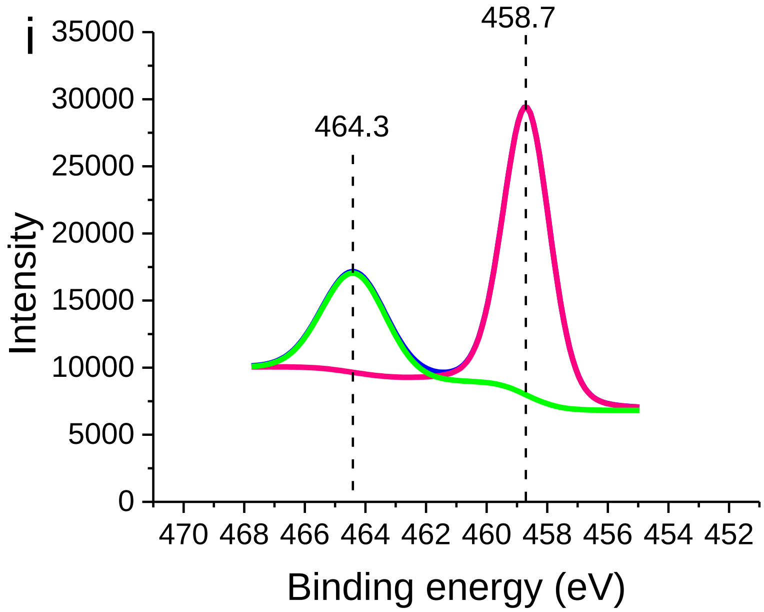

Figure 3.3. XPS survey scan of a) untreated and b) acid treated Fe_{10}-doped TiO_2; Fe 2p high resolution XPS of c) untreated and d) acid treated Fe_5-TiO_2; O 1s high resolution XPS of e) untreated and f) acid treated Fe_5-TiO_2; Ti 2p high resolution XPS of g) untreated and h) acid treated Fe_5- TiO_2; and i) Ti 2p high resolution XPS of bare TiO_2.

The optical properties of bare TiO_2, untreated and acid treated Fe-TiO_2 using diffuse reflectance spectroscopy (DRS) are depicted in Figure 3.4 (a, b). Bare TiO_2 did not show any absorption within the visible light region whereas the Fe-TiO_2 specimens significantly showed a red shift depending on the amount of doping content. The catalyst with the highest iron content showed the highest shift towards longer wavelengths. As the ratio of iron was increased, the number of absorbed photons in the longer wavelength range increased as did the absorption edge between 400 – 650 nm. Such decrease in the band gap energy is attributed to the interaction of the 3d orbital of Ti and d orbital of Fe introducing intra-band gap states that lead to the red shift in the absorption of light [21, 60, 134]. Furthermore, another absorption band was observed around 500 nm attributed to the d-d transitions of ${}^2T_{2g} \rightarrow {}^2A_{2g}$, ${}^2T_{1g}$ of Fe^{3+} [135, 136]. The band gap energy was measured using the well-known Tauc function and a good linear fit was obtained using $(Ahv)^2 \propto (hv - E_g)$, where A is the absorbance and hv is the photon energy and the band gap was measured by extrapolating the linear portion of the curve [137-139]. The band gap energies of untreated and acid treated samples are shown in Figure 3.4 (c, d). The bare TiO_2 band gap energy is 3.3 eV, which corresponds to the direct interband transition [139]. The band gap decreased upon adding Fe^{3+}, and the acid treated Fe-TiO_2 samples showed about ~ 0.1 eV shift toward lower band gaps compared to the untreated ones, which might be due to the removal of surface iron oxide.

In conclusion, the XRD patterns showed that the anatase is the only phase formed and by the increase in the Fe^{3+} content, the crystallite size decreased. Also, HRTEM images showed an amorphous layer contaminating the surface of nanoparticles. Using XPS characterization technique, it was shown that the contaminating layer was composed of iron oxide species. The removal of this contaminating layer was confirmed using HRTEM and XPS.

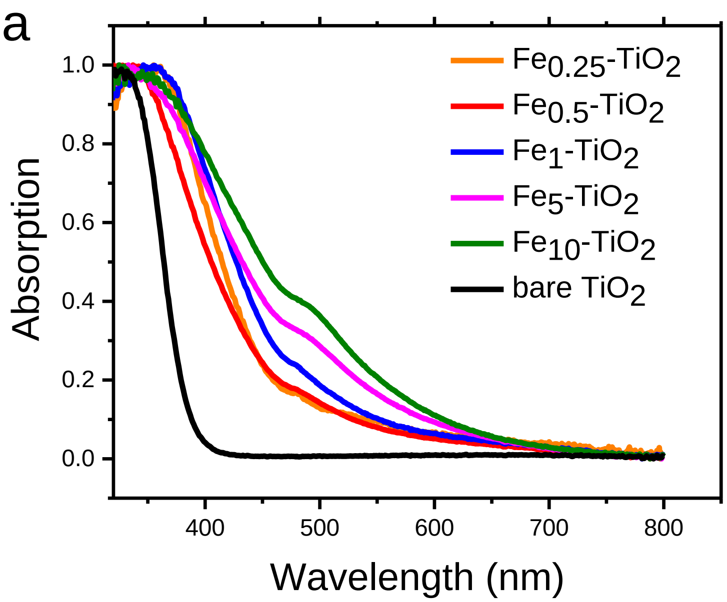
a
Absorption
Wavelength (nm)
1.0
0.8
0.6
0.4
0.2
0.0
400
500
600
700
800
$Fe_{0.25}$-TiO_2
$Fe_{0.5}$-TiO_2
Fe_1-TiO_2
Fe_5-TiO_2
Fe_{10}-TiO_2
bare TiO_2

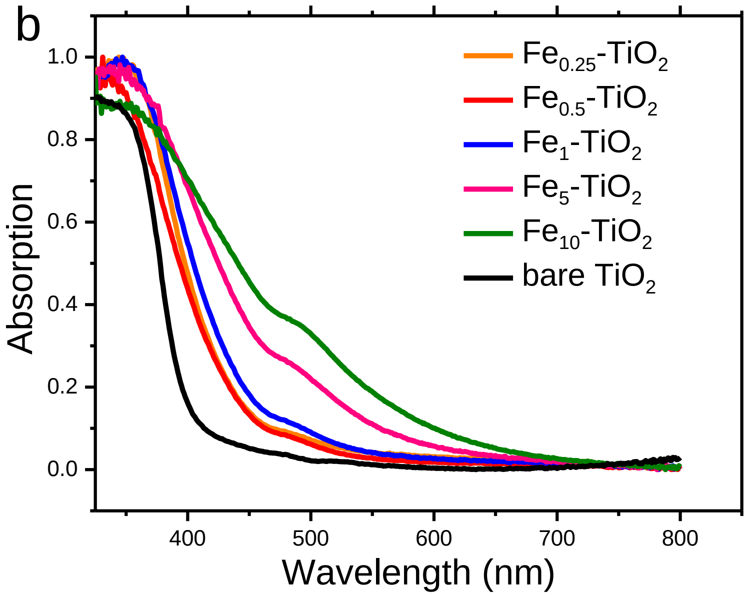
b
Absorption
Wavelength (nm)
1.0
0.8
0.6
0.4
0.2
0.0
400
500
600
700
800
$Fe_{0.25}$-TiO_2
$Fe_{0.5}$-TiO_2
Fe_1-TiO_2
Fe_5-TiO_2
Fe_{10}-TiO_2
bare TiO_2

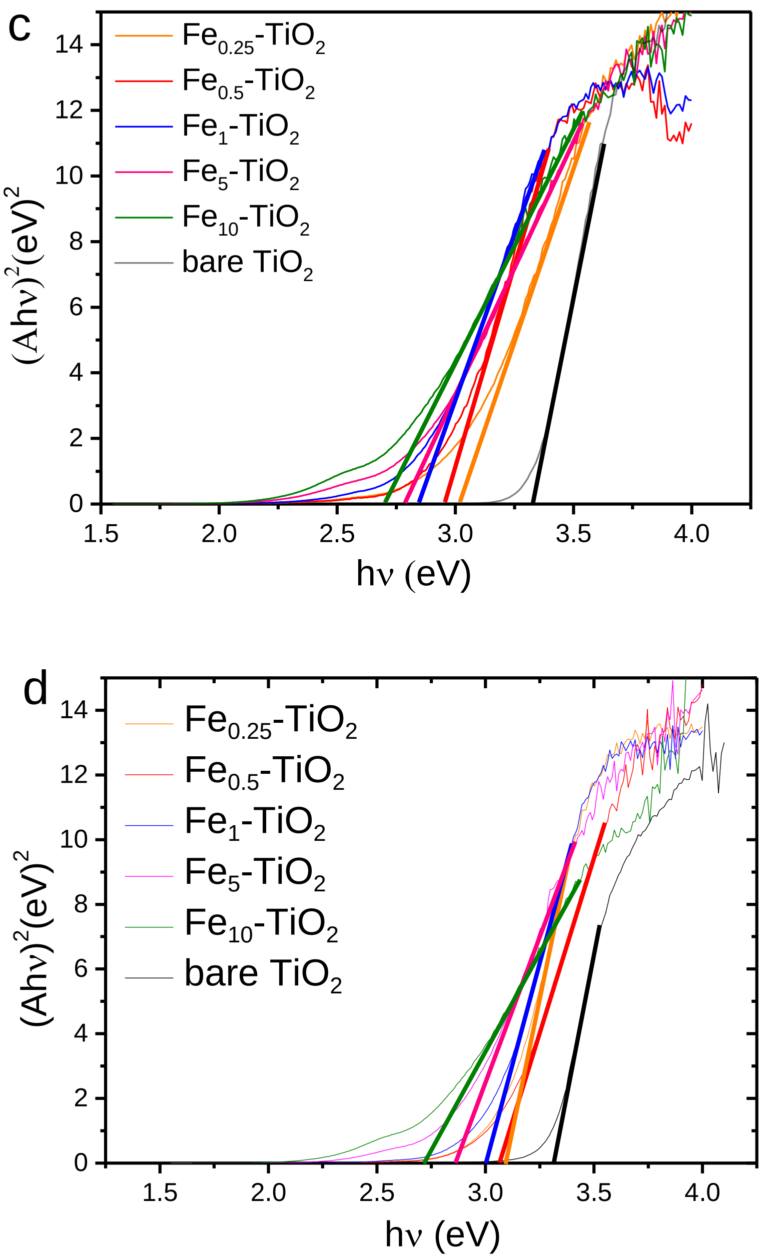

Figure 3.4. UV-vis diffuse reflectance spectra of a) untreated and b) acid treated, and Tauc plot of c) untreated and d) acid treated Fe-TiO_2 with different iron content (0.25, 0.5, 1, 5 and 10 Fe:Ti molar% ratio).

3.3.2 Photocatalytic Activity

As seen in the DRS spectra, the incorporation of Fe^{3+} ions into the crystal lattice of TiO_2 decreased the band gap and caused a red shift in the light absorption. The latter allows the photocatalyst to be activated under visible light illumination. Moreover, since the energy level of Fe^{3+}/Fe^{4+} is above the valence band energy and that of Fe^{3+}/Fe^{2+} is below the conduction band energy of TiO_2 [105, 140], Fe^{3+} reacts with both holes and electrons forming Fe^{4+} or Fe^{2+} traps. On the other hand, Fe^{2+} and Fe^{4+} are less stable than Fe^{3+} based upon the crystal field theory causing them to eventually revert back to the Fe^{3+} state upon their release of the electron and hole at the surface of the photocatalyst initiating the photocatalytic reactions [30, 59, 64, 66, 141]. The latter occurs after light absorption by Fe-TiO_2 to create the photo-generated electrons and holes concomitantly with the generation of hydroxyl and superoxide radicals as follows [92, 111, 127, 142]:

$$Fe^{3+} + h^+ \rightarrow Fe^{4+} \qquad \text{Equation 3.2}$$

$$Fe^{3+} + e^- \rightarrow Fe^{2+} \qquad \text{Equation 3.3}$$

$$Fe^{4+} + OH^- \rightarrow Fe^{3+} + OH^\bullet \qquad \text{Equation 3.4}$$

$$Fe^{2+} + O_2 \rightarrow Fe^{3+} + O_2^{-\bullet} \qquad \text{Equation 3.5}$$

500 mg.L^{-1} of the catalyst was used in all of the photocatalytic activity reactions. Figure 3.5 (a, b) shows the photocatalytic activity and rate constants of bare TiO_2 and untreated Fe-TiO_2 with different amounts of dopant measured under visible light illumination. Among the particles synthesized in natural pH, $Fe_{0.5}$-TiO_2 showed the highest photocatalytic activity. The increase in the doping content led to a decrease in the degradation efficiency; as it can be observed, the photocatalytic activity of bare TiO_2 is

higher than that of Fe_1-TiO_2, Fe_5-TiO_2 and Fe_{10}-TiO_2. Although Fe^{3+} can trap both electrons and holes up to an optimum amount of doping, a further increase makes it a recombination center, which reduces the photo-generated charge carriers' chance to reach the surface and initiate the photocatalytic reactions [143-145]. Also, the high concentration of Fe^{3+} leads to the iron oxide contamination layers on the surface of catalyst particles, which decreases the accessible active sites, where the photocatalytic reactions occur. In a study to evaluate the effect of the synthesis pH on the photocatalytic activity, $Fe_{0.5}$-TiO_2 synthesized in natural pH was compared to $Fe_{0.5}$-TiO_2 synthesized in acidic pH (~3). As it can be seen in Figure 3.5 5a and 5b, the degradation efficiency was increased from 18% to 24%. This increase is due to the smaller crystallite size and finer catalyst particles, which as showed using XRD patterns and Scherrer equation was resulted from the synthesis of particles in the acidic pH. The rate constants were obtained using Langmuir Hinshelwood model, which relates the reaction rate to the concentration of the organic pollutant as follows [146]:

$$r = -\frac{dC}{dt} = \frac{k_r K_{ad} C}{1+K_{ad}+C} \qquad \text{Equation 3.6}$$

where r is the reaction rate, C is the concentration of the pollutant, t is the reaction time, k_r is the intrinsic rate constant and K_{ad} is the adsorption equilibrium constant. When the concentration of the pollutant is very low, E quation 3.6 can be simplified to:

$$\ln\left(\frac{C}{C_0}\right) = -k_r k_{ad} t = k_{app} \qquad \text{Equation 3.7}$$

where k_{app} is the apparent first order rate constant.

$Fe_{0.5}$-TiO_2 synthesized in acidic pH showed the highest rate constant (k_{app}) (Figure 3.5b). As it can be observed from Figure 3.5c treating the Fe-TiO_2 particles in HCl solution increased their photocatalytic activity significantly (up to 5 times). Such an increase in the photocatalytic activity is attributed to removal of the iron oxide layers from the surface of the catalyst particles, resulting into a cleaner surface with more reactive sites for the redox reactions. The $Fe_{0.5}$-TiO_2 particles synthesized in acidic pH demonstrated the highest photocatalytic activity among the other samples and its photocatalytic activity increased from 24% up to 98% after the acid treatment process. It is noteworthy to mention that the specimens with the higher doping content showed a higher relative increase in their photocatalytic activity after the acid treatment; this is due to the higher amount of deposited iron oxide on their surface. Moreover, as can be seen from Figure 3.5d the rate constants have been increased significantly after the acid treatment of the particles. These results are consistent with HRTEM images, where it was observed that after acid treatment of the particles the amorphous layers on the catalyst surface were removed. Also, XPS data confirmed that the at.% of iron was decreased by treating the catalyst with HCl solution showing that the contamination observed on the surface was related to the formed iron oxide layers.

It was necessary to study the effect of the acid treatment on bare TiO_2 to make sure the increase in the photocatalytic activity was not due to a change in morphology of the particle's surface. The bare TiO_2 catalyst particles were treated with HCl solution and their photocatalytic activity was measured under UV light illumination. Figure 3.5(e, f) illustrate the degradation efficiency and the rate constant for bare TiO_2 before and after the acid treatment. The degradation efficiency of bare TiO_2 did not change upon acid treatment, but the obtained k_{app} value for the untreated TiO_2 showed a higher rate constant compared to that of the acid treated one. This result shows that the increase in the Fe-TiO_2 photocatalytic activity, following acid treatment process, was only due to the surface iron oxide layers' removal and not related to the morphology and/or surface modifications caused by etching with the HCl solution. Also, the degradation efficiency of MO under UV and visible light without any catalyst was measured as the control experiments (Figure 3.5c). MO was degraded 20% under UV light after 60 min of reaction time and there was no degradation under visible light illumination. Table 3.4 and Table 3.5 summarize the obtained k_{app} before and after the acid treatment. The linear regression coefficient (R^2) shows the linearity of the plotted ln (C_0/C) vs. time. The high values of the R^2 shows that the fitted plots are linear and the reaction kinetics follows the apparent first order equation [147, 148].

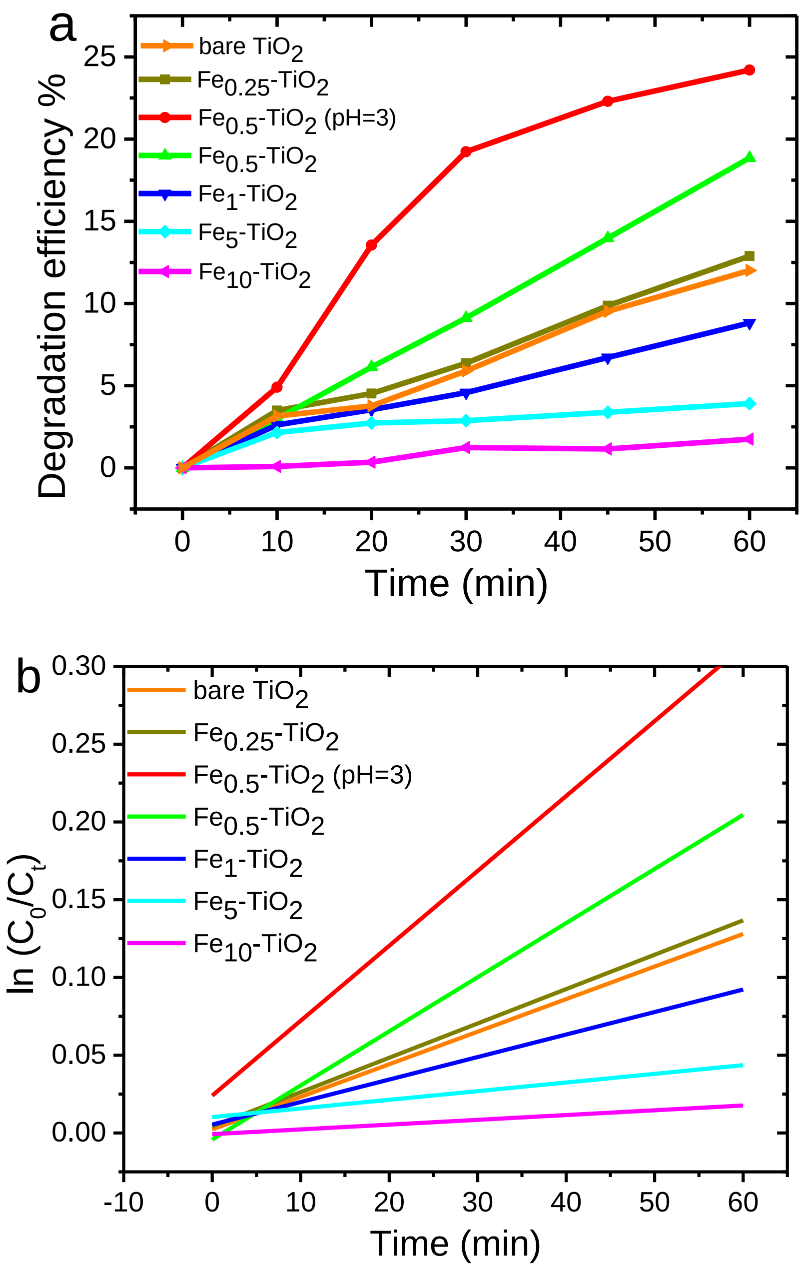
a
Degradation efficiency %
Time (min)
0
5
10
15
20
25
0
10
20
30
40
50
60
bare TiO$_2$
Fe$_{0.25}$-TiO$_2$
Fe$_{0.5}$-TiO$_2$ (pH=3)
Fe$_{0.5}$-TiO$_2$
Fe$_1$-TiO$_2$
Fe$_5$-TiO$_2$
Fe$_{10}$-TiO$_2$
b
ln (C$_0$/C$_t$)
Time (min)
0.00
0.05
0.10
0.15
0.20
0.25
0.30
-10
0
10
20
30
40
50
60
bare TiO$_2$
Fe$_{0.25}$-TiO$_2$
Fe$_{0.5}$-TiO$_2$ (pH=3)
Fe$_{0.5}$-TiO$_2$
Fe$_1$-TiO$_2$
Fe$_5$-TiO$_2$
Fe$_{10}$-TiO$_2$

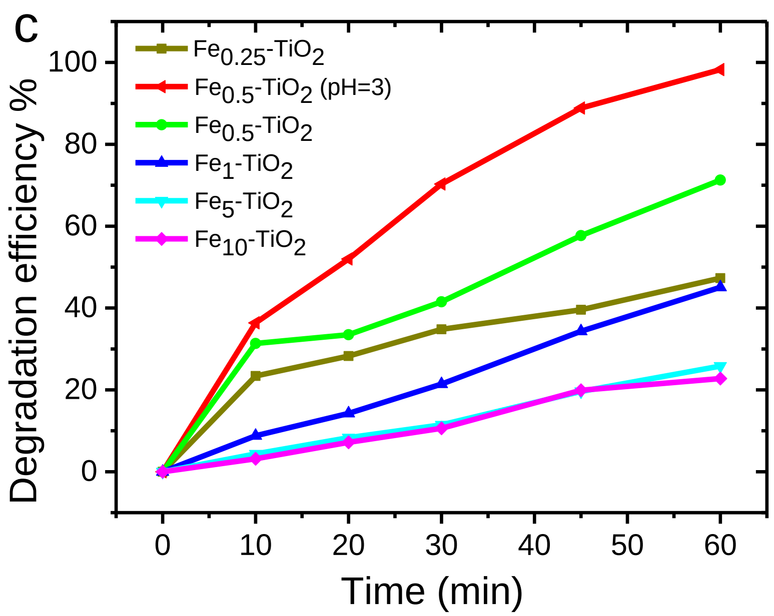
c
Fe0.25-TiO2
Fe0.5-TiO2 (pH=3)
Fe0.5-TiO2
Fe1-TiO2
Fe5-TiO2
Fe10-TiO2
Degradation efficiency %
100
80
60
40
20
0
0
10
20
30
40
50
60
Time (min)

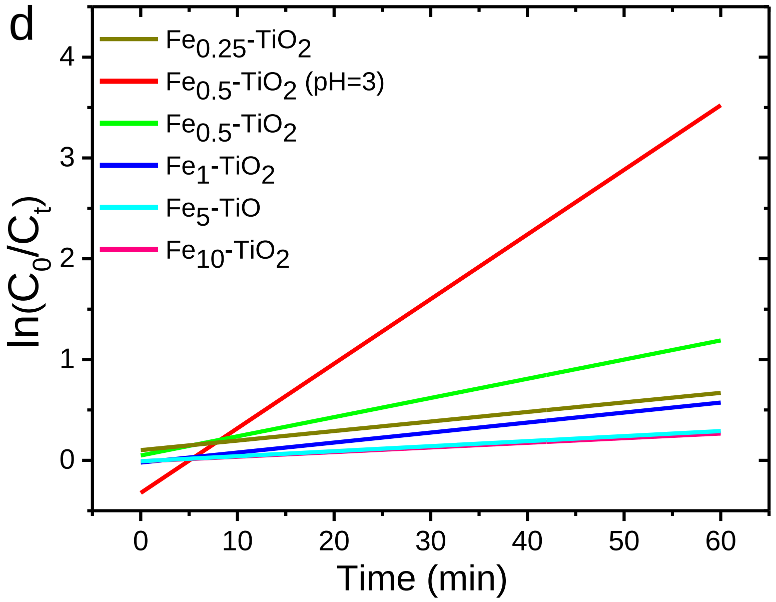
d
Fe0.25-TiO2
Fe0.5-TiO2 (pH=3)
Fe0.5-TiO2
Fe1-TiO2
Fe5-TiO
Fe10-TiO2
ln(C0/Ct)
4
3
2
1
0
0
10
20
30
40
50
60
Time (min)

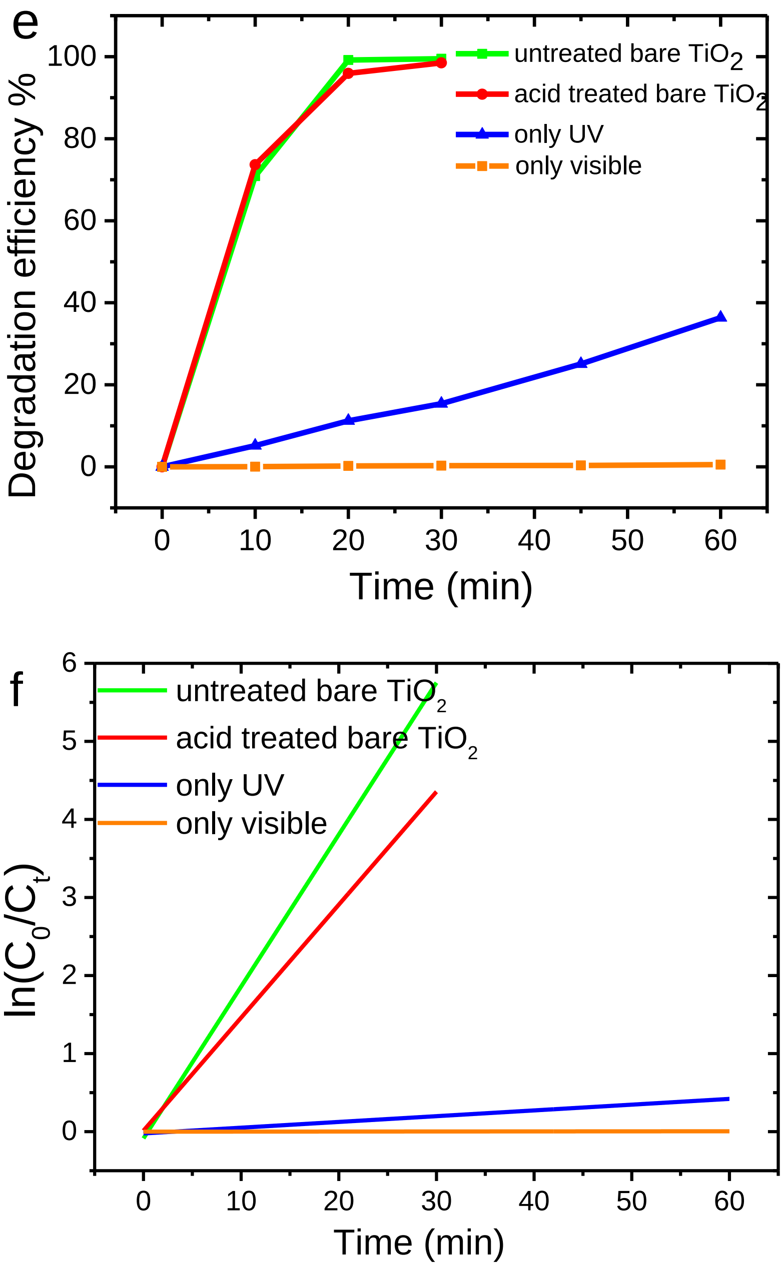

Figure 3.5. a) the degradation efficiency and b) rate constants of untreated bare TiO_2 and Fe-TiO_2; c) the degradation efficiency and d) rate constants of acid treated Fe-TiO_2 with different doping content under visible light illumination; and e) the degradation efficiency and f) rate constants of untreated and acid treated bare TiO_2 under UV light illumination. The degradation efficiency was measured using 20 mg.L^{-1} of MO solution within 60 min of reaction time. The comparison between the degradation efficiency of untreated and acid

treated catalysts shows that the acid treatment process increased the photocatalytic activity of Fe-TiO_2 significantly, whereas it did not affect the bare TiO_2.

Table 3.4. k_{app} of Fe-TiO_2 (under visible light irradiation) with different Fe^{3+} content before and after the acid treatment.

catalyst	k_{app} (min^{-1}) of untreated catalysts	R^2	k_{app} (min^{-1}) of acid treated catalysts	R^2
$Fe_{0.25}$-TiO_2	0.00221	0.98	0.00947	0.90
$Fe_{0.5}$-TiO_2 (pH=3)	0.00462	0.91	0.06409	0.92
$Fe_{0.5}$-TiO_2	0.00348	0.99	0.01902	0.95
Fe_1-TiO_2	0.00145	0.98	0.00992	0.98
Fe_5-TiO_2	0.00056	0.88	0.00499	0.98
Fe_{10}-TiO_2	0.00031	0.90	0.00460	0.97

Table 3.5. k_{app} of bare TiO_2 before and after the acid treatment (under UV light irradiation) and only UV and only visible light irradiation.

sample		k_{app} (min^{-1})	R^2
bare TiO_2 under UV light irradiation	Untreated	0.19459	0.98
	acid treated	0.14471	0.97
only UV light		0.00738	0.97
only visible light		0.00088	0.93

3.4 Conclusions

In summary, Fe-TiO_2 nanoparticles were synthesized by a simple sole-gel method. The effects of Fe^{3+} doping content on the band gap and size of the nanoparticles was studied. It was observed that the increase in the doping content decreased the band gap energy and particle size from 3.3 eV and 13 nm for bare TiO_2 to 2.9 eV and 5 nm for Fe_{10}-TiO_2, respectively. An amorphous layer on the surface of the catalyst particles was identified by HRTEM, and characterized using XPS measurements shown to be composed of iron oxide on the surface of the Fe-TiO_2 nanoparticles. The contamination layer was removed using HCl solution as confirmed by the HRTEM images and the XPS. Cleaning the surface of nanoparticles increased the photocatalytic activity from 24% to 98%.

3.5 Supporting information

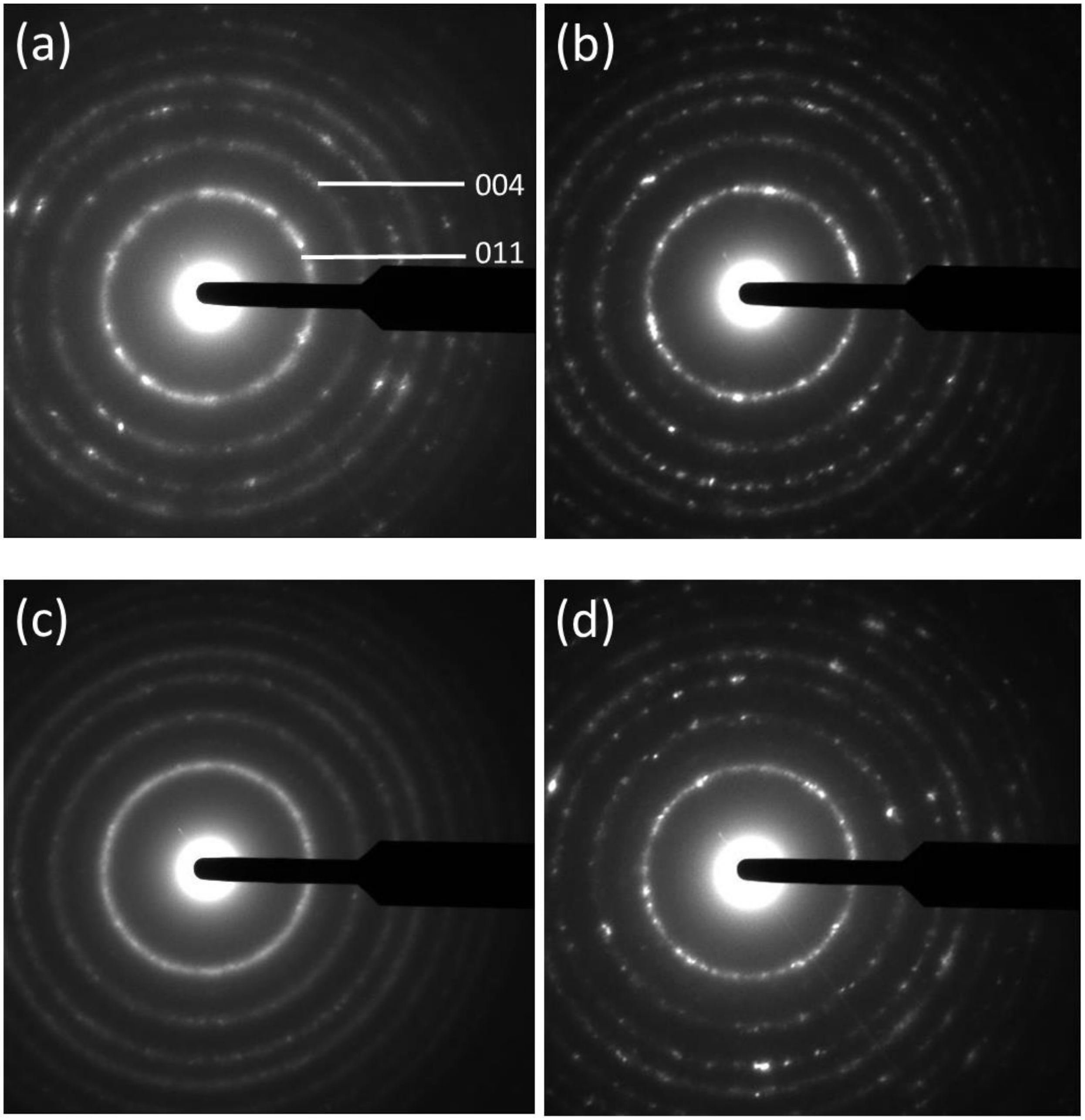

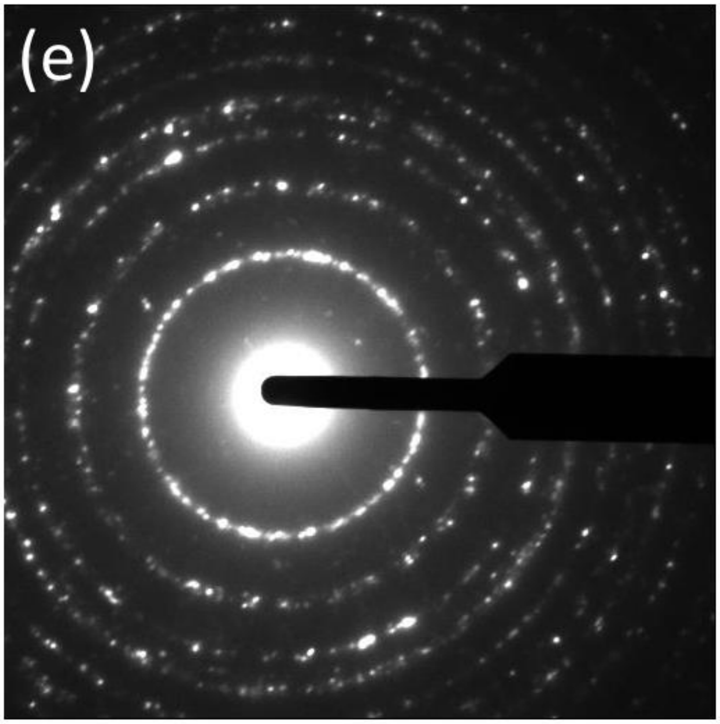

Figure 3.6. SAED of a) untreated and b) acid treated bare TiO_2; and untreated c) $Fe_{0.5}$-TiO_2 d) Fe_1-TiO_2 and e) Fe_5-TiO_2.

Figure 3.7 and Figure 3.8 illustrate the XPS survey scans of bare TiO_2, Fe_5-TiO_2, Fe_1-TiO_2 and high resolution scans of Fe 2p, O 1s and Ti 2p of Fe_{10}-TiO_2.

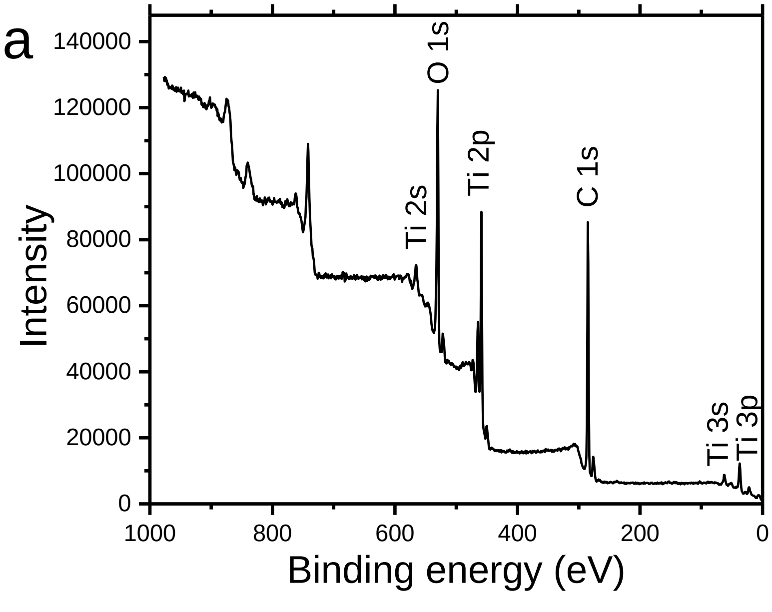

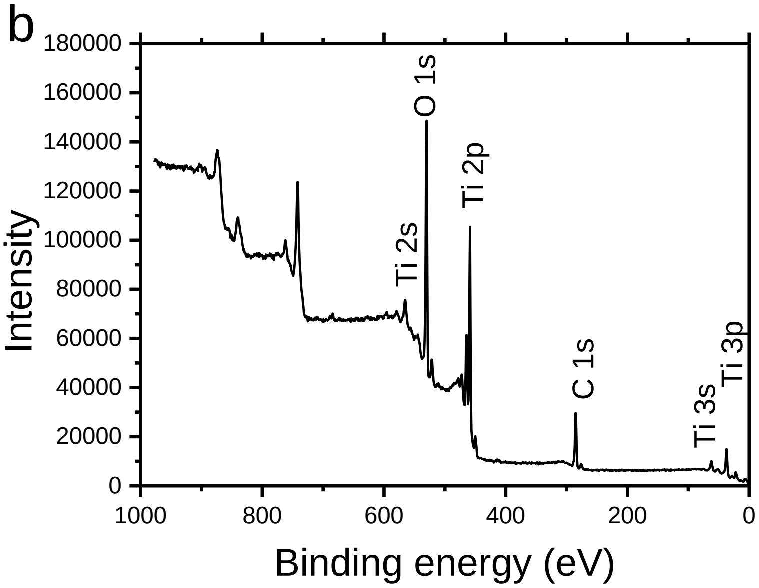
b
Intensity
180000
160000
140000
120000
100000
80000
60000
40000
20000
0
1000
800
600
400
200
0
Binding energy (eV)
O 1s
Ti 2p
Ti 2s
C 1s
Ti 3s
Ti 3p

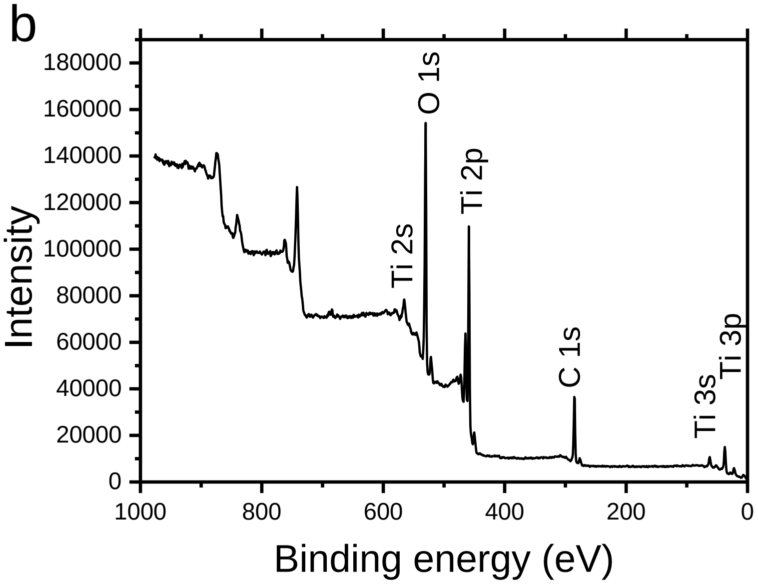
b
Intensity
180000
160000
140000
120000
100000
80000
60000
40000
20000
0
1000
800
600
400
200
0
Binding energy (eV)
O 1s
Ti 2p
Ti 2s
C 1s
Ti 3s
Ti 3p

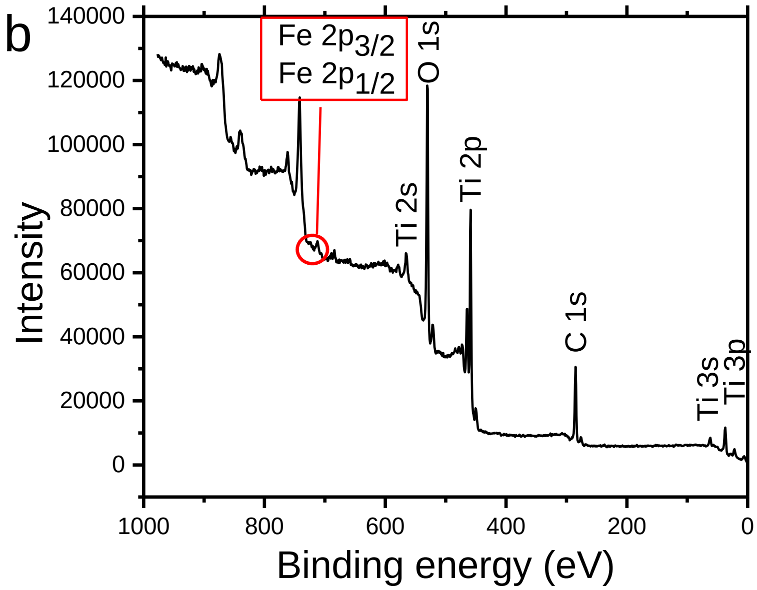
b
Fe 2p3/2
Fe 2p1/2
O 1s
Ti 2p
Ti 2s
C 1s
Ti 3s
Ti 3p
Intensity
140000
120000
100000
80000
60000
40000
20000
0
1000
800
600
400
200
0
Binding energy (eV)

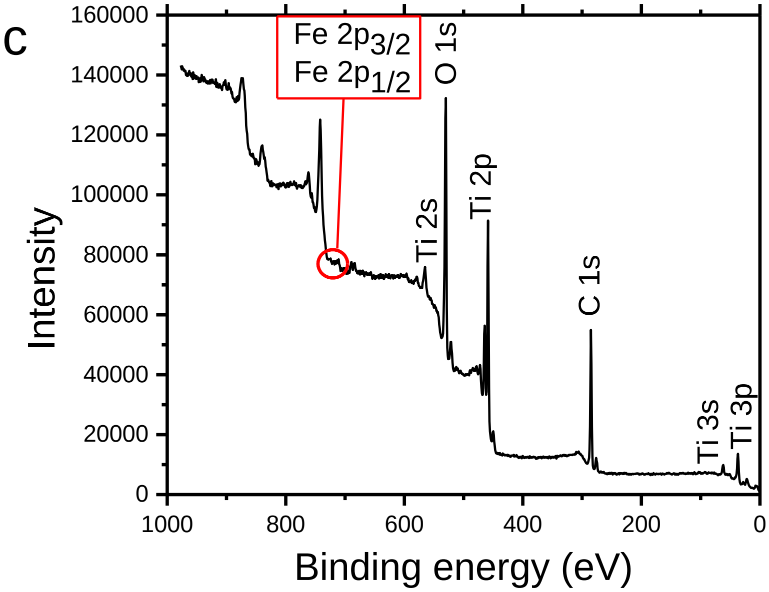
c
Fe 2p3/2
Fe 2p1/2
O 1s
Ti 2p
Ti 2s
C 1s
Ti 3s
Ti 3p
Intensity
160000
140000
120000
100000
80000
60000
40000
20000
0
1000
800
600
400
200
0
Binding energy (eV)

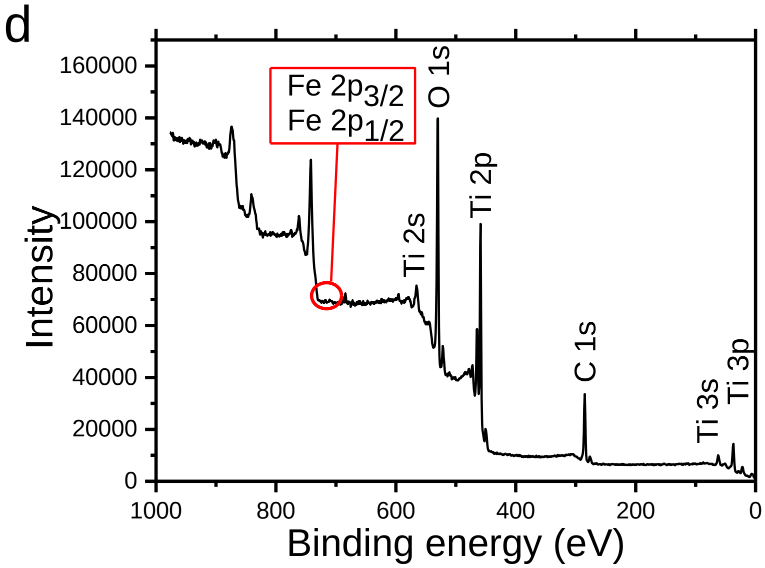

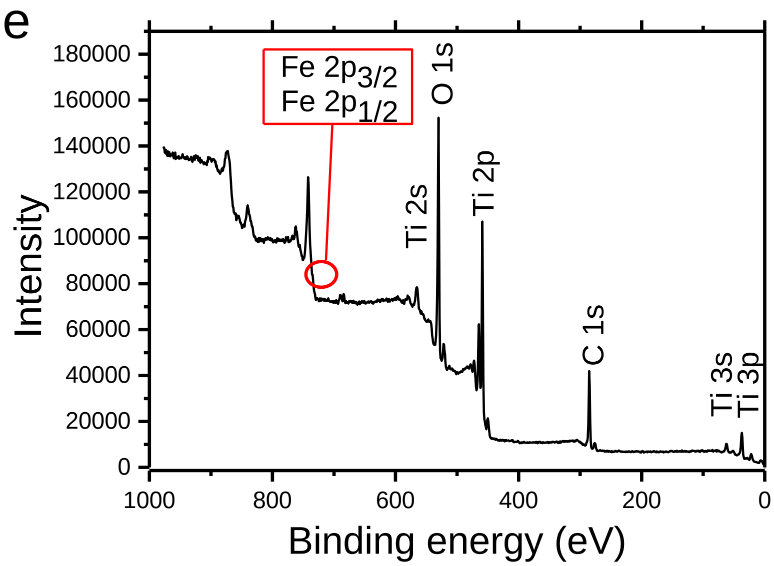

Figure 3.7. XPS survey scan of a) bare TiO_2; b) untreated and c) acid treated $Fe0._5$-TiO_2; d) untreated and e) acid treated Fe_5-TiO_2; f) untreated and g) acid treated Fe_1-doped TiO_2.

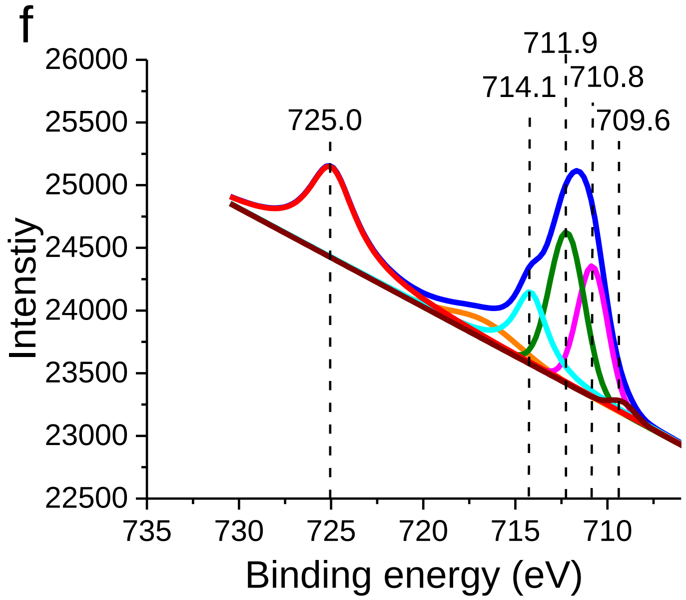
f
711.9
714.1
710.8
725.0
709.6
26000
25500
25000
24500
24000
23500
23000
22500
Intenstiy
735
730
725
720
715
710
Binding energy (eV)

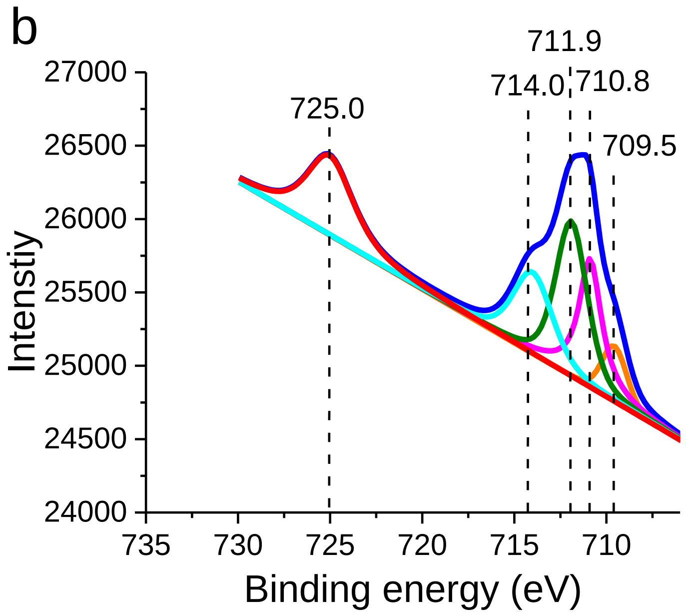
b
711.9
714.0
710.8
725.0
709.5
27000
26500
26000
25500
25000
24500
24000
Intenstiy
735
730
725
720
715
710
Binding energy (eV)

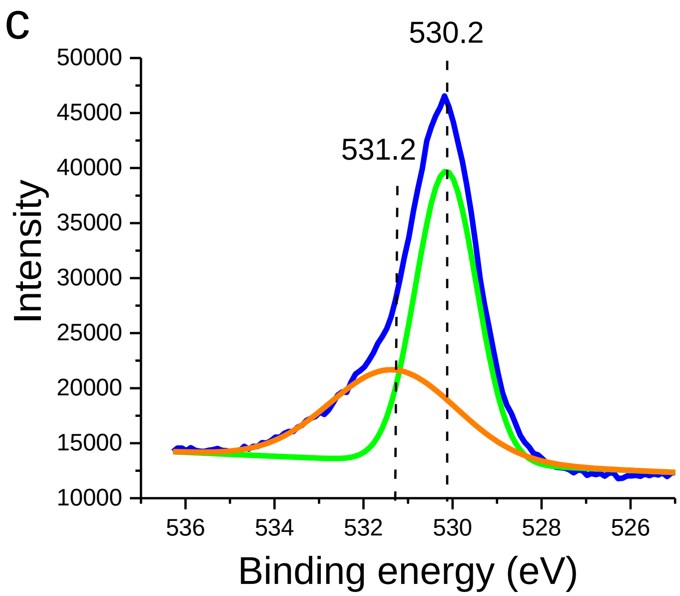
c
530.2
531.2
Intensity
50000
45000
40000
35000
30000
25000
20000
15000
10000
536
534
532
530
528
526
Binding energy (eV)

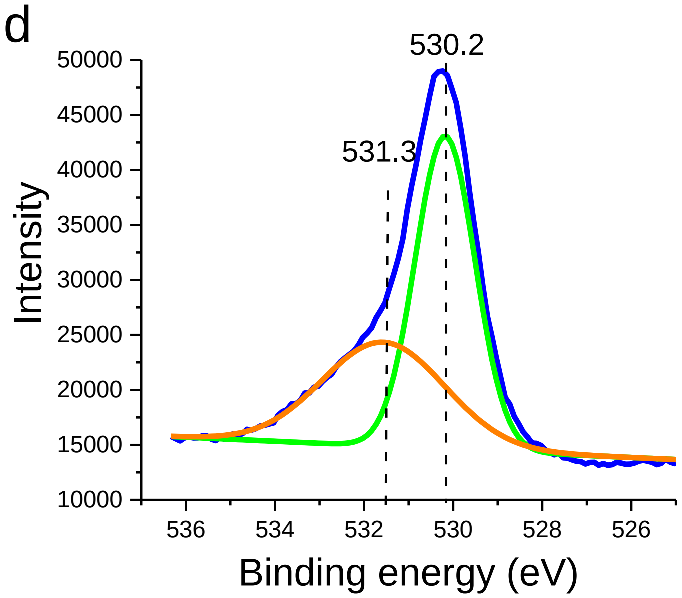
d
530.2
531.3
Intensity
50000
45000
40000
35000
30000
25000
20000
15000
10000
536
534
532
530
528
526
Binding energy (eV)

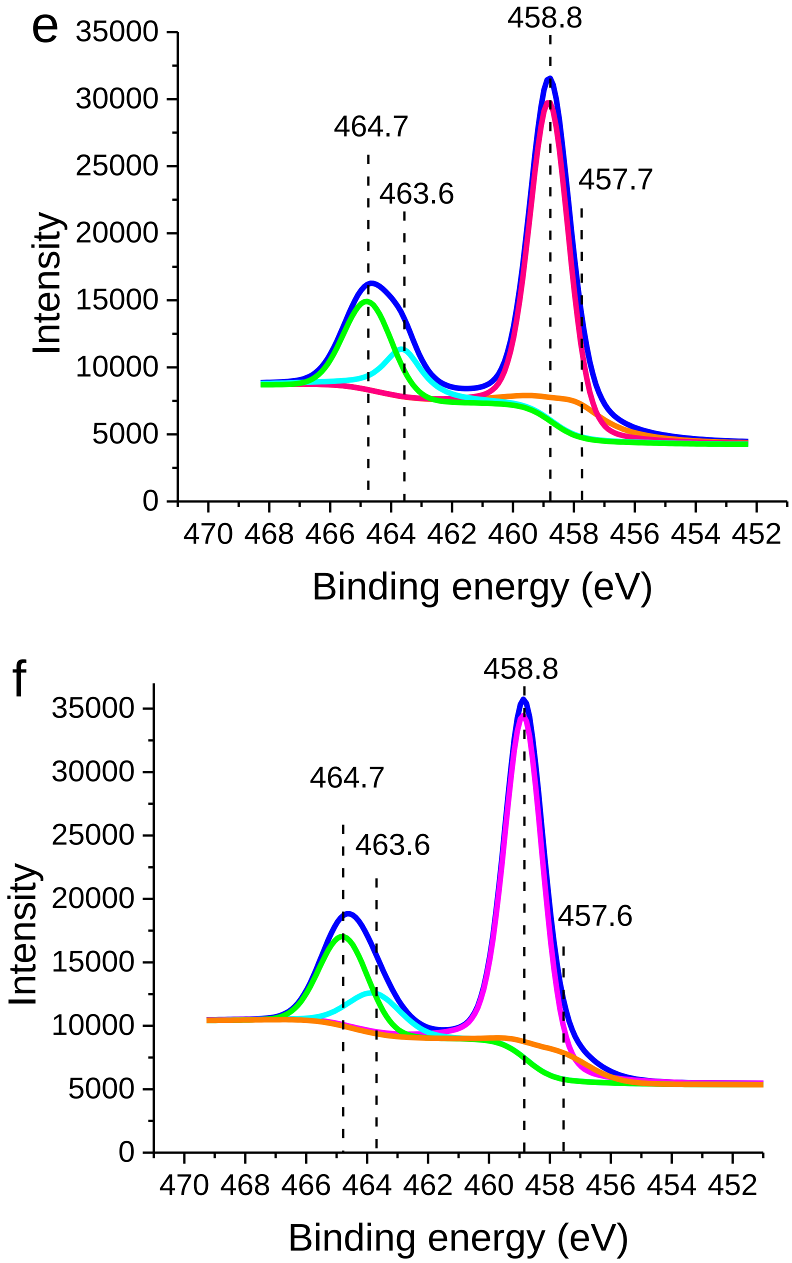

Figure 3.8. High resolution XPS scan of a) untreated and b) acid treated Fe 2p of Fe_{10}-TiO_2; high resolution XPS scan of c) untreated and d) acid treated O 1s of Fe_{10}-TiO_2; high resolution XPS scan of e) untreated and f) acid treated Ti 2p of Fe_{10}- TiO_2.

Acknowledgment

This study was financially supported by the Korea Institute of Energy Technology Evaluation and Planning (KETEP) and the Ministry of Trade, Industry and Energy (MOTIE) of the Republic of Korea and Natural Sciences and Engineering Research Council of Canada (NSERC) and Canada Foundation of Innovation (CFI).

Graphical Abstract

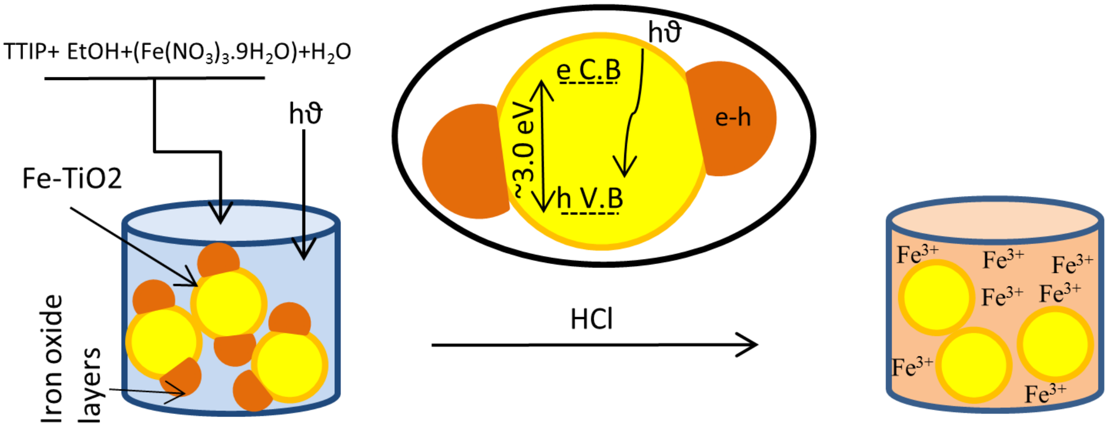

Figure 3.9. The graphical abstract of the paper entitled “Significant improvement in visible light photocatalytic activity of Fe doped TiO_2 using an acid treatment process”.

Chapter 4 Photocatalytic degradation of phenol under visible light irradiation using a high performance, acid treated Fe doped TiO_2

This paper is submitted to the journal of Water Research.

Vahid Moradi, Martin B. G. Jun and Rodney A. Herring

Abstract

In the present work, degradation of phenol solution was used to obtain the optimum synthesis condition of Fe doped TiO_2 nanoparticles and the effect of the parameters on their degradation efficiency. The optimum condition for sol-gel to prepare Fe-TiO_2 nanoparticles was obtained using 0.5 Fe:Ti molar% ratio synthesized in an acidic pH of 3. The nanoparticles were characterized by means of HRTEM, EDX, XPS and DRS. It was observed that the photocatalytic activity suffered from an iron oxide contaminating layer deposited on the surface of the nanoparticles. This contamination was removed using a concentrated HCl acid treatment process. The photocatalytic activity using 500 $mg.L^{-1}$ of $Fe_{0.5}$-TiO_2 in a 10 $mg.L^{-1}$ of phenol solution increased 27% upon removing the contamination layer (from 33%, before the acid treatment, to 42%, after the acid treatment). In addition, the effect of different influential parameters such as catalyst load, pollutant concentration, and reaction time on the degradation efficiency were evaluated. By removing the iron oxide contaminating layer and the control of pH in mild acidic and basic pHs, a 73% increase in the photocatalytic activity within 90 min of reaction time was obtained.

KEYWORDS: Phenol degradation, visible light, photocatalyst, kinetics, iron doping

4.1 Introduction

Phenol is an aromatic, highly toxic compound with a slow degradability in the environment [149]; it has been reported that 1-10 nM of phenol is very toxic for both humans and plants [150]. There is an increasing trend to produce phenol due to its enormous use in industries such as refineries, coal processing, petrochemical, glue, resin, paints, rubber and textile industries [151, 152].

Titanium dioxide has attracted enormous attention in the treatment of water [153-156] and air [157-159] due to its high efficiency in photocatalytic reactions. Meanwhile, TiO_2 is chemically inert, inexpensive, nontoxic, corrosion resistant and environmentally friendly [20, 160-162]. An absorbed photon with a higher energy than the band gap energy causes an electron to be excited to the conduction band, leaving a hole in the valence band [20, 163, 164]. Unfortunately, the high band gap energy of TiO_2 (3.2 eV) limits its application only to UV light irradiation. Since only 8% of solar light contains UV light, TiO_2 is inefficient under solar light irradiation [165-167]. Therefore, to use the photocatalytic capabilities of TiO_2 under solar light irradiation, it is necessary to change the electronic structure of its crystal lattice to decrease its band gap energy. Incorporation of dopants in the structure of TiO_2 is one of the solutions to this problem. It has been reported that transition metal dopants cause a red shift from UV light to visible light achieved by the formation of intermediate energy levels [21, 164]. The decrease in the band gap energy is the result of excitation of the electrons from 3d or 4d orbitals of the dopant to 3d orbitals of Ti [168]. According to previous research the ionic radii of Fe^{3+} is very close to that of Ti^{4+}, hence Fe^{3+} easily substitutes Ti^{4+} in the crystal lattice. The absorption edge sharply increases to longer wavelengths based upon the increase in the iron content, consistent with the change in the color of particles from white to yellow and light brown [30]. Asiltürk et al. reported that with the increase in the iron content in the crystal lattice of TiO_2, the particle size decreased, providing a larger surface area in benefit of photocatalytic activity caused by the inhibiting effect of Fe^{3+} on the crystallization, which leads to the smaller TiO_2 crystallite size [59]. Based on photoluminescence measurements, the presence of Fe^{3+} decreases the electron/hole recombination rate; however, too much iron has the opposite effect, i.e., it increases the recombination since iron will also act as a recombination center. Thus, an optimum concentration of Fe^{3+} is required [169]. As well, Fe^{3+} traps both electrons and holes by forming Fe^{2+} and Fe^{4+}, which results in the increase in the life time of charge carriers. According to the crystal field theory the most stable state is Fe^{3+} (d^5); so, Fe^{2+} and Fe^{4+} return to the more stable state of Fe^{3+} by releasing the trapped electron and hole preferably at the surface of the nanocrystal. The energy level of Fe^{2+}/Fe^{3+} is very close to that of Ti^{3+}/Ti^{4+}, subsequently, the trapped electron in Fe^{2+} can migrate to the neighbour Ti^{4+} and eventually reach to the surface [92]. Previous studies have shown that during the doping process, the iron does not enter the crystal lattice completely and it can precipitate on the surface of the nanoparticles by forming iron oxides [106]. The layer of iron oxide on the surface of the Fe-TiO_2 has two effects: 1) it contaminates the surface of the TiO_2 particles and decreases the surface area to volume ratio, and 2) it acts as a recombination center for electrons and holes, which decreases the lifetime of the charge carriers [107-109]. In our previous study [33], we showed that cleaning this contamination layer using a concentrated HCl acid treatment increases the photocatalytic activity of Fe-TiO_2 significantly using methyl orange as the pollutant representative. However, it was crucial to investigate the degradation efficiency using a more stable molecule. Therefore, in the present work the photocatalytic activity of Fe-TiO_2 before and after the acid treatment was studied using phenol molecule. Moreover, the effect of different influential parameters such as the amount of doping content, concentration of catalyst, reaction time, initial concentration of the pollutant and pH were investigated on the degradation efficiency and kinetics of reaction.

4.2 Materials and methods

4.2.1 Reagents and chemicals

All the chemicals were used as purchased without further purification. Titanium isopropoxide (TTIP) (>97%) was used as the precursor of the TiO_2 nanoparticles and iron (III) nitrate nonahydrate ($Fe(NO_3)_3.9H_2O$) was used as the Fe^{3+} dopant both purchased from Sigma Aldrich. Hydrochloric acid (HCl) and sodium hydroxide (NaOH) were used to adjust the pH solution and were obtained from Sigma Aldrich. Deionized water (with the purity of >18.2 MΩ) was used to synthesize the catalyst particles.

4.2.2 Material characterization

X-ray diffraction (XRD) patterns were collected using PANalytical Empyrean X-ray diffractometer with a copper X-ray lamp, Kα (*A*°) = 1.54 at room temperature with the 2θ angles scanned from 10 to 90 degrees. Elemental analysis and surface chemical composition were studied using Omicron & Leybold MAX200 X-ray Photoelectron Spectrometer (XPS). Elemental analysis of energy dispersive X-ray (EDX), and SEM images were obtained using Hitachi S-4800 instrument. The acceleration voltage and working distance for SEM images were 1 kV and 8 cm and those for EDX mapping were 15 kV and 15 cm, respectively. A Hitachi HF-3300v was used to obtain HRTEM images.

UV-vis absorbance spectra of the catalyst powders were obtained using a Lambda 1050 UV/Vis-NIR Spectrometer. A Cary 100 UV-vis Spectrometer was used to measure the concentration of phenol for photocatalytic activity measurements.

4.2.3 Catalyst preparation

TiO_2 and Fe-doped TiO_2 were prepared using a simple sol-gel method. Different amounts of iron (0.5, 1, 5 and 10:1, Fe:Ti %molar ratio) was used as the dopant and a constant H_2O:Ti (4:1) molar ratio was used to prepare the catalysts. The desired amount of iron was dissolved in deionized water and the mixture was added to 30 mL of anhydrous ethyl alcohol. The pH was adjusted to the desired one in this step using HNO_3 solution. It should be mentioned that $Fe_{0.5}$-TiO_2 sample was synthesized in an acidic pH (~3) to study the effect of synthesis pH on the photocatalytic activity. Then, the TTIP was added dropwise to the solution. The mixture was stirred for 2 hrs and consecutively dried in the oven for 2 hrs at 80 °C. The dried powder was ground using a mortar to obtain finer particles and then were washed 3 times using deionized water to remove the remained ethyl alcohol residual. They were then calcined in the oven at 400 °C for 3 hrs. Since HCl has been reported to be a suitable solvent for iron oxide compounds [110, 170], it was used to dissolve and remove the iron oxide layers. To acid-treat the catalyst particles, they were stirred for 3 hrs in concentrated HCl solution (pH~2) and then washed 3 times with deionized water to remove the possible chlorine residual.

4.2.4 Photocatalytic reactions

The photocatalytic reactions were performed using phenol as the pollutant. All of the reactions were carried out in a 300 mL Pyrex cylindrical reactor containing 200 mL of solution. The desired amount of phenol was added to distilled water and then the pH of the solution was adjusted using HCl or NaOH. The desired amount of catalyst was loaded to the mixture and it was stirred for 30 min in the dark to reach the adsorption equilibrium before the lamp was turned on. A 300 W xenon lamp with a λ>400 nm cut off filter was used as the visible light source. The distance of the lamp in all experiments was kept fixed at 20 cm above the solution. Degradation efficiency (DE) was calculated using the following equation:

$$X\% = \frac{C_0 - C_C}{C_0} \times 100 \qquad \text{Equation 4.1}$$

where, $X\%$ is the DE, C_0 and C_c are the initial and final concentrations of phenol, respectively.

4.3 Results and Discussions

4.3.1 Material characterization

Figure 4.1 shows the XRD patterns of the pristine TiO_2 and Fe-TiO_2 particles with different amounts of the doping content. The peak analysis showed a peak at 2θ value of 25.3, which is in accordance with the main peak of anatase, representing the (101) crystal plane [171]. Also, the Bragg diffraction peaks were observed at 38.01, 48.1, 54.03, 55.07, 62.05, 68.8, 70.2 and 75.1 corresponding to (004), (200), (105), (211), (204), (116), (220) and (215) crystal planes of anatase, respectively [112, 172]. Rutile phase with the main peak at 27.45° corresponding to (110) was not found in any of the particles showing that for the calcination temperature of 400 °C anatase is the only formed phase. The average particle size was obtained using the Scherrer equation [115, 173, 174]:

$$D = \frac{k\lambda}{\beta \cos\theta}$$ Equation 4.2

where D is the crystallite size, k is a constant (0.9 in this case), λ is the X-ray irradiation wavelength, β is the FWHM (full width at half maximum) and θ is the Bragg angle. It was found out that the average particle size for the pristine TiO_2 was about 13.0 nm. With an increase in the iron content, the size decreased and reached a minimum size of 5.9 nm for the Fe_{10}-TiO_2. Moreover, the crystallinity of the particles decreased as the doping content increased resulting to a significant decrease in the intensity of the anatase peaks. This suggests that the incorporation of Fe^{3+} ions in the crystal lattice effectively restrains the growth of the TiO_2. As the ionic radius of Fe^{3+} (0.645 $\mathring{A}$) and Ti^{4+} (0.604 $\mathring{A}$) are very similar [64], it is suggested that the Fe^{3+} ions substitute Ti^{4+} by the diffuse channels along the c-axis in the crystal lattice [175].

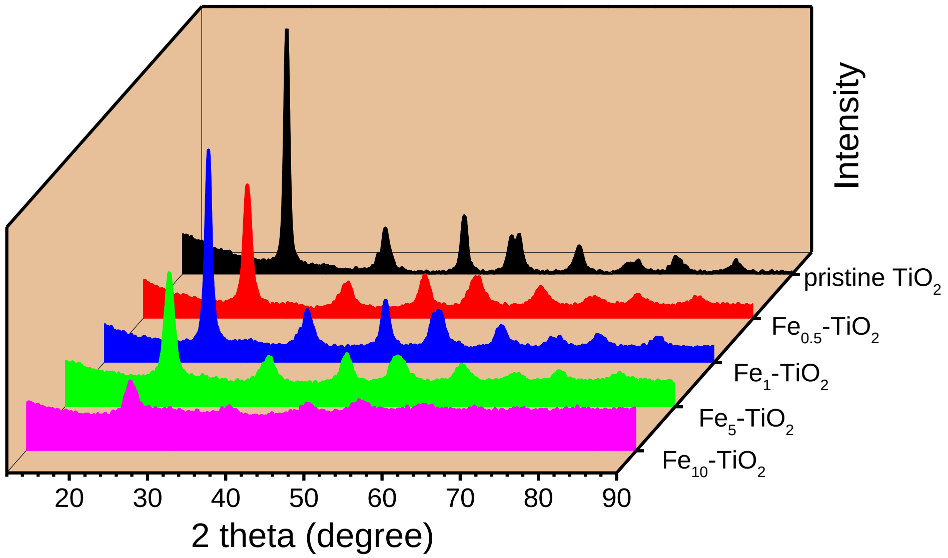

Figure 4.1. XRD pattern of the pristine and Fe-TiO_2 with different Fe^{3+} content calcined at 400 °C for 3 hours.

The HRTEM images (Figure 4.2) showed an unknown amorphous phase on the particles surface. This amorphous layer contaminates the surface of the nanoparticles decreasing the surface to volume ratio, which is a crucial factor in photocatalytic reactions, and promoting electron/hole recombination at the interface and preventing the charges from reacting with the adsorbed water and oxygen molecules to produce radicals. It was assumed that the contaminating layer is composed of iron oxide deposited on the surface. Therefore, the particles were stirred in concentrated HCl solution (pH~2) as a suitable solvent for hematite and magnetite to remove the contaminating layer. Figure 4.2 shows the Fe_{10}-TiO_2 nanoparticles (a) before and (b) after the acid treatment. The amorphous layer in the untreated particles (shown in the red dashed outlines) cannot be seen in the acid-treated particles.

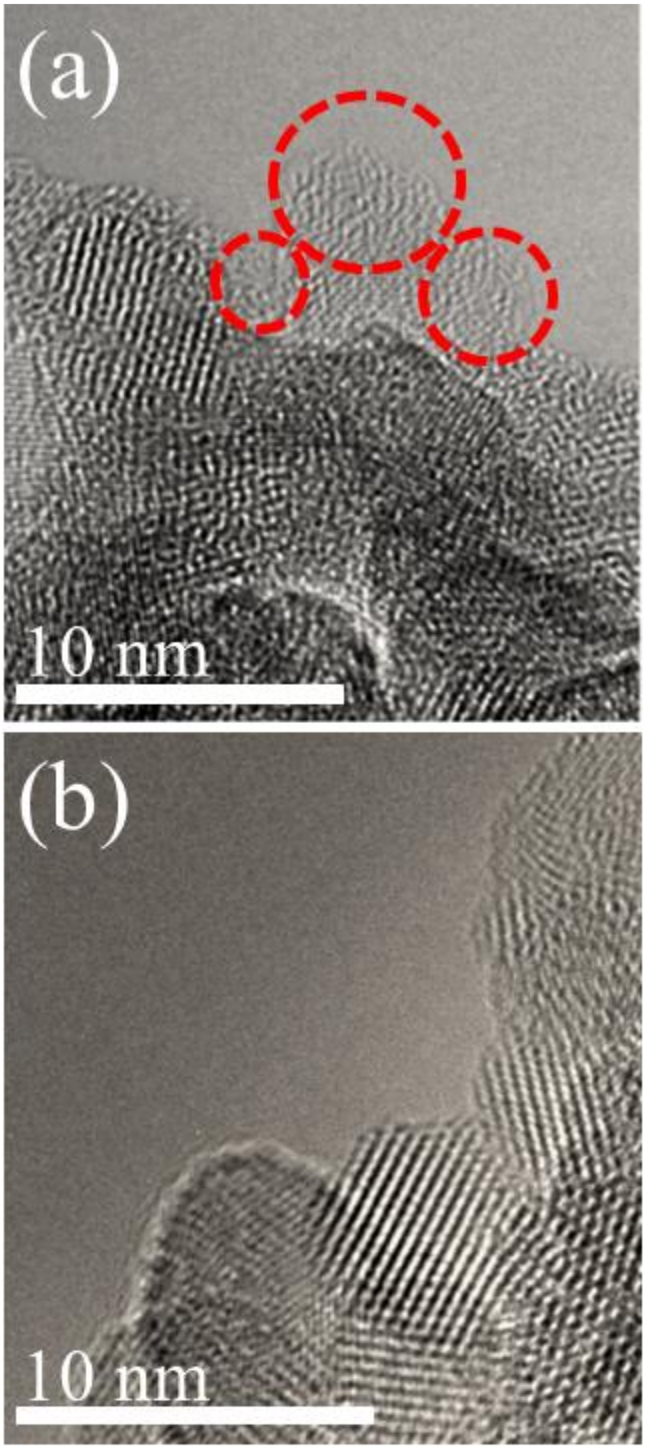

Figure 4.2. HRTEM images of a) untreated and b) acid treated Fe_{10}-TiO_2 nanoparticles.

The optical properties of pristine TiO_2 and Fe-TiO_2 have been described in detail in our previous study [33]. The effect of incorporation of Fe^{3+} and the acid treatment on the light absorption of Fe-TiO_2 is described in Figure 4.3 and Figure 4.11. The pristine TiO_2 with the band gap energy of ~3.3 eV did not show any visible light absorption. As the dopant was added to the crystal lattice of TiO_2, a red shift towards longer wavelength was observed and the band gap was decreased based on the increase in the doping content to 2.7 eV for Fe_{10}-TiO_2. Such decrease in the band gap energy is attributed to the interaction of the intermediate energy levels of Fe^{3+} with the 3d orbital of Ti in the conduction band [60, 111]. The absorption band observed around 500 nm is due to the d-d transitions of $^2T_{2g} \rightarrow {}^2A_{2g}$, $^2T_{1g}$ [135]. Moreover, the band gap of the Fe-TiO_2 nanoparticles after the acid treatment showed ~ 0.1 eV shift towards shorter wavelengths, which might be due to the removal of surface iron oxide.

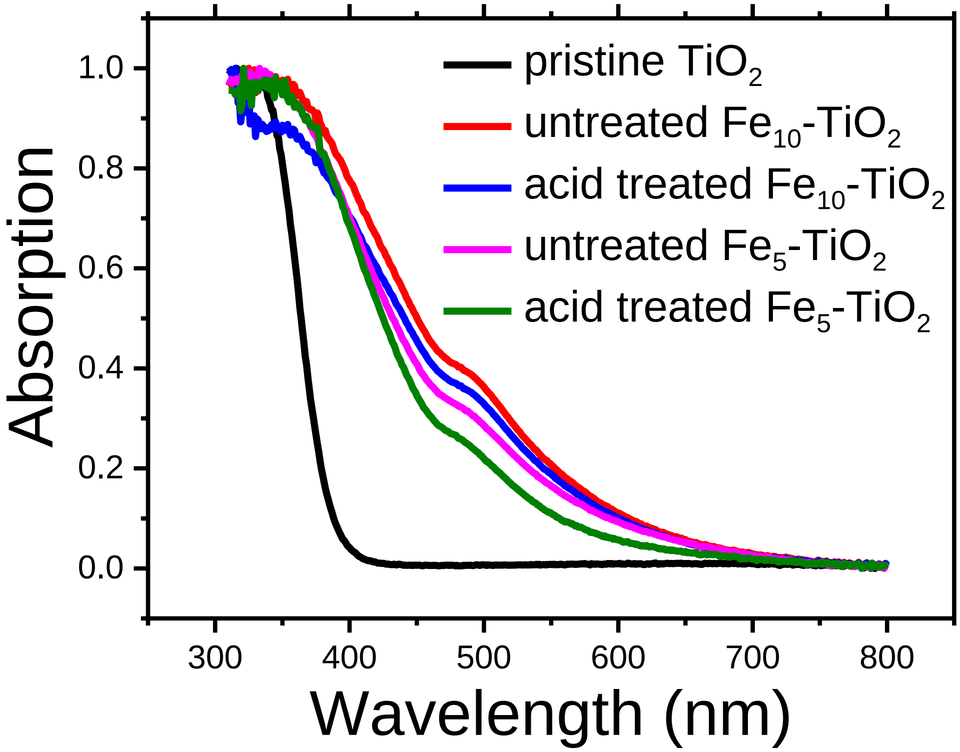

Figure 4.3. UV-vis absorption spectra of the pristine TiO_2 and Fe-TiO_2 with different doping content before and after acid treatment.

X-ray photoelectron spectroscopy (XPS) was employed as a surface sensitive characterization technique to study the surface element composition of the nanoparticles as explained previously [33]. The XPS survey scans found that the surface of Fe-TiO_2 nanoparticles was composed of Ti, O and Fe elements. Table 4.1 shows the at.% ratio of Fe:Ti in Fe-TiO_2 nanoparticles with different Fe content before and after the acid treatment. The atomic percent (at.%) of Fe decreased significantly after treating the catalyst particles with HCl solution, which was due to the removal of iron oxide layers from the surface of nanoparticles confirming that the amorphous layer observed in HRTEM images (Figure 4.2) was composed of iron oxide layers. It should be mentioned that the at.% of Ti did not change by the acid-treatment.

Table 4.1 Change in at.% of Fe content in Fe-TiO_2 nanoparticles with different Fe content

Catalyst	Fe:Ti	
	before acid treatment	after acid treatment
Fe_1-TiO_2	1.4	0.7
Fe_5-TiO_2	5.1	2.9
Fe_{10}-TiO_2	8.6	5.4

Table 4.2 shows the peak position and FWHM of O, Ti and Fe elements; the two peaks observed in O 1s scan are ascribed to Fe_2O_3, Fe_3O_4, TiO_2 (~530.2 eV) and surface H_2O_2 (~532.1 eV) [122, 123, 176]. The deconvolution of the Ti high resolution scan led to four peaks at 457.8, 458.8, 463.4 and 464.6 eV ascribed to Ti^{3+} $2p_{3/2}$, Ti^{4+} $2p_{3/2}$, Ti^{3+} $2p_{1/2}$ and Ti^{4+} $2p_{1/2}$, respectively. The Ti^{3+} peaks are ascribed to the generated oxygen vacancies, where the oxygen electrons convert Ti^{4+} to Ti^{3+} to preserve the charge balance. It is noteworthy to mention that the Ti^{3+} peaks were not observed in pristine TiO_2. [128-130]. Also, the peaks observed at around 709.3, 710.6, 711.9, 713.7 and 725.2 eV in Fe high resolution spectra confirmed the existence of Fe_2O_3 and Fe_3O_4 [118, 119, 177].

Table 4.2. High resolution XPS spectra of titanium, oxygen and iron

Peak	Position BE (eV)	FWHM (eV)
O 1s	530.2	1.7
	532.1	2.35
Ti $2p_{3/2}$	458.7	1.63
Ti $2p_{1/2}$	464.3	1.92
Fe $2p_{3/2}$	709.3	1.21
	710.6	1.39
	711.9	1.54
	713.7	2.56
Fe $2p_{1/2}$	725.2	3.66

Figure 4.4 depicts the elemental analysis maps of Fe_{10}-TiO_2 before and after acid treatment for Fe, Ti and O; and Table 4.3 shows the change in at.% of Fe:Ti before and after the acid treatment process for the samples with different doping content. The EDX mappings and spectra of $Fe_{0.5}$-TiO_2 and Fe_1-TiO_2 before and after the acid treatment are shown in Figure 4.12 and Figure 4.13.

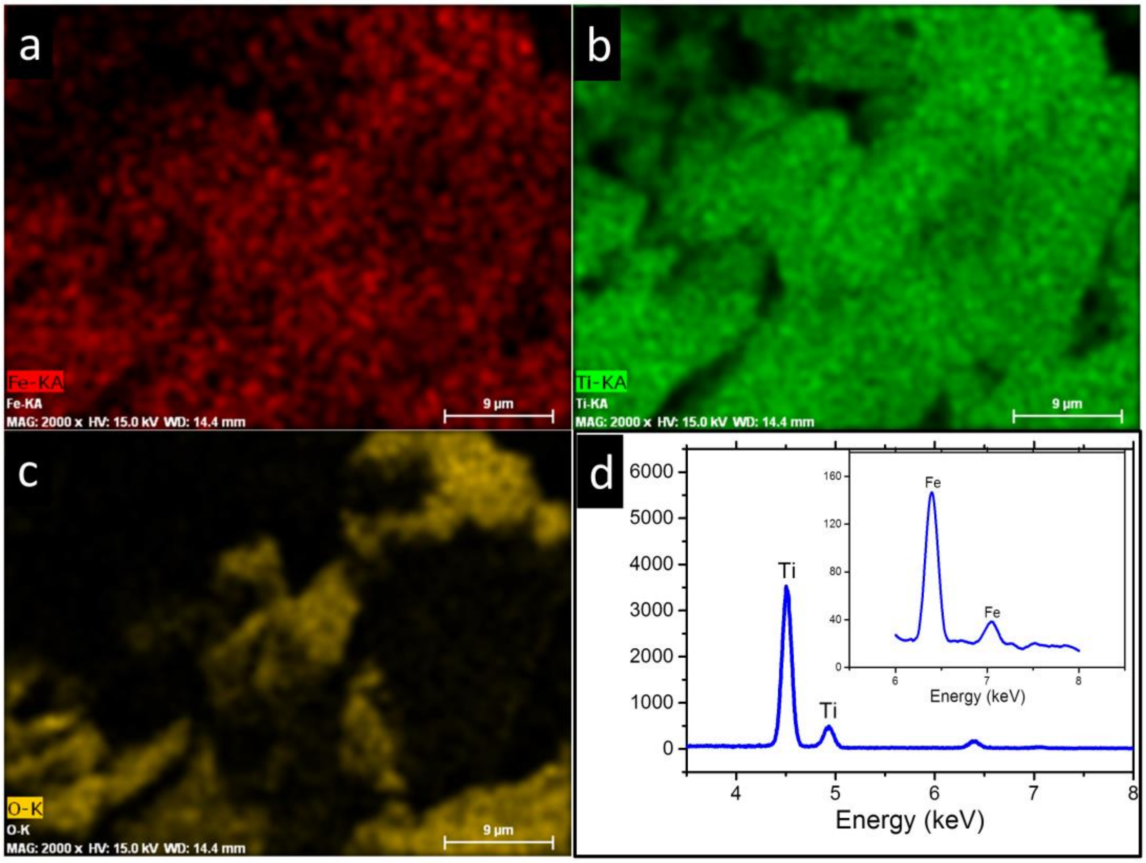
a
Fe-KA
Fe-KA
MAG: 2000 x HV: 15.0 kV WD: 14.4 mm
9 µm
b
Ti-KA
Ti-KA
MAG: 2000 x HV: 15.0 kV WD: 14.4 mm
9 µm
c
O-K
O-K
MAG: 2000 x HV: 15.0 kV WD: 14.4 mm
9 µm
d
6000
5000
4000
3000
2000
1000
0
Ti
Ti
4
5
6
7
8
Energy (keV)
160
120
80
40
0
Fe
Fe
6
7
8
Energy (keV)

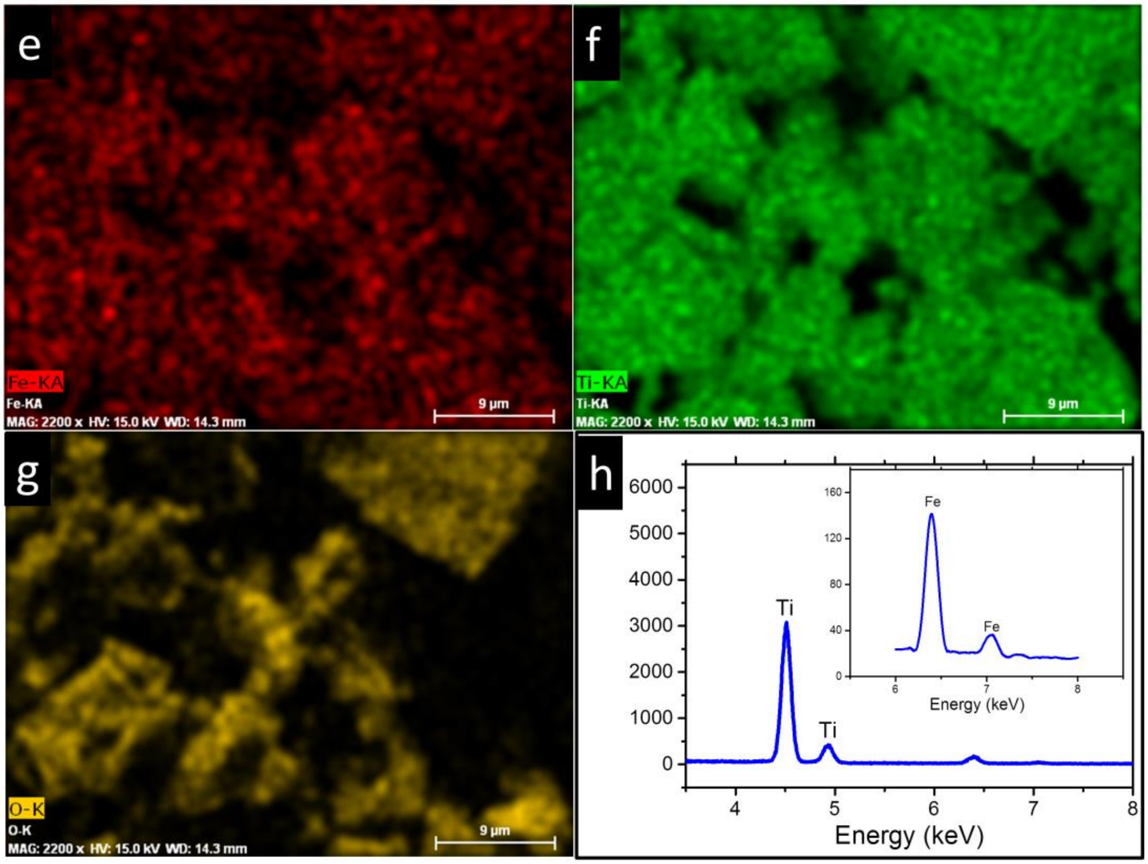

Figure 4.4. Elemental maps of a) Fe, b) Ti, c) O and d) EDX spectrum of Fe_{10}-TiO_2 before acid treatment; elemental maps of e) Fe, f) Ti, g) O and h) EDX spectrum of Fe_{10}-TiO_2 after acid treatment.

The elemental analysis showed the at.% Fe:Ti ratio before the acid treatment: 0.57 (0.37: 64.31), 0.92 (0.66:71.46), 4.8 (2.81:58.54), 10.8 (3.48: 32.18), for $Fe_{0.5}$-TiO_2, Fe_1-TiO_2, Fe_5-TiO_2 and Fe_{10}-TiO_2, respectively. After the acid treatment, the Fe content diminished remarkably about twofold in all of the samples. This is in a complete agreement with the results obtained from the XPS analysis confirming the fact that the iron oxides deposited on the surface are dissolved in the acid solution and removed from the surface of the catalyst.

Table 4.3. The at.% ratio of Fe:Ti before and after the acid treatment obtained using EDX elemental analysis

Catalyst	O		Ti		Fe	
	untreated	acid treated	untreated	acid treated	untreated	acid treated
$Fe_{0.5}$-TiO_2	35.32	14.1	64.31	85.67	0.37	0.23
Fe_{10}-TiO_2	64.34	71.96	32.18	26.72	3.48	1.28
Fe_5-TiO_2	38.65	37.92	58.54	60.55	2.81	1.53
Fe_1-TiO_2	27.88	47.05	71.46	52.56	0.66	0.39

The photocatalytic activity of Fe-TiO_2 was measured using phenol solution under visible light illumination and the effects of iron content, acid treatment of the particles, amount of catalyst in the solution, concentration of pollutant, irradiation time and pH were studied. The Langmuir-Hinshelwood model, which is used to model the kinetics of photocatalytic reactions of organics in aqueous solution, was used to study the photo degradation kinetics. The model relates the reaction rate to the concentration of organic compounds:

$$r = -\frac{dC}{dt} = \frac{k_r K_{ad} C}{1 + K_{ad} + C} \qquad \text{Equation 4.3}$$

where r is the reaction rate, C is the concentration of the organic compound, t is the reaction time, k_r is the intrinsic rate constant and K_{ad} is the adsorption equilibrium constant.

4.3.2 Photocatalytic activity measurements

4.3.2.1 Effect of iron content as dopant

Figure 4.5a illustrates the effect of iron content on the photocatalytic activity of Fe-TiO_2 using 10 mg.L^{-1} of phenol solution within 90 min of reaction time. As the doping content increased the photocatalytic activity decreased. The latter can be explained associated with the fact that Fe^{3+} can trap both electrons and holes up to an optimum amount [178, 179]; as the doping content exceeds this optimum point, it acts as a recombination center for the photo-generated charge carriers having an adverse effect on the photocatalytic activity [169, 180]. It is notable that the DE of the pristine TiO_2 was higher than that of the doped catalysts with high doping content. $Fe_{0.5, pH=3}$-TiO_2 showed a higher photocatalytic activity compared to the ones synthesized in natural pH. This is due to the acidic pH hindering the hydrolysis process that leads to finer catalyst particles [181, 182].

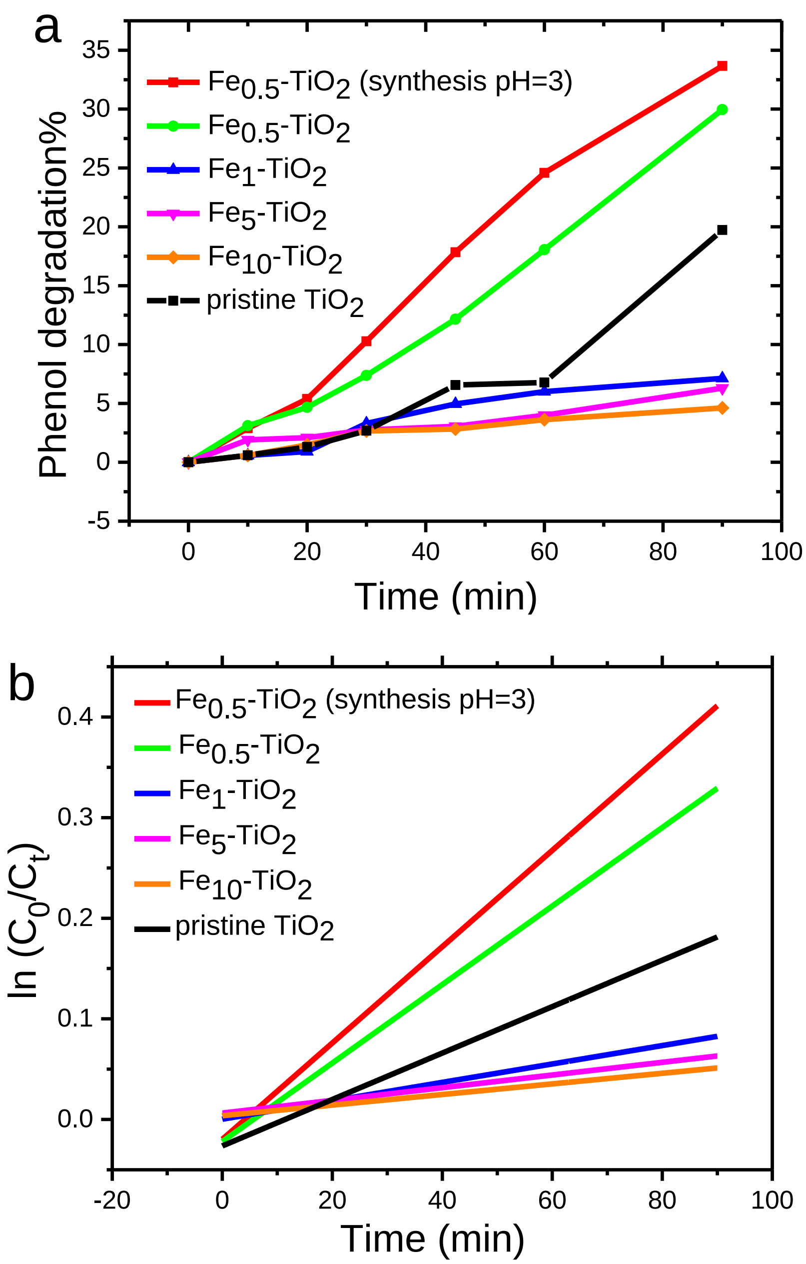

Figure 4.5. The effect of doping content on a) photocatalytic activity and b) kinetics of phenol degradation; catalyst load= 500 mg.L^{-1} and [phenol]$_0$= 10 mg.L^{-1}.

Figure 4.5b and Table 4.4 illustrate the rate constants for different Fe^{3+} content, where k$_{app}$ is the rate constant and R^2 is the (residual)^2 calculated from least squares method. The rate constant decreased significantly by the increase in the doping content from 0.5 to 1 molar% (Fe:Ti).

Table 4.4. The effect of doping content on the rate constant of phenol degradation; catalyst load= 500 mg.L^{-1} and [phenol]$_0$= 10 mg.L^{-1}.

Catalyst	k_{app} (min^{-1})	R^2
pristine TiO_2	0.00231	0.93
$Fe_{0.5,\ pH=3}$-TiO_2	0.00479	0.99
$Fe_{0.5}$-TiO_2	0.0039	0.97
Fe_1-TiO_2	0.0009147	0.92
Fe_5-TiO_2	0.00063	0.94
Fe_{10}-TiO_2	0.000527	0.93

4.3.2.2 Effect of acid treatment and removal of surface iron oxide contaminating layer

Figure 4.6a shows the photocatalytic activity of the Fe-TiO_2 catalysts doped with different amounts of Fe^{3+} treated with the HCl solution using 10 mg.L^{-1} of phenol solution within 90 min of reaction time. Upon applying the acid treatment to the catalyst particles, their photocatalytic activity increased significantly. The DE of $Fe_{0.5,\ pH=3}$-TiO_2 was increased 24% after the acid treatment. This increase was even more remarkable in the samples with higher amount of iron. For instance, the DE of Fe_{10}-TiO_2 increased by the factor of 2.5. As shown in the HRTEM images and XPS data, only a portion of Fe^{3+} is doped in the crystal lattice of TiO_2 and the remaining is deposited on the surface of the particles in various forms of iron oxides. This deposited layer contaminates the surface, where the majority of photocatalytic reactions take place; hence, it reduces the reactive sites for photocatalytic reactions and diminishes the photocatalytic activity. In addition, this contamination layer acts as a recombination center for the photo-generated electrons and holes and reduces their chance to reach to the surface to initiate the photocatalytic reactions. The improvement in the DE was due to the removal of this layer from the particles’ surface. Also, it should be mentioned that the DE of the Fe_1-TiO_2 before the acid treatment was less than the pristine TiO_2 and after the acid treatment it increased to a higher DE than that of the pristine TiO_2. Figure 4.6b and Table 4.5 show the rate constants for the catalysts with different amounts of doping content after the acid treatment process.

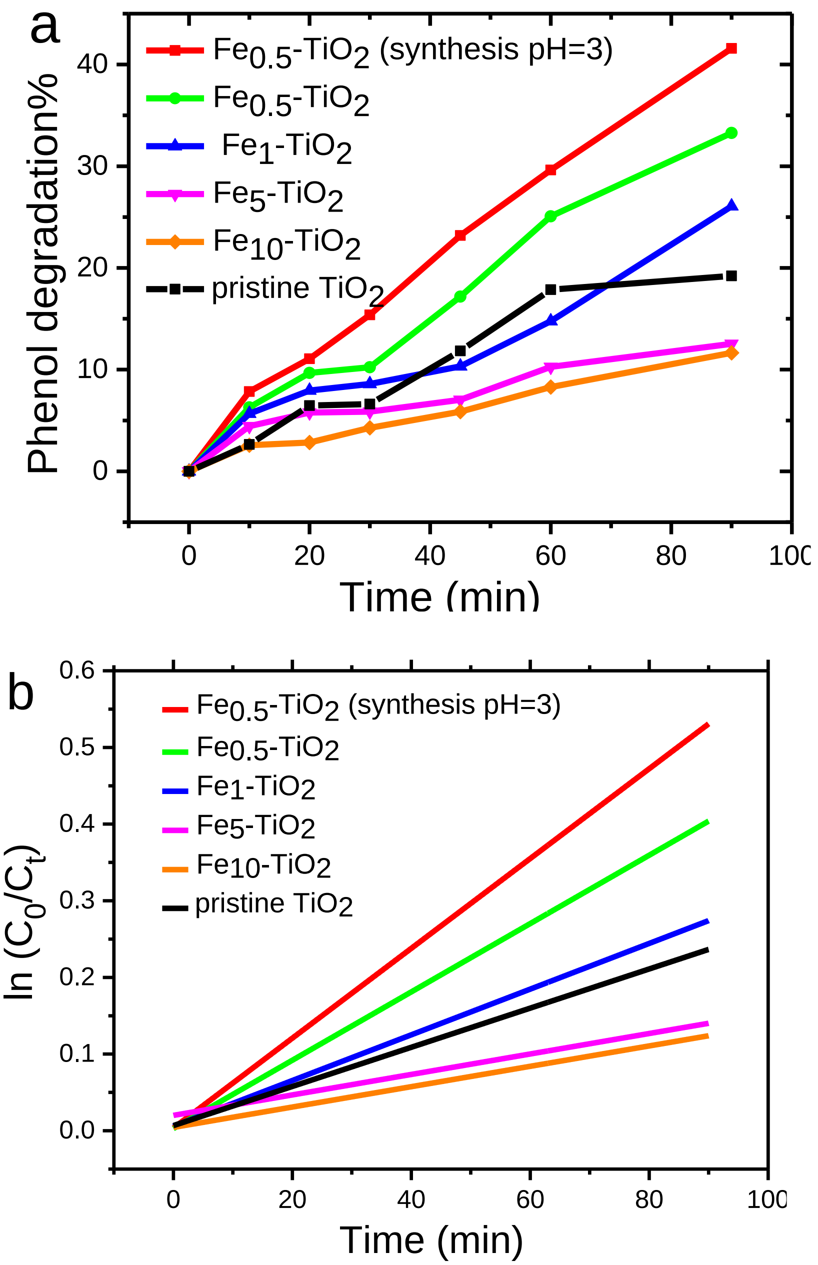

Figure 4.6. a) photocatalytic activity and b) kinetics of phenol degradation after the acid treatment; catalyst load= 500 mg.L^{-1}, [phenol]$_0$= 10 mg.L^{-1}.

Comparing the rate constants of the photocatalytic reactions before (Table 4.4) and after acid treatment (Table 4.5), the k$_{app}$ of the particles with higher amounts of Fe doping increased further subsequent to the acid treatment. In the samples with higher doping content, more iron was used in the doping process compared to the ones with less amount of doping content that produced more contamination layers on their surface. Upon applying the acid treatment, they show more improvement in their k_{app} and photocatalytic activity.

Table 4.5. The rate constants of phenol degradation after the acid treatment; catalyst load= 500 mg.L^{-1} and [phenol]$_0$= 10 mg.L^{-1}.

Catalyst	k_{app} (min^{-1})	R^2
pristine TiO_2	0.00255	0.93
$Fe_{0.5,\ pH=3}$-TiO_2	0.00586	0.99
$Fe_{0.5}$-TiO_2	0.00446	0.98
Fe_1-TiO_2	0.00298	0.93
Fe_5-TiO_2	0.00134	0.91
Fe_{10}-TiO_2	0.00133	0.99

4.3.2.3 Effect of catalyst load

The effect of catalyst load on DE was studied using 20 mg.L^{-1} of phenol solution and 200, 500, 1000, 1500 and 3000 mg.L^{-1} of $Fe_{0.5,\ pH=3}$-TiO_2. As shown in Figure 4.7a, the DE obtained with 200 mg.L^{-1} of the catalyst load was 18% and the DE increased remarkably to 78% employing 3000 mg.L^{-1} of the catalyst load within 90 min of reaction time. Such an improvement resulted from more catalyst particles contributing to the photocatalytic reactions. Figure 4.7b plots the theoretical and experimental rate constants for different catalyst loads in the reaction solution. In the theoretical rate constants, it was assumed that the rate constant increases proportional to the increase in the catalyst load. However, it can be seen that as the catalyst load increases, the difference between the theoretical and experimental rate constants increases. This is due to the fact that by the increase of catalyst load up to an optimum point the DE increases; however, after the optimum point the catalyst particles block the irradiated, which results into the lower photocatalytic activity.

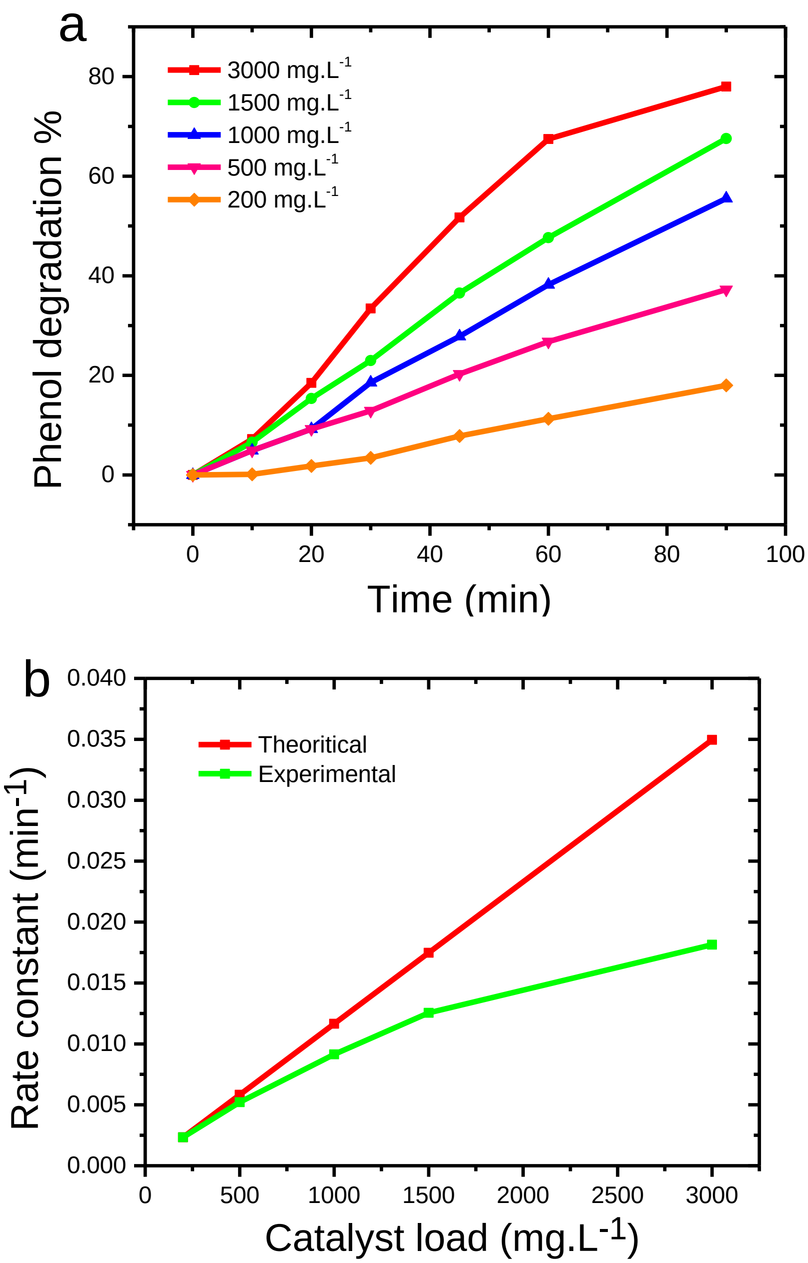

Figure 4.7. The effect of catalyst load on a) photocatalytic activity and b) rate constant of phenol using acid treated Fe$_{0.5,\ pH=3}$-TiO$_2$, [phenol]$_0$= 20 mg.L^{-1}.

4.3.2.4 Effect of reaction time

The photocatalytic performance was measured within 6 hours for 20 mg.L^{-1}of phenol solution using 1000 mg.L^{-1} of the catalyst load (Fe$_{0.5,\ pH=3}$-TiO$_2$). As shown in Figure 4.8a, the DE increases with the time and 87% DE was obtained after 6 hours of reaction time. As the reaction continues, less phenol molecules would be available to the catalyst particles. hence, the reaction rate decreases gradually (Figure 4.8b).

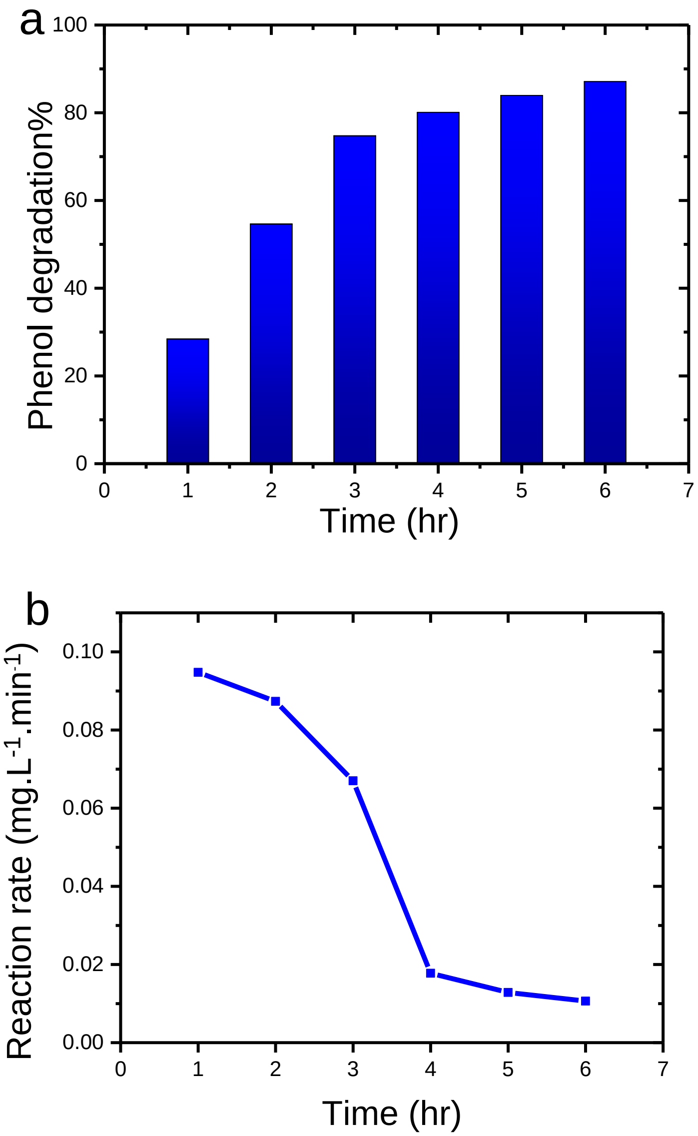

Figure 4.8. The effect of reaction time on a) photocatalytic activity and b) reaction rate of phenol degradation, catalyst load= 1000 mg.L^{-1}, [phenol]$_0$= 20 mg.L^{-1}.

4.3.2.5 Effect of initial concentration of phenol

The effect of initial pollutant concentration on DE was studied using different amounts of phenol concentration (10, 20, 50 and 100 mg.L^{-1}) and a constant catalyst load ($Fe_{0.5, pH=3}$-TiO_2) of 500 mg.L^{-1}. From Figure 4.9a, the DE decreases with an increase in the pollutant concentration.

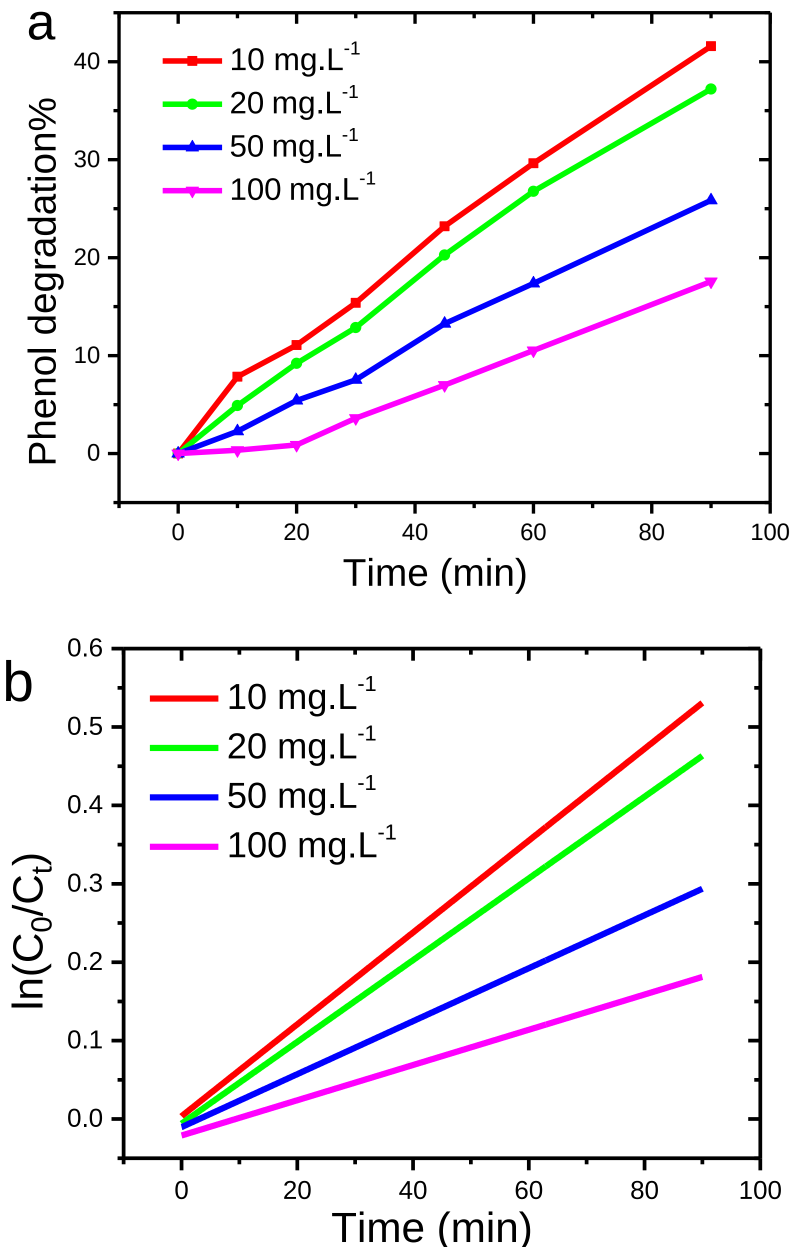

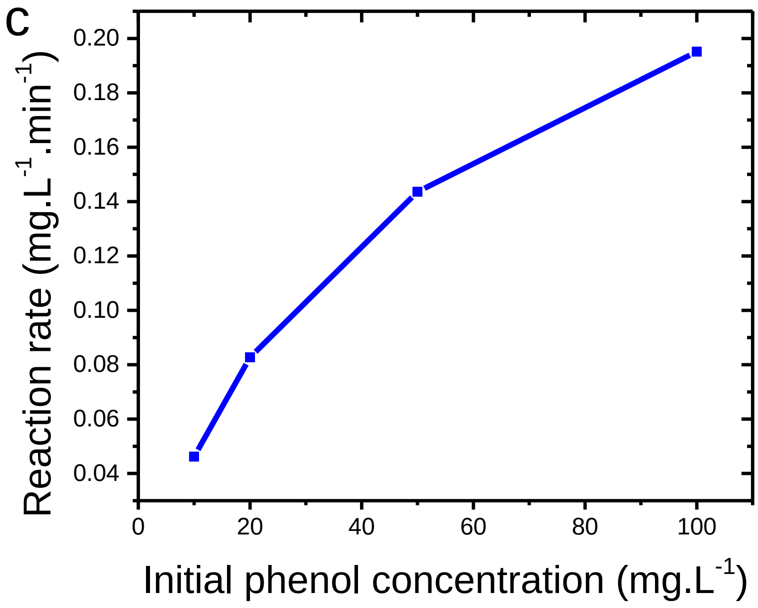

Figure 4.9. The effect of initial phenol concentration on a) photocatalytic activity, b) rate constant and c) reaction rate; catalyst load= 500 mg.L^{-1} ($Fe_{0.5,\ pH=3}$-TiO_2) and reaction time= 90 min.

The rate constants (Figure 4.9b and Table 4.6) decrease with the increase in the phenol concentration. Since the catalyst load is kept constant while the initial phenol concentration increases, the photocatalytic activity decreases. However, as shown in Figure 4.9c, the reaction rate within 90 min of reaction time increases with the increase in the initial phenol concentration. As the initial phenol concentration increases there are more phenol molecules available for the catalyst particles to continuously participate in the photocatalytic reactions.

Table 4.6. The effect of initial phenol concentration on the rate constants; catalyst load= 500 mg.L^{-1}.

Phenol concentration (mg.L^{-1})	k_{app} (min^{-1})	R^2
10	0.00586	0.99
20	0.00521	0.99
50	0.00338	0.99
100	0.00225	0.96

4.3.2.6 Effect of pH

Variation in pH of the solution affects the surface characteristics of the catalyst particles, generation and scavenging of hydroxyl radicals and also leads to the formation of different phenol species. Hence, it is important to study the photocatalytic activity within different pH ranges. Figure 4.10 illustrates the effect of pH on photocatalytic degradation of 10 mg.L^{-1} of phenol solution. The best results were obtained in mild alkaline (pH=8, 57% DE) and mild acidic (pH=5.5, 56% DE) pHs. Further decrease (pH=4.5, 37% DE) and increase (pH=9, 16% DE) in the pH of the solution had an adverse effect on the photocatalytic activity. According to point of zero charge (pzc), the surface of TiO_2 is negatively charged in alkaline pHs and conversely, positively charged in acidic pHs. In mild alkaline pHs, hydroxide ions facilitate generation of hydroxyl radicals through the reaction of the hydroxide ions with the holes in the valence band of TiO_2 [183, 184]. In a harsh alkaline condition, the Coulombic repulsion between the hydroxide anions and negatively charged surface of TiO_2 impedes the hydroxyl radical generation [162]. Moreover, phenolate anion is dominated specie of phenol molecule in extreme alkaline pHs, which causes a repulsive force between the high soluble phenolate anion and negatively charged TiO_2 surface. Although the harsh acidic pH is not favorable for photocatalytic activity, the electrostatic attraction between the positively charge on TiO_2 surface and the phenol molecule, and also low solubility of phenol within the low acidic pH range enhances the adsorption of phenol on the catalyst particles' surface, which is advantageous to the photocatalytic reactions [185].

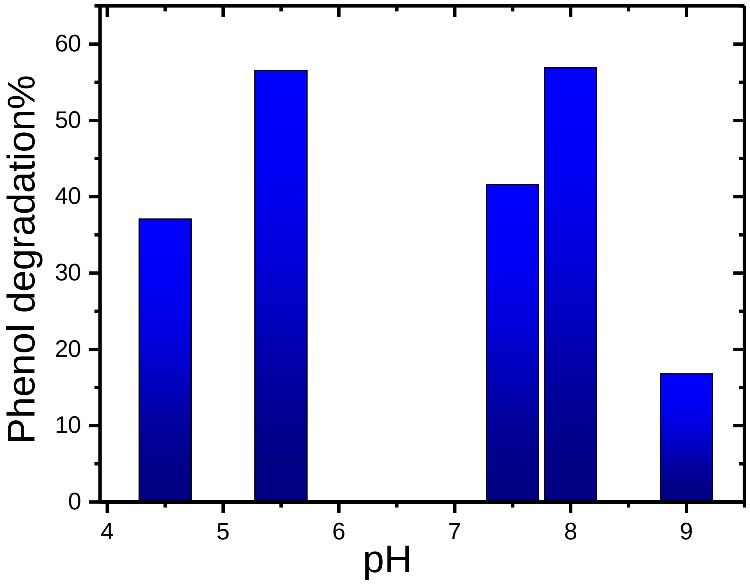

Figure 4.10. The effect of pH on the photocatalytic activity; catalyst load= 500 $mg.L^{-1}$and $[phenol]_0$= 10 $mg.L^{-1}$.

4.4 Conclusions

The Fe-TiO_2 with different amounts of Fe^{3+} was synthesized successfully using the sol-gel method. The UV-vis absorption spectra of Fe-TiO_2 had a red shift towards visible light due to the doped Fe3+ in the crystal lattice of the particles, whereas the pristine TiO_2 had activity only within the UV region. An amorphous contamination layer was found on the surface of the particles using TEM imaging. XPS showed that the layer is composed of iron oxide, which was deposited on the surface of the nanoparticles during the synthesis step. The layer was removed using concentrated HCl solution and its removal was confirmed by TEM, XPS and EDX. EDX chemical analysis showed that the concentration of iron decreased significantly by acid treatment. XPS proved that such a decrease was due to the removal of the surface iron oxide. Degradation of phenol was used to measure the photocatalytic activity of the nanoparticles. It was observed that although the increase in the doping content increases the red shift, it deteriorates the photocatalytic activity. The removal of surface iron oxide layer improved the degradation efficiency significantly. Also, the increase in the catalyst load increased the photocatalytic activity up to an optimum point and after that it has an adverse effect on the reaction rate. The pH played an important role in the degradation efficiency of the catalyst particles, where the highest photocatalytic activity was obtained operating under mild acidic and basic pHs. the photocatalytic activity was increased up to 73% by the removal of iron oxide and working under the optimum pH condition.

4.5 Supporting information

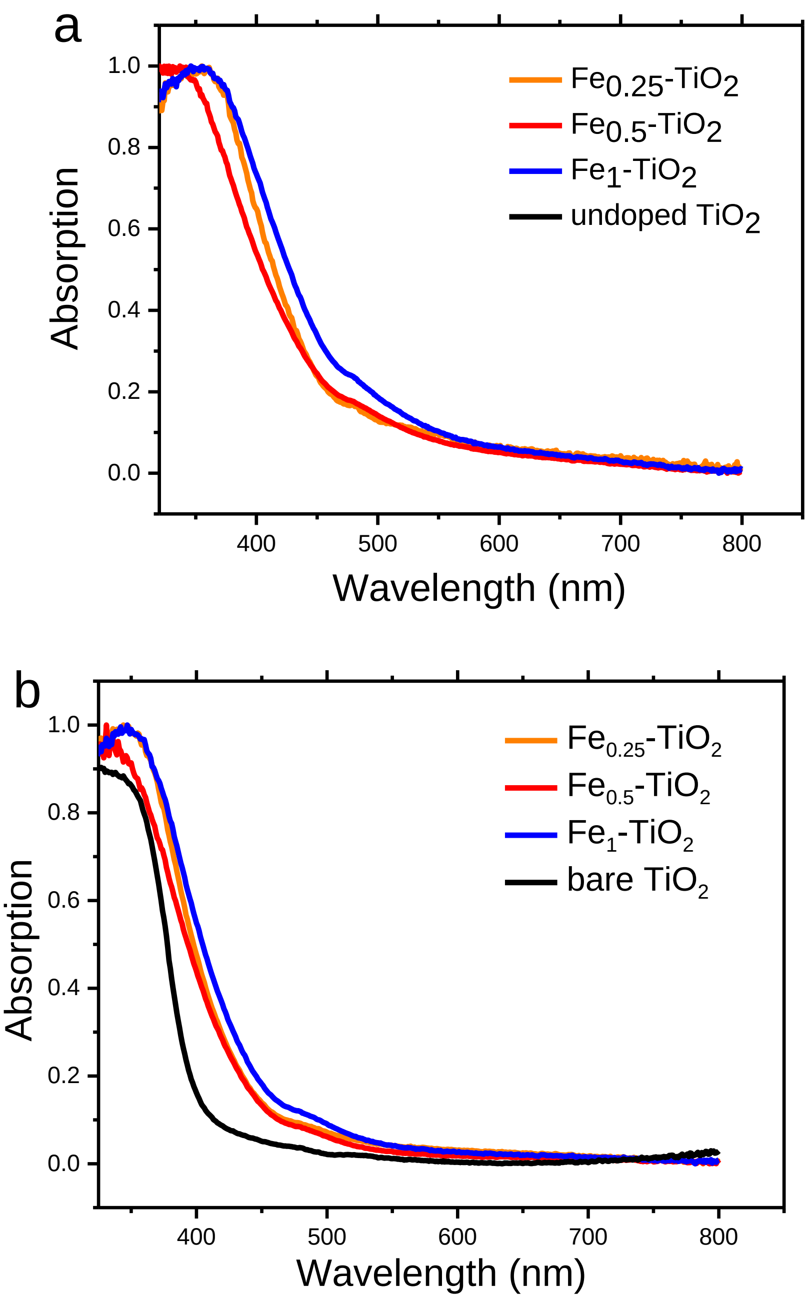

Figure 4.11. UV-vis absorption spectra of Fe-TiO_2 with different amounts of the doping content a) before and b) after acid treatment

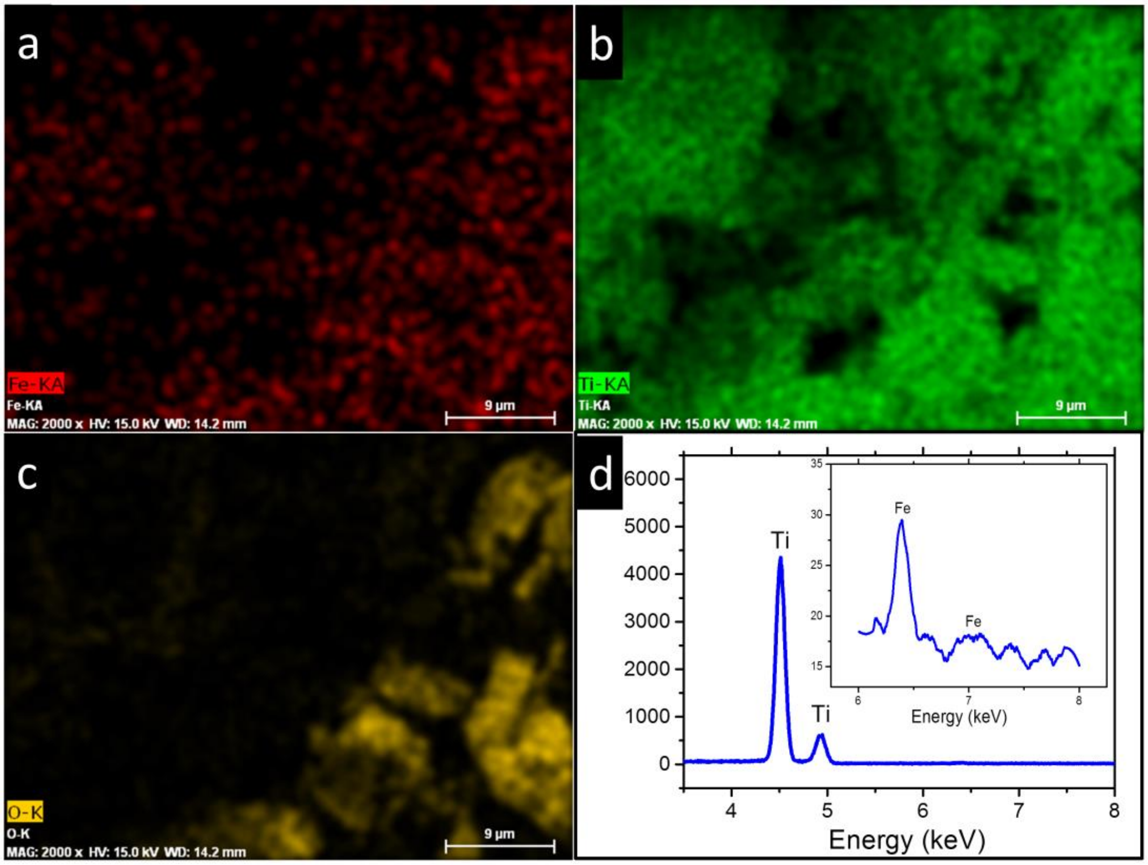
a
Fe-KA
Fe-KA
MAG: 2000 x HV: 15.0 kV WD: 14.2 mm
9 µm
b
Ti-KA
Ti-KA
MAG: 2000 x HV: 15.0 kV WD: 14.2 mm
9 µm
c
O-K
O-K
MAG: 2000 x HV: 15.0 kV WD: 14.2 mm
9 µm
d
6000
5000
4000
3000
2000
1000
0
Ti
Ti
4
5
6
7
8
Energy (keV)
35
30
25
20
15
Fe
Fe
6
7
8
Energy (keV)

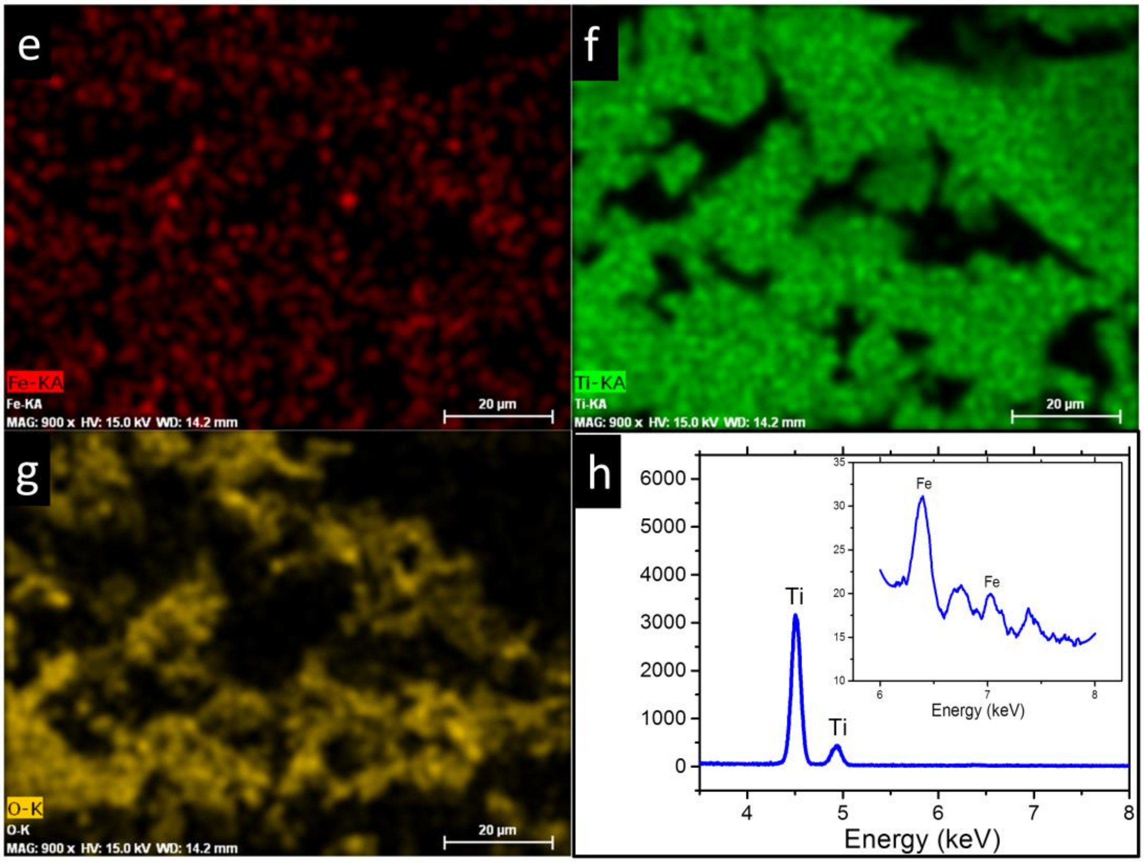

Figure 4.12. Elemental maps of a) Fe, b) Ti, c) O and d) EDX spectrum of $Fe_{0.5}$-TiO_2 before acid treatment; elemental maps of e) Fe, f) Ti, g) O and h) EDX spectrum of F0.5-TiO_2 after acid treatment.

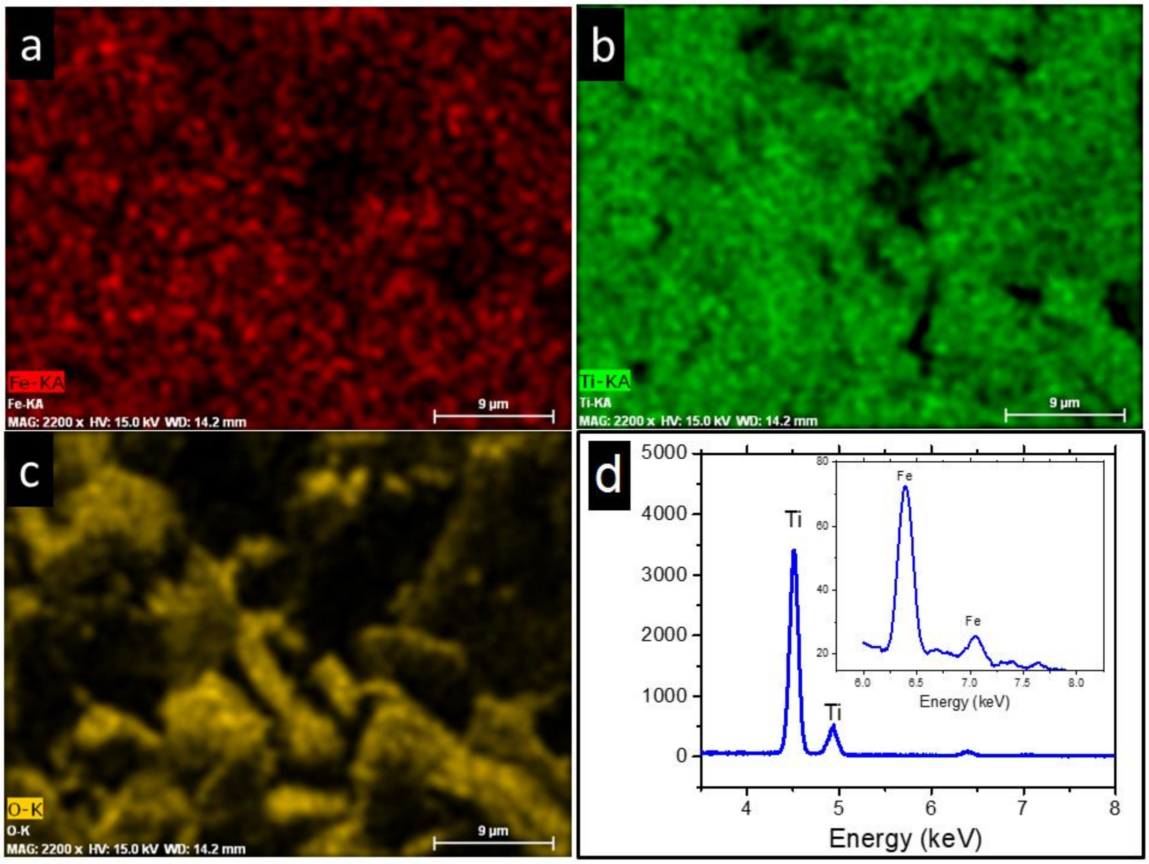
a
Fe-KA
Fe-KA
MAG: 2200 x HV: 15.0 kV WD: 14.2 mm
9 µm
b
Ti-KA
Ti-KA
MAG: 2200 x HV: 15.0 kV WD: 14.2 mm
9 µm
c
O-K
O-K
MAG: 2200 x HV: 15.0 kV WD: 14.2 mm
9 µm
d
5000
4000
3000
2000
1000
0
Ti
Ti
4
5
6
7
8
Energy (keV)
80
60
40
20
Fe
Fe
6.0
6.5
7.0
7.5
8.0
Energy (keV)

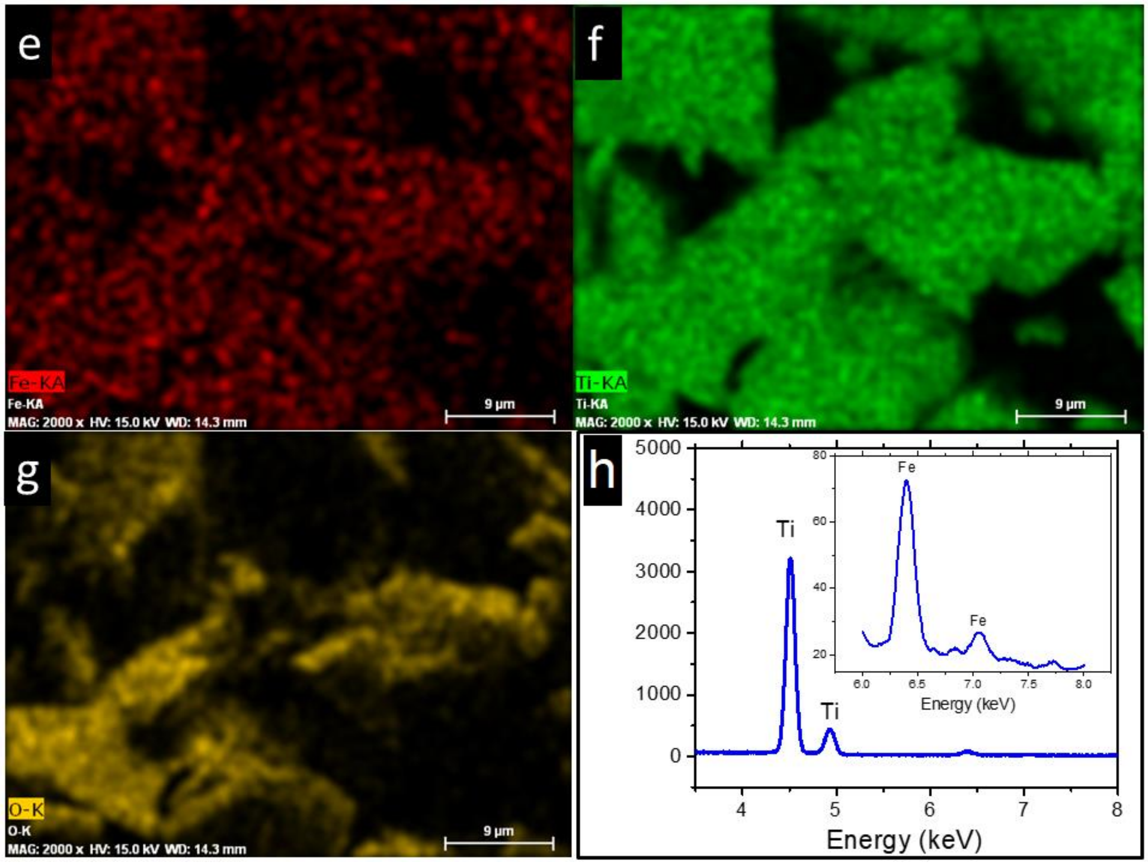

Figure 4.13. Elemental maps of a) Fe, b) Ti, c) O and d) EDX spectrum of Fe_5-TiO_2 before acid treatment; elemental maps of e) Fe, f) Ti, g) O and h) EDX spectrum of Fe_5-TiO_2 after acid treatment.

Chapter 5 Conclusions and Future Work

5.1 Conclusions

This dissertation describes a facile sol-gel method to synthesize bare (undoped) and Fe doped TiO_2 nanoparticles for wastewater treatment under visible light irradiation. The focus of this work was to find the reasons behind the low photocatalytic activity of Fe-TiO_2 and then to improve its photocatalytic activity. The optimum conditions to synthesize the Fe-TiO_2 photocatalyst were obtained. The properties of Fe-TiO_2 were characterized using XRD, SAED, TEM, HRTEM, XPS, DRS and EDX. Also, the optimum conditions for degradation efficiency were obtained using phenol as the representative pollutant. The DE was optimized for different reaction conditions such as the effect of the removal of the contamination layer from the surface of the Fe-TiO_2 nanoparticles, catalyst load, reaction time, the pollutant's initial concentration and the pH of the solution. Moreover, the kinetics of the photocatalytic reactions were studied thoroughly for a better understanding of the process and optimum reaction conditions.

Chapter 3 investigated the reason behind the low photocatalytic activity of the Fe-TiO_2. An iron oxide contamination layer was found out on the surface of the nanoparticles, which increased the electron/hole recombination centers and decreased the surface area of the nanoparticles. The iron oxide contamination layer was removed using an acid treatment process by means of concentrated HCl solution. In addition, the effect of the Fe content on the crystal lattice and optical properties of the nanoparticles were studied. Methyl orange was used as the pollutant to investigate the effect of removing the contamination layer and also for the doping content on the DE under visible light irradiation.

Chapter 4 focused on the practical applications of the synthesized photocatalyst in degradation of phenol solution under visible light irradiation. Different influencing parameters on the DE of the nanoparticles were taken into consideration and the kinetics of the reaction under different conditions were investigated to find the efficient conditions for practical use of the photocatalyst.

The key findings and contributions of this work are categorized into synthesis and characterization of the catalyst, and its practical use in degradation of organic pollution and optimizing the photocatalytic reaction conditions and kinetics study as follows:

5.1.1 Synthesis and characterization

1. **The effect of synthesis pH on the crystallite size of the nanoparticles**

   The catalyst was synthesized in natural pH of the solution and also in acidic pH of 3. The nanoparticles synthesized in the acidic pH had a smaller crystallite size due to its inhibition of the hydrolysis step leading to finer nanoparticles. The smaller the size, the higher the photocatalytic activity obtained due to the larger surface area.

2. **The effect of the Fe doping content on the crystallinity and crystallite size of the nanoparticles**

   The XRD patterns showed that the increase in the amount of Fe^{3+} in the Fe-TiO_2 crystal lattice caused a decrease in the crystallinity of the nanoparticles. This is due to the restraint of the crystal growth by introducing the Fe^{3+} dopant. Also, the crystallite size was measured using the Scherrer equation. The size decreased gradually from 13 nm for the bare TiO_2 nanoparticles to 5.9 nm for the Fe_{10}-TiO_2, the highest amount of the doping content.

3. The effect of the Fe doping content on the lattice parameters

Different Fe:Ti molar% ratios were used to synthesized the nanoparticles. The effect of the doping content on the lattice parameter was studied using SAED. It was observed that by increasing the doping content, the lattice parameter increased. This is attributed to the larger ionic radius of Fe^{3+} compared to that of Ti^{4+}.

4. The effect of HCl acid treatment on the photocatalytic activity of Fe-TiO_2

An amorphous layer was found on the surface of the nanoparticles using TEM and HRTEM. XPS showed that the amorphous layer is composed of iron oxide. This layer contaminates the surface and decreases the accessible sites for the photocatalytic reactions to take place. Also, it acts as a recombination center for the photo-generated charge carriers, which decreases the photocatalytic activity. The contamination layer was removed by concentrated HCl acid treatment process; HRTEM and XPS and EDX showed that the concentration of surface iron oxide decreased dramatically resulting in the DE increasing significantly upon the removal of the contamination layer.

5.1.2 Optimizing the photocatalytic reaction conditions and kinetics study

1. The effect of Fe doping content on the optical properties of the nanoparticles

Using DRS measurements it was found out that by the incorporation of the Fe^{3+} in the crystal lattice of TiO_2, the absorption of TiO_2 shifted from UV light to visible light. Also, as the concentration of the dopant increased the red shift towards longer wavelengths increased. The red shift was interpreted to be due to the interaction of the d orbitals of Fe^{3+} with the 3d orbitals of Ti^{4+} producing intermediate band gap energies. The band gap energies were calculated from Tauc function plots that showed the band gap energy of the bare TiO_2 was 3.3 eV, which decreased gradually upon increasing the doping content to 2.7 eV for Fe_{10}-TiO_2.

2. **The effect of the catalyst load in the solution on the photocatalytic activity**

   As the amount of the photocatalyst increased the DE increased. However, there is an optimum amount for the catalyst load and exceeding that optimum point has an adverse effect on the reaction rate and DE. In our case, after 1500 mg.L^{-1} of the catalyst load the increase in the DE was not as much expected. The increase in the catalyst load that exceeds the optimum amount blocks the irradiated light to the solution resulting in a lower DE.

3. **The effect of reaction time on the photocatalytic activity**

   It was found that although the DE increased as the reaction time increased, the reaction rate decreased. This is attributed to having less pollutant molecules around the photocatalyst nanoparticles to react with; therefore, the reaction rate decreased.

4. **The effect of the initial concentration of the pollutant in the water on the photocatalytic activity**

   The increase in the concentration of the pollutant with a constant amount of catalyst load decreased the DE. The photocatalytic reaction rate increased since there were more available pollutant molecules for the photocatalyst nanoparticles to degrade.

5. **The effect of pH of the solution on the photocatalytic activity**

   The pH was an important factor in the photocatalytic degradation of phenol. The best results were obtained using mild acidic and mild alkaline pHs. The generation of hydroxyl radicals were facilitated in the mild alkaline pHs. The electrostatic attraction between the phenol molecule and the positively charged surface of TiO_2 as well as low solubility of phenol in mild acidic pHs increased the adsorption of light leading to higher DE.

5.1.3 The applications and the impacts of this research work

The prepared Fe doped titania photocatalyst with significantly enhanced photocatalytic activity under visible light irradiation has the potential to be utilized for various applications including wastewater treatment and water and air purification and disinfection, sterilization and self-cleaning surfaces. Considering the effectiveness of the prepared photocatalyst in degradation of organic pollution under visible light irradiation, the huge positive impact of this research in cleaning the environment is appreciable.

5.2 Future work

The results obtained in this research improved the photocatalytic activity of Fe-TiO_2 significantly. However, this research work can still be improved by some modifications to be developed further.

- The impact of the acid treatment time should be studied further since it might remove more of the contamination layer that could lead to a higher photocatalytic activity.
- The acid treatment process introduced in this research work might be advantageous to other catalysts with other dopants as well. So, its impact on them can be studied and the acid treatment process might be introduced as a general method for the improvement of the photocatalytic activity using doped photocatalysts.
- The Fe-TiO_2 nanoparticles can be coated on the surface of a substrate and their photocatalytic activity as a fixed bed photo-reactor can be measured.
- Other metal or non-metal co-dopants can be used in the doping process to study their synergistic effect on the photocatalytic activity.

Chapter 6 Bibliography

1. Mestre, A.S., et al., *Enhanced clofibric acid removal by activated carbons: Water hardness as a key parameter.* Chemical Engineering Journal, 2016. **286**: p. 538-548.

2. Saththasivam, J., K. Loganathan, and S. Sarp, *An overview of oil–water separation using gas flotation systems.* Chemosphere, 2016. **144**: p. 671-680.

3. Steliga, T., P. Jakubowicz, and P. Kapusta, *Changes in toxicity during treatment of wastewater from oil plant contaminated with petroleum hydrocarbons.* Journal of Chemical Technology & Biotechnology, 2015. **90**(8): p. 1408-1418.

4. Gough, R., et al., *Dissolved organic carbon and trihalomethane precursor removal at a UK upland water treatment works.* Science of The Total Environment, 2014. **468–469**: p. 228-239.

5. Liu, Y.-J., et al., *Removal of nonsteroidal anti-inflammatory drugs (NSAIDs) by electrocoagulation–flotation with a cationic surfactant.* Separation and Purification Technology, 2015. **152**: p. 148-154.

6. Cechinel, M.A.P., et al., *Removal of metal ions from a petrochemical wastewater using brown macro-algae as natural cation-exchangers.* Chemical Engineering Journal, 2016. **286**: p. 1-15.

7. Li, X., et al., *An efficient and green pretreatment to stimulate short-chain fatty acids production from waste activated sludge anaerobic fermentation using free nitrous acid.* Chemosphere, 2016. **144**: p. 160-167.

8. Martínez-García, C.G., C. Fall, and M.T. Olguín, *Activated sludge mass reduction and biodegradability of the endogenous residues by digestion under different aerobic to anaerobic conditions: Comparison and modeling.* Bioresource Technology, 2016. **203**: p. 32-41.

9. Tisa, F., A.A. Abdul Raman, and W.M.A. Wan Daud, *Applicability of fluidized bed reactor in recalcitrant compound degradation through advanced oxidation processes: A review.* Journal of Environmental Management, 2014. **146**: p. 260-275.

10. Slokar, Y.M. and A. Majcen Le Marechal, *Methods of decoloration of textile wastewaters.* Dyes and Pigments, 1998. **37**(4): p. 335-356.

11. Chou, S. and C. Huang, *Application of a supported iron oxyhydroxide catalyst in oxidation of benzoic acid by hydrogen peroxide.* Chemosphere, 1999. **38**(12): p. 2719-2731.

12. Pilli, S., et al., *Overview of Fenton pre-treatment of sludge aiming to enhance anaerobic digestion.* Reviews in Environmental Science and Bio/Technology, 2015. **14**(3): p. 453-472.

13. Rahim Pouran, S., A.R. Abdul Aziz, and W.M.A. Wan Daud, *Review on the main advances in photo-Fenton oxidation system for recalcitrant wastewaters.* Journal of Industrial and Engineering Chemistry, 2015. **21**: p. 53-69.

14. Xiao, J., Y. Xie, and H. Cao, *Organic pollutants removal in wastewater by heterogeneous photocatalytic ozonation.* Chemosphere, 2015. **121**: p. 1-17.

15. Magureanu, M., N.B. Mandache, and V.I. Parvulescu, *Degradation of pharmaceutical compounds in water by non-thermal plasma treatment.* Water Research, 2015. **81**: p. 124-136.

16. Xin, L., et al., *Degradation of triclosan in aqueous solution by dielectric barrier discharge plasma combined with activated carbon fibers.* Chemosphere, 2016. **144**: p. 855-863.

17. Shu, H.-Y., M.-C. Chang, and W.-P. Hsieh, *Remedy of dye manufacturing process effluent by UV/*H_2O_2 *process.* Journal of Hazardous Materials, 2006. **128**(1): p. 60-66.

18. Saien, J., V. Moradi, and A.-R. Soleymani, *Investigation of a jet mixing photo-reactor device for rapid dye discoloration and aromatic degradation via UV/*H_2O_2 *process.* Chemical Engineering Journal, 2012. **183**: p. 135-140.

19. Devi, L.G. and R. Kavitha, *A review on non metal ion doped titania for the photocatalytic degradation of organic pollutants under UV/solar light: Role of photogenerated charge carrier dynamics in enhancing the activity.* Applied Catalysis B: Environmental, 2013. **140–141**: p. 559-587.

20. Kumar, S.G. and L.G. Devi, *Review on Modified* TiO_2 *Photocatalysis under UV/Visible Light: Selected Results and Related Mechanisms on Interfacial Charge Carrier Transfer Dynamics.* The Journal of Physical Chemistry A, 2011. **115**(46): p. 13211-13241.

21. Rauf, M.A., M.A. Meetani, and S. Hisaindee, *An overview on the photocatalytic degradation of azo dyes in the presence of* TiO_2 *doped with selective transition metals.* Desalination, 2011. **276**(1): p. 13-27.

22. García-Montaño, J., et al., *Pilot plant scale reactive dyes degradation by solar photo-Fenton and biological processes.* Journal of Photochemistry and Photobiology A: Chemistry, 2008. **195**(2): p. 205-214.

23. Cheng, M., et al., *Hydroxyl radicals based advanced oxidation processes (AOPs) for remediation of soils contaminated with organic compounds: A review.* Chemical Engineering Journal, 2016. **284**: p. 582-598.

24. Hao, C., et al., *Liquid phase-based ultrasonic-assisted synthesis of G–ZnO nanocomposites and its sunlight photocatalytic activity.* Materials & Design, 2016. **89**: p. 864-871.

25. Eley, C., et al., *Nanojunction-Mediated Photocatalytic Enhancement in Heterostructured CdS/ZnO, CdSe/ZnO, and CdTe/ZnO Nanocrystals.* Angewandte Chemie International Edition, 2014. **53**(30): p. 7838-7842.

26. Hunge, Y.M., et al., *Visible light catalysis of methyl orange using nanostructured* WO_3 *thin films.* Ceramics International, 2016. **42**(1): p. 789-798.

27. Pattanaik, P. and M.K. Sahoo, TiO_2 *photocatalysis: progress from fundamentals to modification technology.* Desalination and Water Treatment, 2014. **52**(34-36): p. 6567-6590.

28. Daghrir, R., P. Drogui, and D. Robert, *Modified* TiO_2 *For Environmental Photocatalytic Applications: A Review.* Industrial & Engineering Chemistry Research, 2013. **52**(10): p. 3581-3599.

29. Mohapatra, D.P., et al., *Analysis and advanced oxidation treatment of a persistent pharmaceutical compound in wastewater and wastewater sludge-carbamazepine.* Science of The Total Environment, 2014. **470**: p. 58-75.

30. Pan, L., et al., *Photoisomerization of Norbornadiene to Quadricyclane Using Transition Metal Doped* TiO_2. Industrial & Engineering Chemistry Research, 2010. **49**(18): p. 8526-8531.

31. Zhou, J., et al., *Photodegradation of Benzoic Acid over Metal-Doped* TiO_2. Industrial & Engineering Chemistry Research, 2006. **45**(10): p. 3503-3511.

32. Sidheswaran, M. and L.L. Tavlarides, *Characterization and Visible Light Photocatalytic Activity of Cerium- and Iron-Doped Titanium Dioxide Sol−Gel Materials.* Industrial & Engineering Chemistry Research, 2009. **48**(23): p. 10292-10306.

33. Moradi, V., et al., *Significant improvement in visible light photocatalytic activity of Fe doped* TiO_2 *using an acid treatment process.* Applied Surface Science, 2018. **427**(Part B): p. 791-799.

34. Zhang, G., et al., *Synthesis of nano-*TiO_2*/diatomite composite and its photocatalytic degradation of gaseous formaldehyde.* Applied Surface Science, 2017. **412**: p. 105-112.

35. Sang, L., Y. Zhao, and C. Burda, TiO_2 *Nanoparticles as Functional Building Blocks.* Chemical Reviews, 2014. **114**(19): p. 9283-9318.

36. Mo, S.-D. and W.Y. Ching, *Electronic and optical properties of three phases of titanium dioxide: Rutile, anatase, and brookite.* Physical Review B, 1995. **51**(19): p. 13023-13032.

37. Jie, H., et al., *Nitrogen-doped TiO nanopowders prepared by chemical vapor synthesis: band structure and photocatalytic activity under visible light.* Research on Chemical Intermediates, 2012. **38**(6): p. 1171-1180.

38. Wu, G. and A. Chen, *Direct growth of F-doped* TiO_2 *particulate thin films with high photocatalytic activity for environmental applications.* Journal of Photochemistry and Photobiology A: Chemistry, 2008. **195**(1): p. 47-53.

39. Bang, J.H. and K.S. Suslick, *Applications of Ultrasound to the Synthesis of Nanostructured Materials.* Advanced Materials, 2010. **22**(10): p. 1039-1059.

40. Qin, D.-D., et al., *Facile Solvothermal Method for Fabricating Arrays of Vertically Oriented α-Fe2O3 Nanowires and Their Application in Photoelectrochemical Water Oxidation.* Energy & Fuels, 2011. **25**(11): p. 5257-5263.

41. Wang, Y., et al., *Review of the progress in preparing nano* TiO_2*: An important environmental engineering material.* Journal of Environmental Sciences, 2014. **26**(11): p. 2139-2177.

42. Chen, Y., et al., *Synthesis, characterization and electrochemical properties of mesoporous zirconia nanomaterials prepared by self-assembling sol–gel method with Tween 20 as a template.* Chemical Engineering Journal, 2011. **170**(2–3): p. 518-524.

43. Yun, J., et al., *The effect of La doping concentration on optical and electrical properties of LaxSr1-xTiO3 thin film fabricated by sol–gel process.* Thin Solid Films, 2016. **600**: p. 1-5.

44. Saáedi, A., et al., *XPS studies and photocurrent applications of alkali-metals-doped ZnO nanoparticles under visible illumination conditions.* Physica E: Low-dimensional Systems and Nanostructures, 2016. **79**: p. 113-118.

45. Djaoued, Y., S. Balaji, and N. Beaudoin, *Sol–gel synthesis of mesoporous* WO_3*–*TiO_2 *composite thin films for photochromic devices.* Journal of Sol-Gel Science and Technology, 2013. **65**(3): p. 374-383.

46. Gupta, S. and M. Tripathi, *A review on the synthesis of TiO2 nanoparticles by solution route*, in *Open Chemistry*. 2012. p. 279.

47. Chen, C., et al., *Template-free sol–gel preparation and characterization of free-standing visible light responsive C,N-modified porous monolithic* TiO_2. Journal of Hazardous Materials, 2010. **178**(1): p. 560-565.

48. Long, R.Q. and R.T. Yang, *Selective Catalytic Oxidation of Ammonia to Nitrogen over Fe_2O_3–TiO_2 Prepared with a Sol–Gel Method.* Journal of Catalysis, 2002. **207**(2): p. 158-165.

49. Lee, S., et al., *Two-Step Sol−Gel Method-Based TiO_2 Nanoparticles with Uniform Morphology and Size for Efficient Photo-Energy Conversion Devices.* Chemistry of Materials, 2010. **22**(6): p. 1958-1965.

50. Eiden-Assmann, S., J. Widoniak, and G. Maret, *Synthesis and Characterization of Porous and Nonporous Monodisperse Colloidal TiO_2 Particles.* Chemistry of Materials, 2004. **16**(1): p. 6-11.

51. Hirano, M., et al., *Photoactivity and phase stability of ZrO_2-doped anatase-type TiO_2 directly formed as nanometer-sized particles by hydrolysis under hydrothermal conditions.* Journal of Solid State Chemistry, 2003. **170**(1): p. 39-47.

52. Hanaor, D.A.H. and C.C. Sorrell, *Review of the anatase to rutile phase transformation.* Journal of Materials Science, 2011. **46**(4): p. 855-874.

53. Chen, Y.-F., et al., *The effect of calcination temperature on the crystallinity of TiO_2 nanopowders.* Journal of Crystal Growth, 2003. **247**(3): p. 363-370.

54. Hisatomi, T., J. Kubota, and K. Domen, *Recent advances in semiconductors for photocatalytic and photoelectrochemical water splitting.* Chemical Society Reviews, 2014. **43**(22): p. 7520-7535.

55. Fagan, R., et al., *A review of solar and visible light active TiO_2 photocatalysis for treating bacteria, cyanotoxins and contaminants of emerging concern.* Materials Science in Semiconductor Processing, 2016. **42, Part 1**: p. 2-14.

56. Varshney, G., et al., *Nanoscale TiO_2 films and their application in remediation of organic pollutants.* Coordination Chemistry Reviews, 2016. **306**: p. 43-64.

57. Siriwong, C., et al., *Doped-metal oxide nanoparticles for use as photocatalysts.* Progress in Crystal Growth and Characterization of Materials, 2012. **58**(2–3): p. 145-163.

58. Kerkez-Kuyumcu, Ö., et al., *A comparative study for removal of different dyes over M/TiO2 (M = Cu, Ni, Co, Fe, Mn and Cr) photocatalysts under visible light irradiation.* Journal of Photochemistry and Photobiology A: Chemistry, 2015. **311**: p. 176-185.

59. Asiltürk, M., F. Sayılkan, and E. Arpaç, *Effect of Fe^{3+} ion doping to TiO_2 on the photocatalytic degradation of Malachite Green dye under UV and vis-irradiation.* Journal of Photochemistry and Photobiology A: Chemistry, 2009. **203**(1): p. 64-71.

60. Kemp, T.J. and R.A. McIntyre, *Transition metal-doped titanium(IV) dioxide: Characterisation and influence on photodegradation of poly(vinyl chloride).* Polymer Degradation and Stability, 2006. **91**(1): p. 165-194.

61. Devi, L.G., et al., *Enhanced photocatalytic activity of transition metal ions* Mn^{2+}*,* Ni^{2+} *and* Zn^{2+} *doped polycrystalline titania for the degradation of Aniline Blue under UV/solar light.* Journal of Molecular Catalysis A: Chemical, 2010. **328**(1): p. 44-52.

62. Wilke, K. and H.D. Breuer, *The influence of transition metal doping on the physical and photocatalytic properties of titania.* Journal of Photochemistry and Photobiology A: Chemistry, 1999. **121**(1): p. 49-53.

63. Chang, S.-m. and W.-s. Liu, *The roles of surface-doped metal ions (V, Mn, Fe, Cu, Ce, and W) in the interfacial behavior of* TiO_2 *photocatalysts.* Applied Catalysis B: Environmental, 2014. **156**: p. 466-475.

64. Santos, R.d.S., et al., *Iron Insertion and Hematite Segregation on Fe-Doped* TiO_2 *Nanoparticles Obtained from Sol–Gel and Hydrothermal Methods.* ACS Applied Materials & Interfaces, 2012. **4**(10): p. 5555-5561.

65. Shough, A.M., D.J. Doren, and B. Ogunnaike, *Transition Metal Substitution in ETS-10: DFT Calculations and a Simple Model for Electronic Structure Prediction.* Chemistry of Materials, 2009. **21**(7): p. 1232-1241.

66. Zhou, M., J. Yu, and B. Cheng, *Effects of Fe-doping on the photocatalytic activity of mesoporous* TiO_2 *powders prepared by an ultrasonic method.* Journal of Hazardous Materials, 2006. **137**(3): p. 1838-1847.

67. Fujishima, A. and K. Honda, *Electrochemical Photolysis of Water at a Semiconductor Electrode.* Nature, 1972. **238**(5358): p. 37-38.

68. Schrauzer, G.N. and T.D. Guth, *Photocatalytic reactions. 1. Photolysis of water and photoreduction of nitrogen on titanium dioxide.* Journal of the American Chemical Society, 1977. **99**(22): p. 7189-7193.

69. Frank, S.N. and A.J. Bard, *Heterogeneous photocatalytic oxidation of cyanide ion in aqueous solutions at titanium dioxide powder.* Journal of the American Chemical Society, 1977. **99**(1): p. 303-304.

70. Gaya, U.I. and A.H. Abdullah, *Heterogeneous photocatalytic degradation of organic contaminants over titanium dioxide: A review of fundamentals, progress and problems.* Journal of Photochemistry and Photobiology C: Photochemistry Reviews, 2008. **9**(1): p. 1-12.

71. Robinson, T., et al., *Remediation of dyes in textile effluent: a critical review on current treatment technologies with a proposed alternative.* Bioresource Technology, 2001. **77**(3): p. 247-255.

72. Parshetti, G.K., et al., *Decolorization and detoxification of sulfonated azo dye methyl orange by Kocuria rosea MTCC 1532.* Journal of Hazardous Materials, 2010. **176**(1): p. 503-509.

73. Farag, A.A.M., et al., *Characterization of electrical and optical absorption of organic based methyl orange for photovoltaic application.* Synthetic Metals, 2011. **161**(19): p. 2135-2143.

74. Michałowicz, J. and W. Duda, *Phenols -- Sources and Toxicity.* Polish Journal of Environmental Studies, 2007. **16**(3): p. 347-362.

75. Park, M.-R., et al., *Influence of Immobilization of Bacterial Cells and* TiO_2 *on Phenol Degradation.* Water, Air, & Soil Pollution, 2013. **224**(3): p. 1473.

76. Zaidan, L.E.M.C., et al., *Heterogeneous photocatalytic degradation of phenol and derivatives by (*$BiPO_4/H_2O_2$*/UV and* TiO_2/H_2O_2*/UV) and the evaluation of plant seed toxicity tests.* Korean Journal of Chemical Engineering, 2017. **34**(2): p. 511-522.

77. Nguyen, D.C.T., K.-Y. Cho, and W.-C. Oh, *Synthesis of frost-like CuO combined graphene-*TiO_2 *by self-assembly method and its high photocatalytic performance.* Applied Surface Science, 2017. **412**: p. 252-261.

78. Cermenati, L., et al., *Probing the* TiO_2 *Photocatalytic Mechanisms in Water Purification by Use of Quinoline, Photo-Fenton Generated OH• Radicals and Superoxide Dismutase.* Journal of Physical Chemistry B, 1997. **101**(14): p. 2650-2658.

79. Suhadolnik, L., et al., *A* TiO_2*-nanotubes-based coil-type microreactor for highly efficient photoelectrocatalytic degradation of organic compounds.* Journal of Industrial and Engineering Chemistry, 2017. **47**: p. 384-390.

80. Jung, J.-J., J.-W. Jang, and J.-W. Park, *Effect of generation growth on photocatalytic activity of nano* TiO_2*-magnetic cored dendrimers.* Journal of Industrial and Engineering Chemistry, 2016. **44**: p. 52-59.

81. Wei, X.-N., et al., *Facile synthesis of tunable carbon modified mesoporous* TiO_2 *for visible light photocatalytic application.* Applied Surface Science, 2017. **412**: p. 357-365.

82. Asahi, R., et al., *Visible-Light Photocatalysis in Nitrogen-Doped Titanium Oxides.* Science, 2001. **293**(5528): p. 269-271.

83. Sun, M., et al., *Efficient Degradation of Azo Dyes over* Sb_2S_3/TiO_2 *Heterojunction under Visible Light Irradiation.* Industrial & Engineering Chemistry Research, 2012. **51**(7): p. 2897-2903.

84. Kang, I.-C., et al., *Improvement in Photocatalytic Activity of TiO_2 under Visible Irradiation through Addition of N-TiO_2.* Environmental Science & Technology, 2008. **42**(10): p. 3622-3626.

85. Peng, B., et al., *General Synthesis and Optical Properties of Monodisperse Multifunctional Metal-Ion-Doped TiO_2 Hollow Particles.* The Journal of Physical Chemistry C, 2009. **113**(47): p. 20240-20245.

86. Ma, T.-Y., et al., *Hierarchically Structured Squama-like Cerium-Doped Titania: Synthesis, Photoactivity, and Catalytic CO Oxidation.* The Journal of Physical Chemistry C, 2009. **113**(38): p. 16658-16667.

87. Yu, H., et al., *An Efficient Visible-Light-Sensitive Fe(III)-Grafted TiO_2 Photocatalyst.* The Journal of Physical Chemistry C, 2010. **114**(39): p. 16481-16487.

88. Liu, B. and X. Zhao, *The synergetic effect of V and Fe-co-doping in TiO_2 studied from the DFT + U first-principle calculation.* Applied Surface Science, 2017. **399**: p. 654-662.

89. Roy, N., et al., *Engineered Electronic States of Transition Metal Doped TiO_2 Nanocrystals for Low Overpotential Oxygen Evolution Reaction.* The Journal of Physical Chemistry C, 2014. **118**(51): p. 29499-29506.

90. Harb, M., *Screened Coulomb Hybrid DFT Study on Electronic Structure and Optical Properties of Anionic and Cationic Te-Doped Anatase TiO_2.* The Journal of Physical Chemistry C, 2013. **117**(25): p. 12942-12948.

91. Piskunov, S., et al., *C-, N-, S-, and Fe-Doped TiO_2 and $SrTiO_3$ Nanotubes for Visible-Light-Driven Photocatalytic Water Splitting: Prediction from First Principles.* The Journal of Physical Chemistry C, 2015. **119**(32): p. 18686-18696.

92. Choi, W., A. Termin, and M.R. Hoffmann, *The Role of Metal Ion Dopants in Quantum-Sized TiO_2: Correlation between Photoreactivity and Charge Carrier Recombination Dynamics.* The Journal of Physical Chemistry, 1994. **98**(51): p. 13669-13679.

93. Kumar, A. and A.K. Jain, *Photophysics and photocatalytic properties of Ag^+-activated sandwich Q-CdS–TiO_2.* Journal of Photochemistry and Photobiology A: Chemistry, 2003. **156**(1–3): p. 207-218.

94. Di Paola, A., et al., *Preparation of Polycrystalline TiO_2 Photocatalysts Impregnated with Various Transition Metal Ions: Characterization and Photocatalytic Activity for the Degradation of 4-Nitrophenol.* The Journal of Physical Chemistry B, 2002. **106**(3): p. 637-645.

95. Moser, J., M. Grätzel, and R. Gallay, *Inhibition of Electron-Hole Recombination in Substitutionally Doped Colloidal Semiconductor Crystallites.* Helvetica Chimica Acta, 1987. **70**(6): p. 1596-1604.

96. Oh, W.-C., et al., *Characterization and relative photonic efficiencies of a new Fe-ACF/*TiO_2 *composite photocatalysts designed for organic dye decomposition.* Journal of Industrial and Engineering Chemistry, 2009. **15**(2): p. 190-195.

97. Shi, Z., et al., *Photocatalytic Activity of Fe and Ce Co-doped Mesoporous* TiO_2 *Catalyst under UV and Visible Light.* Journal of the Chinese Chemical Society, 2012. **59**(5): p. 614-620.

98. Khalid, N.R., et al., *Synergistic effects of Fe and graphene on photocatalytic activity enhancement of* TiO_2 *under visible light.* Applied Surface Science, 2012. **258**(15): p. 5827-5834.

99. Cui, L., et al., *A visible light active photocatalyst: Nano-composite with Fe-doped anatase* TiO_2 *nanoparticles coupling with* TiO_2*(B) nanobelts.* Journal of Molecular Catalysis A: Chemical, 2010. **326**(1–2): p. 1-7.

100. Cui, L., et al., *Synthesis and visible light photocatalysis of Fe-doped* TiO_2 *mesoporous layers deposited on hollow glass microbeads.* Journal of Solid State Chemistry, 2009. **182**(10): p. 2785-2790.

101. Zhang, K., et al., *Preparation of highly visible light active Fe-N co-doped mesoporous* TiO_2 *photocatalyst by fast sol-gel method.* Journal of Nanoparticle Research, 2014. **16**(2): p. 1-9.

102. Xiao, L., et al., *Synergistic effects of doped* Fe^{3+} *and deposited Au on improving the photocatalytic activity of* TiO_2*.* Catalysis Letters, 2006. **111**(3): p. 207-211.

103. Qamar, M., et al., *Synthesis and photocatalytic activity of mesoporous nanocrystalline Fe-doped titanium dioxide.* Catalysis Today, 2014. **230**: p. 158-165.

104. Xing, M., et al., *Effect of synergy on the visible light activity of B, N and Fe co-doped* TiO_2 *for the degradation of MO.* Nanoscale, 2010. **2**(7): p. 1233-1239.

105. Tong, T., et al., *Preparation of* Fe^{3+}*-doped* TiO_2 *catalysts by controlled hydrolysis of titanium alkoxide and study on their photocatalytic activity for methyl orange degradation.* Journal of Hazardous Materials, 2008. **155**(3): p. 572-579.

106. Bajnóczi, É.G., et al., *The influence of the local structure of Fe(III) on the photocatalytic activity of doped* TiO_2 *photocatalysts—An EXAFS, XPS and Mössbauer spectroscopic study*. Applied Catalysis B: Environmental, 2011. **103**(1–2): p. 232-239.

107. Hung, W.-C., et al., *Synthesis and characterization of TiO_2 and Fe/TiO_2 nanoparticles and their performance for photocatalytic degradation of 1,2-dichloroethane.* Applied Surface Science, 2008. **255**(5, Part 1): p. 2205-2213.

108. Nahar, M.S., K. Hasegawa, and S. Kagaya, *Photocatalytic degradation of phenol by visible light-responsive iron-doped TiO_2 and spontaneous sedimentation of the TiO_2 particles.* Chemosphere, 2006. **65**(11): p. 1976-1982.

109. Nagaveni, K., M.S. Hegde, and G. Madras, *Structure and Photocatalytic Activity of $Ti_{1-x}M_xO_{2\pm\delta}$ (M = W, V, Ce, Zr, Fe, and Cu) Synthesized by Solution Combustion Method.* The Journal of Physical Chemistry B, 2004. **108**(52): p. 20204-20212.

110. Sidhu, P.S., et al., *Dissolution of iron oxides and oxyhydroxides in hydrochloric and perchloric acids.* Clays and Clay Minerals, 1981. **29**(6): p. 269-276.

111. Yu, J., Q. Xiang, and M. Zhou, *Preparation, characterization and visible-light-driven photocatalytic activity of Fe-doped titania nanorods and first-principles study for electronic structures.* Applied Catalysis B: Environmental, 2009. **90**(3–4): p. 595-602.

112. Parayil, S.K., et al., *Synthesis of mixed phase anatase-TiO_2(B) by a simple wet chemical method.* Materials Letters, 2013. **95**: p. 175-177.

113. Yang, H.G., et al., *Anatase TiO_2 single crystals with a large percentage of reactive facets.* Nature, 2008. **453**(7195): p. 638-641.

114. Rao, Y., et al., *Organic Solvent-Dispersed TiO_2 Nanoparticle Characterization.* Langmuir, 2009. **25**(21): p. 12713-12720.

115. Inturi, S.N.R., et al., *Visible-light-induced photodegradation of gas phase acetonitrile using aerosol-made transition metal (V, Cr, Fe, Co, Mn, Mo, Ni, Cu, Y, Ce, and Zr) doped TiO_2.* Applied Catalysis B: Environmental, 2014. **144**: p. 333-342.

116. Yu, J., et al., *Effects of pH on the microstructures and photocatalytic activity of mesoporous nanocrystalline titania powders prepared via hydrothermal method.* Journal of Molecular Catalysis A: Chemical, 2006. **258**(1–2): p. 104-112.

117. Isley, S.L. and R.L. Penn, *Titanium Dioxide Nanoparticles: Effect of Sol−Gel pH on Phase Composition, Particle Size, and Particle Growth Mechanism.* The Journal of Physical Chemistry C, 2008. **112**(12): p. 4469-4474.

118. Andersson, S.L.T. and R.F. Howe, *An x-ray photoelectron study of metal clusters in zeolites.* The Journal of Physical Chemistry, 1989. **93**(12): p. 4913-4920.

119. Grosvenor, A.P., et al., *Investigation of multiplet splitting of Fe 2p XPS spectra and bonding in iron compounds.* Surface and Interface Analysis, 2004. **36**(12): p. 1564-1574.

120. Wang, G., et al., *Facile Synthesis of Highly Photoactive α-Fe_2O_3-Based Films for Water Oxidation.* Nano Letters, 2011. **11**(8): p. 3503-3509.

121. Moulder, J.F.S., W. F.; Sobol, P. E.; Bomben, K. D. Handbook of X-ray Photoelectron Spectroscopy. In Physical Electronics Division, Perkin-Elmer Corporation: Eden rairie, MN, 1992.

122. Fujii, T., et al., *In situ XPS analysis of various iron oxide films grown by NO_2-assisted molecular-beam epitaxy.* Physical Review B, 1999. **59**(4): p. 3195-3202.

123. Mills, P. and J.L. Sullivan, *A study of the core level electrons in iron and its three oxides by means of X-ray photoelectron spectroscopy.* Journal of Physics D: Applied Physics, 1983. **16**(5): p. 723.

124. Saha, N.C. and H.G. Tompkins, *Titanium nitride oxidation chemistry: An x-ray photoelectron spectroscopy study.* Journal of Applied Physics, 1992. **72**(7): p. 3072-3079.

125. Song, Z., J. Hrbek, and R. Osgood, *Formation of TiO_2 Nanoparticles by Reactive-Layer-Assisted Deposition and Characterization by XPS and STM.* Nano Letters, 2005. **5**(7): p. 1327-1332.

126. Chiarello, G.L., M.H. Aguirre, and E. Selli, *Hydrogen production by photocatalytic steam reforming of methanol on noble metal-modified TiO_2.* Journal of Catalysis, 2010. **273**(2): p. 182-190.

127. Khan, H. and I.K. Swati, *Fe^{3+}-doped Anatase TiO_2 with d–d Transition, Oxygen Vacancies and Ti^{3+} Centers: Synthesis, Characterization, UV–vis Photocatalytic and Mechanistic Studies.* Industrial & Engineering Chemistry Research, 2016. **55**(23): p. 6619-6633.

128. Liu, X., et al., *Ti^{3+} self-doped TiO_2-x anatase nanoparticles via oxidation of TiH_2 in H_2O_2.* Catalysis Today, 2014. **225**: p. 80-89.

129. Zhang, X., et al., *The role of oxygen vacancy-Ti^{3+} states on TiO_2 nanotubes' surface in dye-sensitized solar cells.* Materials Letters, 2013. **100**: p. 51-53.

130. Yang, T.-S., et al., *Effect of N_2 ion flux on the photocatalysis of nitrogen-doped titanium oxide films by electron-beam evaporation.* Applied Surface Science, 2006. **252**(10): p. 3729-3736.

131. Liu, M., et al., *Energy-Level Matching of Fe(III) Ions Grafted at Surface and Doped in Bulk for Efficient Visible-Light Photocatalysts.* Journal of the American Chemical Society, 2013. **135**(27): p. 10064-10072.

132. *Electronic depiction of magnetic origin in undoped and Fe doped TiO_2-d epitaxial thin films.* Applied Physics Letters, 2011. **99**(11): p. 112502.

133. Shao, Y., et al., *Investigation of nitrogen doped and carbon species decorated* TiO_2 *with enhanced visible light photocatalytic activity by using chitosan.* Applied Catalysis B: Environmental, 2015. **179**: p. 344-351.

134. George, S., et al., *Role of Fe Doping in Tuning the Band Gap of* TiO_2 *for the Photo-Oxidation-Induced Cytotoxicity Paradigm.* Journal of the American Chemical Society, 2011. **133**(29): p. 11270-11278.

135. Zhu, J., et al., Fe^{3+}-TiO_2 *photocatalysts prepared by combining sol–gel method with hydrothermal treatment and their characterization.* Journal of Photochemistry and Photobiology A: Chemistry, 2006. **180**(1–2): p. 196-204.

136. Abbas, N., et al., *Sol–gel synthesis of* TiO_2-Fe_2O_3 *systems: Effects of Fe2O3 content and their photocatalytic properties.* Journal of Industrial and Engineering Chemistry, 2016. **39**: p. 112-120.

137. Zhang, Y., et al., *Influence of Fe ions in characteristics and optical properties of mesoporous titanium oxide thin films.* Applied Surface Science, 2009. **256**(1): p. 85-89.

138. Wang, Q., et al., *Photocatalytic Fe-doped TiO2/PSF composite UF membranes: Characterization and performance on BPA removal under visible-light irradiation.* Chemical Engineering Journal, 2017. **319**: p. 39-47.

139. Wang, X.H., et al., *Pyrogenic Iron(III)-Doped* TiO_2 *Nanopowders Synthesized in RF Thermal Plasma: Phase Formation, Defect Structure, Band Gap, and Magnetic Properties.* Journal of the American Chemical Society, 2005. **127**(31): p. 10982-10990.

140. Yan, X., et al., *Novel three-dimensionally ordered macroporous* Fe^{3+}*-doped* TiO_2 *photocatalysts for* H_2 *production and degradation applications.* Applied Surface Science, 2017. **394**: p. 248-257.

141. Tieng, S., et al., *Nucleation−Growth of* TiO_2 *Nanoparticles Doped with Iron Acetylacetonate.* The Journal of Physical Chemistry C, 2011. **115**(13): p. 5244-5250.

142. Pang, Y.L. and A.Z. Abdullah, Fe^{3+} *doped* TiO_2 *nanotubes for combined adsorption–sonocatalytic degradation of real textile wastewater.* Applied Catalysis B: Environmental, 2013. **129**: p. 473-481.

143. Cai, L., X. Liao, and B. Shi, *Using Collagen Fiber as a Template to Synthesize* TiO_2 *and* Fe_x/TiO_2 *Nanofibers and Their Catalytic Behaviors on the Visible Light-Assisted Degradation of Orange II.* Industrial & Engineering Chemistry Research, 2010. **49**(7): p. 3194-3199.

144. Xu, C., et al., *Enhanced mechanism of the photo-thermochemical cycle based on effective Fe-doping TiO_2 films and DFT calculations.* Applied Catalysis B: Environmental, 2017. **204**: p. 324-334.

145. Shon, H.K., et al., *Development of a novel method to prepare Fe- and Al-doped TiO_2 from wastewater.* Journal of Industrial and Engineering Chemistry, 2009. **15**(4): p. 476-482.

146. Wang, S. and S. Zhou, *Titania deposited on soft magnetic activated carbon as a magnetically separable photocatalyst with enhanced activity.* Applied Surface Science, 2010. **256**(21): p. 6191-6198.

147. Wu, F., et al., *Enhanced photocatalytic degradation and adsorption of methylene blue via TiO_2 nanocrystals supported on graphene-like bamboo charcoal.* Applied Surface Science, 2015. **358**: p. 425-435.

148. Wu, F., et al., *Highly enhanced photocatalytic degradation of methylene blue over the indirect all-solid-state Z-scheme g-C_3N_4-RGO-TiO_2 nanoheterojunctions.* Applied Surface Science, 2017. **405**: p. 60-70.

149. Andersson, M., et al., *Preparation of Nanosize Anatase and Rutile TiO_2 by Hydrothermal Treatment of Microemulsions and Their Activity for Photocatalytic Wet Oxidation of Phenol.* The Journal of Physical Chemistry B, 2002. **106**(41): p. 10674-10679.

150. Morville, S., et al., *Spatial and Geographical Variations of Urban, Suburban and Rural Atmospheric Concentrations of Phenols and Nitrophenols (7 pp).* Environmental Science and Pollution Research, 2006. **13**(2): p. 83-89.

151. Busca, G., et al., *Technologies for the removal of phenol from fluid streams: A short review of recent developments.* Journal of Hazardous Materials, 2008. **160**(2–3): p. 265-288.

152. W. Jordan, H.v.B., O. Gerlich, M. Kleine-Boymann, J. Ullrich, *Ullmann's Encyclopedia of Industrial Chemistry*. 2002: Wiley-VCH Verlag.

153. Sriwong, C., S. Wongnawa, and O. Patarapaiboolchai, *Recyclable thin TiO_2-embedded rubber sheet and dye degradation.* Chemical Engineering Journal, 2012. **191**: p. 210-217.

154. Vinu, R., S.U. Akki, and G. Madras, *Investigation of dye functional group on the photocatalytic degradation of dyes by nano-TiO_2.* Journal of Hazardous Materials, 2010. **176**(1): p. 765-773.

155. Aarthi, T., P. Narahari, and G. Madras, *Photocatalytic degradation of Azure and Sudan dyes using nano TiO_2.* Journal of Hazardous Materials, 2007. **149**(3): p. 725-734.

156. Wongkalasin, P., S. Chavadej, and T. Sreethawong, *Photocatalytic degradation of mixed azo dyes in aqueous wastewater using mesoporous-assembled TiO_2 nanocrystal synthesized by a modified sol–gel process.* Colloids and Surfaces A: Physicochemical and Engineering Aspects, 2011. **384**(1): p. 519-528.

157. Lugo-Vega, C.S., B. Serrano-Rosales, and H. de Lasa, *Immobilized particle coating for optimum photon and TiO_2 utilization in scaled air treatment photo reactors.* Applied Catalysis B: Environmental, 2016. **198**: p. 211-223.

158. Wang, W., et al., *Enhanced photocatalytic activity of hierarchical macro/mesoporous TiO_2–graphene composites for photodegradation of acetone in air.* Applied Catalysis B: Environmental, 2012. **119**: p. 109-116.

159. Selishchev, D.S., et al., *TiO_2 mediated photocatalytic oxidation of volatile organic compounds: Formation of CO as a harmful by-product.* Applied Catalysis B: Environmental, 2017. **200**: p. 503-513.

160. Reddy, P.A.K., et al., *Recent advances in photocatalytic treatment of pollutants in aqueous media.* Environment International, 2016. **91**: p. 94-103.

161. Yadav, H.M., J.-S. Kim, and S.H. Pawar, *Developments in photocatalytic antibacterial activity of nano TiO_2: A review.* Korean Journal of Chemical Engineering, 2016. **33**(7): p. 1989-1998.

162. Konstantinou, I.K. and T.A. Albanis, *TiO_2-assisted photocatalytic degradation of azo dyes in aqueous solution: kinetic and mechanistic investigations.* Applied Catalysis B: Environmental, 2004. **49**(1): p. 1-14.

163. Carp, O., C.L. Huisman, and A. Reller, *Photoinduced reactivity of titanium dioxide.* Progress in Solid State Chemistry, 2004. **32**(1–2): p. 33-177.

164. Chen, J., et al., *Recent progress in enhancing photocatalytic efficiency of TiO_2-based materials.* Applied Catalysis A: General, 2015. **495**: p. 131-140.

165. Mor, G.K., et al., *A review on highly ordered, vertically oriented TiO_2 nanotube arrays: Fabrication, material properties, and solar energy applications.* Solar Energy Materials and Solar Cells, 2006. **90**(14): p. 2011-2075.

166. Chen, C., W. Ma, and J. Zhao, *Semiconductor-mediated photodegradation of pollutants under visible-light irradiation.* Chemical Society Reviews, 2010. **39**(11): p. 4206-4219.

167. Chen, X., et al., *Semiconductor-based Photocatalytic Hydrogen Generation.* Chemical Reviews, 2010. **110**(11): p. 6503-6570.

168. Kumbhar, A. and G. Chumanov, *Synthesis of Iron(III)-Doped Titania Nanoparticles and its Application for Photodegradation of Sulforhodamine-B Pollutant.* Journal of Nanoparticle Research, 2005. **7**(4): p. 489-498.

169. Sun, S., et al., *Photocatalytic degradation of gaseous toluene on Fe-TiO_2 under visible light irradiation: A study on the structure, activity and deactivation mechanism.* Applied Surface Science, 2012. **258**(12): p. 5031-5037.

170. Lu, Z.-Y. and D.M. Muir, *Dissolution of metal ferrites and iron oxides by HCl under oxidising and reducing conditions.* Hydrometallurgy, 1988. **21**(1): p. 9-21.

171. Zhang, Q., L. Gao, and J. Guo, *Effects of calcination on the photocatalytic properties of nanosized TiO_2 powders prepared by $TiCl_4$ hydrolysis.* Applied Catalysis B: Environmental, 2000. **26**(3): p. 207-215.

172. Khanna, P.K., N. Singh, and S. Charan, *Synthesis of nano-particles of anatase-TiO_2 and preparation of its optically transparent film in PVA.* Materials Letters, 2007. **61**(25): p. 4725-4730.

173. Sun, S., et al., *Full visible-light absorption of TiO_2 nanotubes induced by anionic S_2^{2-} doping and their greatly enhanced photocatalytic hydrogen production abilities.* Applied Catalysis B: Environmental, 2017. **206**: p. 168-174.

174. Liu, Z., L. Hong, and B. Guo, *Physicochemical and electrochemical characterization of anatase titanium dioxide nanoparticles.* Journal of Power Sources, 2005. **143**(1–2): p. 231-235.

175. Pang, Y.L. and A.Z. Abdullah, *Effect of low Fe^{3+} doping on characteristics, sonocatalytic activity and reusability of TiO_2 nanotubes catalysts for removal of Rhodamine B from water.* Journal of Hazardous Materials, 2012. **235–236**: p. 326-335.

176. Kalantari, K., et al., *Enhancing the photocatalytic oxidation of dibenzothiophene using visible light responsive Fe and N co-doped TiO_2 nanoparticles.* Ceramics International, 2017. **43**(1, Part B): p. 973-981.

177. Farhangi, N., et al., *Visible light active Fe doped TiO_2 nanowires grown on graphene using supercritical CO_2.* Applied Catalysis B: Environmental, 2011. **110**: p. 25-32.

178. Liu, S. and Y. Chen, *Enhanced photocatalytic activity of TiO_2 powders doped by Fe unevenly.* Catalysis Communications, 2009. **10**(6): p. 894-899.

179. Melghit, K., O.S. Al-Shukeili, and I. Al-Amri, *Effect of M-doping (M = Fe, V) on the photocatalytic activity of nanorod rutile TiO_2 for Congo red degradation under the sunlight.* Ceramics International, 2009. **35**(1): p. 433-439.

180. Yalçın, Y., M. Kılıç, and Z. Çınar, *Fe^{3+}-doped TiO_2: A combined experimental and computational approach to the evaluation of visible light activity.* Applied Catalysis B: Environmental, 2010. **99**(3–4): p. 469-477.

181. Li, B., et al., *Preparation and characterization of nano-TiO_2 powder.* Materials Chemistry and Physics, 2003. **78**(1): p. 184-188.

182. Sugimoto, T., X. Zhou, and A. Muramatsu, *Synthesis of uniform anatase TiO_2 nanoparticles by gel–sol method: 3. Formation process and size control.* Journal of Colloid and Interface Science, 2003. **259**(1): p. 43-52.

183. Kambur, A., G.S. Pozan, and I. Boz, *Preparation, characterization and photocatalytic activity of TiO_2–ZrO_2 binary oxide nanoparticles.* Applied Catalysis B: Environmental, 2012. **115–116**: p. 149-158.

184. Doong, R.-A., et al., *The influence of pH and cadmium sulfide on the photocatalytic degradation of 2-chlorophenol in titanium dioxide suspensions.* Water Research, 2001. **35**(12): p. 2873-2880.

185. Chiou, C.-H., C.-Y. Wu, and R.-S. Juang, *Influence of operating parameters on photocatalytic degradation of phenol in UV/TiO_2 process.* Chemical Engineering Journal, 2008. **139**(2): p. 322-329.